5-1-2011

The role of diffusion and membrane topography in the initiation of high affinity IgE receptor signaling

Nicholas Andrews

Nicholas L. Andrews

Candidate

Biomedical Sciences

Department

This dissertation is approved, and it is acceptable in quality and form for publication on microfilm:

Approved by the Dissertation Committee:

, Chairperson

Accepted:

Dean, Graduate School

Date

THE ROLE OF DIFFUSION AND MEMBRANE TOPOGRAPHY IN THE INITIATION OF HIGH AFFINITY IGE RECEPTOR SIGNALING

by

NICHOLAS L. ANDREWS

B.S. Biology/Spanish, University of New Mexico 2001

DISSERTATION

Submitted in Partial Fulfillment of the
Requirements for the Degree of

Doctor of Philosophy
Biomedical Sciences

The University of New Mexico
Albuquerque, New Mexico

May 2011

DEDICATION

This is dedicated to my family, my best teachers. Thanks Addie, Owen, and Liam for all your patience, support, and love throughout this long process. You all have kept me grounded and made it so easy for me to focus on the things that really matter. To Owen, I'm sure that I've learned more from you than you have from me in these last five years. Watching you laugh, play, learn, challenge, and grow has helped inspire me to do those things more myself. I'm so proud to be your dad. Liam, from you I've learned that there's never any reason not to laugh, smile, or have seconds. Keep smiling and I'll do the same. Addie, you have always been there patiently waiting, passionately encouraging, loudly cheering, thanklessly working, and tirelessly loving. I couldn't ask for anything more, thank you for being you. By being you, you teach me how to be me. I sure couldn't have gotten this far on my own. I love you all.

ACKNOWLEDGEMENT

I would first like to acknowledge my mentor, Dr. Diane Lidke. Diane has been invaluable in helping me through my dissertation research and I feel honored to have been her first graduate student. I have sincerely appreciated her enthusiasm for this project and her willingness to help me with any and all aspects of my research from experiment design to writing image analysis code to writing the manuscript and preparing posters; her door has always been open.

I would also like to acknowledge my other committee members for the unique attributes they have brought to bear in advising me. Dr. Jan Oliver has always helped me to see the larger context of my project and has been my go-to person when I need to find just the right way to phrase an idea. Dr. Bridget Wilson has a knack for focusing on the small details and so I have learned to have my work as polished as possible before bringing it to her for review. Dr. Bill Shuttleworth put the pressure on me very early in my project to make my research hypothesis-driven, something that has proven a challenge when utilizing so many state-of-the-art techniques, but also something that has strengthened my research tremendously. Dr. Tim Boyle helped to put me on this path nearly nine years ago by introducing me to "real" science. Each year I realize more how much I learned working with Tim: how to think like a scientist, how to prepare a manuscript, and how to present my findings. Thanks, Tim, for putting me and so many other young scientists ahead of the curve going into our first graduate lab rotation.

None of this work would have been possible without the help of my co-workers and colleagues. The wonderful technicians in the OWL lab who helped me so often and

so willingly over the past three and a half years: Marina Martinez, Jan Pfeiffer, Mary Raymond-Stintz, and Christy Tarleton. Thanks to my fellow grad students Shujie Yang and Shalini Low-Nam for all of their personal and professional support. Also, a special thanks to Dr. Keith Lidke for serving as my own personal Matlab support person and technician. The vast majority of the analyses in this work would not have been possible without Keith's expertise. Thanks as well to Dr. Dave Haaland, Dr. Mike Sinclair, and Dr. Ryan Davis; my colleagues at Sandia National Laboratories who generously gave of their time and equipment to make the hyperspectral imaging studies possible.

THE ROLE OF DIFFUSION AND MEMBRANE TOPOGRAPHY IN THE INITIATION OF HIGH AFFINITY IGE RECEPTOR SIGNALING

by

NICHOLAS L. ANDREWS

ABSTRACT OF DISSERTATION

Submitted in Partial Fulfillment of the
Requirements for the Degree of

Doctor of Philosophy
Biomedical Sciences

The University of New Mexico
Albuquerque, New Mexico

May 2011

THE ROLE OF DIFFUSION AND MEMBRANE TOPOGRAPHY IN THE INITIATION OF HIGH AFFINITY IGE RECEPTOR SIGNALING

by

Nicholas L. Andrews

B.S., Biology/Spanish, University of New Mexico, 2001

Ph.D., Biomedical Sciences, 2011

ABSTRACT

The high affinity IgE receptor (FcεRI) plays a primary role in the pathogenesis of allergic disease and shares significant similarities with the two other multichain immune recognition receptor family members, the B-cell receptor and T-cell receptor. A wealth of information exists in all three of these receptor systems with regard to the signaling cascades occurring subsequent to receptor activation. It is also known that all three require binding of multivalent antigen to initiate signaling. However, very little is known about the precise mechanism by which multivalent antigen binding initializes downstream signaling. It has long been known that, in response to antigen binding, FcεRI reorganizes into large aggregates on the cell surface and that the receptor transitions from freely diffusing to highly immobile. The extent of aggregation and immobilization appears to correlate strongly with the extent of cellular activation, as measured by release of pre-formed mediators of allergic inflammation from intracellular granules. These observations have fueled speculation that immobilization of FcεRI may be the primary driver behind signal initiation. However, technical limitations related to the challenges of imaging highly dynamic, nanometer scale phenomena in living cells has precluded detailed examination of these processes.

Here, we describe the development of novel live cell imaging techniques and quantum dot (QD) based probes to address the role played by receptor dynamics in FcεRI signaling. Using multi-color single QD tracking, we rigorously quantified the diffusion of FcεRI in the absence of multivalent antigen and discovered a novel role for the actin cytoskeleton in modulating the diffusion of transmembrane proteins on micron length scales. We developed a real-time assay to monitor the kinetics of antigen-induced immobilization of FcεRI and report that this process is influenced by the actin cytoskeleton and heavily dependent on multivalent antigen concentration. We describe the relationship between immobilization, clustering and signal intiation and demonstrate that immobilization is not required for robust signaling. We also show that antigen-induced aggregation and internalization of FcεRI is not dependent on downstream signaling. From these data, we propose that the size of receptor clusters alone dictates the mobility, signaling competence, and internalization of FcεRI.

Table of Contents

ACKNOWLEDGEMENT iv

ABSTRACT vii

CHAPTER 1: INTRODUCTION 1

1.1 The multichain immune recognition receptor family 2

1.2 Overview of an allergic inflammatory response 3

1.3 High Affinity IgE Receptor Overview 4

1.4 FcεRI Signaling 7

1.4.1 The FcεRI signaling cascade 7

1.4.2 Role of topography in FcεRI signaling 9

1.4.3 Role of dynamics in FcεRI signaling 12

1.5 Single Particle Tracking 13

1.5.1 Single Particle Tracking Overview 14

1.5.2 Single Particle Tracking of FcεRI 17

1.5.3 Quantum Dots for SPT 18

1.6 Hypothesis: Changes in FcεRI diffusion and topography serve to initiate FcεRI signaling. 19

CHAPTER 2: ACTIN RESTRICTS FCεRI DIFFUSION AND FACILITATES ANTIGEN-INDUCED RECEPTOR IMMOBILIZATION 21

2.1 ABSTRACT 23

2.2 INTRODUCTION 24

2.3 RESULTS 26

2.3.1 QD-IgE is functionally monovalent 26

2.3.2 QD-IgE-FcεRI demonstrates characteristic membrane protein diffusion 29

2.3.3 Receptors are co-confined in micron-scale membrane domains 30

2.3.4 Dynamic actin structures restrict FcεRI diffusion 34

2.3.5 Cytoskeletal disruption slows immobilization kinetics 40
2.4 DISCUSSION 41
2.5 MATERIALS AND METHODS 45
2.5.1 Reagents 45
2.5.2 Cell culture 45
2.5.3 Degranulation assay 45
2.5.4 Cell treatment for SPT experiments 46
2.5.5 Cell treatment for immobilization 46
2.5.6 Electron Microscopy 46
2.5.7 Fluorescence Microscopy 47
2.5.8 Single Particle Tracking 48
2.5.9 Statistical Analysis 49
2.5.10 Image Processing 49
2.6 ACKNOWLEDGEMENTS 49
CHAPTER 3: ANTIGEN-INDUCED FcεRI IMMOBILIZATION IS REQUIRED FOR INTERNALIZATION, NOT SIGNALING 51
3.1 ABSTRACT 53
3.2 INTRODUCTION 54
3.3 RESULTS 56
3.3.1 Dose dependence of immobilization and cluster size 56
3.3.2 Role of downstream signaling 60
3.3.3 Direct cross-linking of IgE-FcεRI is required for immobilization 63
3.3.4 Antigen-induced clusters of at least three receptors do not immobilize 66
3.3.5 Multivalent antigen remains highly mobile at low, activating doses 69
3.6 DISCUSSION 72
3.7 MATERIALS AND METHODS 79
3.7.1 Reagents 79

3.7.1.1 Synthesis of DNP-QD 79
3.7.1.2 Synthesis of dansyl-BSA 80
3.7.2 Cell culture 80
3.7.3 Degranulation assay 80
3.7.4 IP and Western Blotting 80
3.7.5 Wide-field imaging 81
3.7.5.1 SPT of QD-IgE 81
3.7.5.2 SPT of DNP-QD 82
3.7.5.3 Kinetics of immobilization assay 82
3.7.6 Confocal imaging of $IgE_{anti\text{-}DNP}$ and $IgE_{anti\text{-}dansyl}$ 83
3.7.7 Hyperspectral imaging microscopy 84
3.7.8 Electron microscopy 84
3.7.9 Flow cytometry 85
3.7.10 Statistical analysis 85
3.7.11 Image Processing 85
3.8 ACKNOWLEDGEMENTS 86
CHAPTER 4: SUMMARY, IMPLICATIONS, AND FUTURE STUDIES 87
4.1 SUMMARY 88
4.1.1 Chapter 2 summary 88
4.1.2 Chapter 3 summary 90
4.2 IMPLICATIONS 93
4.2.1 Implications for FcεRI diffusion and plasma membrane structure 93
4.2.2 Implications for multichain immune recognition receptor activation 95
4.3 FUTURE STUDIES 96
4.3.1 Future Study 1: Probing the dynamics of non-IgE-bound FcεRI 97
4.3.2 Future Study 2: Dose dependent temporal regulation of FcεRI signaling 98

4.3.3 Future Study 3: Mechanism of FcεRI internalization 99
4.4 CONCLUDING REMARKS 100
APPENDIX A: SUPPLEMENTARY INFORMATION FOR CHAPTER 2 102
A.1 Supplementary Figures for Chapter 2 103
A.2 Supplementary Video Legends 110
A.3 Supplementary Methods 112
A.3.1 EM analysis of QD-IgE valency 112
A.3.2 TIRF controls 112
A.3.3 Gene constructs and transfection 114
A.3.4 Image Registration 115
A.3.5 Image Processing 115
A.3.6 Single Particle Tracking 116
A.3.7 Short range interaction analyses 118
A.3.8 Deconvolution 119
A.3.9 Binary Segmentation of Actin Structures 120
A.3.10 Actin Trajectory Overlap 120
A.3.11 Diffusion in proximity to actin 121
APPENDIX B: SUPPLEMENTARY INFORMATION FOR CHAPTER 3 123
B.1 Supplementary Figures for Chapter 3 124
B.2 Supplementary Video Legend 129
B.3 Supplementary Methods for Chapter 2 129
B.3.1 Simultaneous Ca^{2+} Ratio Imaging and SPT 129
REFERENCES 131

List of Figures

Figure 1.1. Structure of the alpha chain of FcεRI and its interaction with IgE. 6

Figure 1.2. Schematic representation of FcεRI signaling 8

Figure 1.3. FcεRI is distributed nonrandomly on resting and activated mast cells 11

Figure 1.4. Shematic representation of topographical progression of FcεRI signaling 12

Figure 1.5. Mean square displacement plots..... 17

Figure 2.1. QD-IgE serves as a non-perturbing probe of FcεRI diffusion..... 28

Figure 2.2. FcεRI are co-confined 32

Figure 2.3. Motion of QD-IgE-FcεRI is consistent with co-confinement; not attraction . 34

Figure 2.4. Actin defines regions of FcεRI motion in the membrane..... 36

Figure 2.5. Effect of actin proximity on FcεRI trajectories 38

Figure 2.6. Actin facilitates cross-link-induced immobilization of FcεRI 39

Figure 3.1. Antigen induced immobilization and degranulation are dose-dependent 58

Figure 3.2. Clustering of IgE-FcεRI is dose-dependent 60

Figure 3.3. PP2-sensitve signaling is not required for immobilization or internalization 62

Figure 3.4. Direct cross-linking is required for immobilization 65

Figure 3.5. Antigen-induced clusters of at least three QD-IgE-FcεRI remain mobile 68

Figure 3.6. DNP-QD remains mobile at activating doses..... 70

Figure 3.7. Cluster-centric model of MIRR signaling 78

Figure S2.1. QD-IgE is predominantly monovalent 103

Figure S2.2. Influence of temperature on diffusion..... 103

Figure S2.3. QD-IgE-FcεRI exhibits four motional modes 103

Figure S2.4. Analysis of simulated receptor dimerization or co-confinement 104

Figure S2.5. Membrane-coverslip distance does not dictate QD-IgE-FcεRI diffusion .. 105

Figure S2.6. GFP-actin structure is visibly disrupted by latrunculin treatment..... 107

Figure S2.7. Electron microscopy of membrane sheets..... 108

Figure S2.8. Cartoon model of receptor movement through the membrane architecture109

Figure S3.1. Instantaneous diffusion coefficient as a function of time for a single cell after treatment with 0.001 μg/ml DNP-BSA 124

Figure S3.2. Simultaneous measurements of QD-IgE diffusion and Ca2+ responses.... 125

Figure S3.3. Antigen-induced clustering occurs in the absence of downstream signaling 126

Figure S3.4. $IgE_{anti\text{-}dansyl}$ and $IgE_{anti\text{-}DNP}$ are specific for their designated antigens..... 127

Figure S3.5. Degranulation occurs under the same conditions as the hyperspectral microscopy experiment..... 128

List of Tables

Table 2.1. Median diffusion coefficients and actin overlap..... 30

Table 3.1. Median diffusion coefficients 71

CHAPTER 1: INTRODUCTION

1.1 The multichain immune recognition receptor family

The multichain immune recognition receptor family includes the B-cell receptor (BCR), T-cell receptor (TCR), and the high affinity IgE receptor (FcεRI) (Sigalov 2004). Given the key role that each of these receptor systems plays in mediating the delicate balance between health (via recognition and clearance of bacterial, viral, and parasitic infections) and disease (via induction of autoimmunity and allergy), it is not surprising that their signaling cascades are among the most well studied in all of biology (Sigalov 2004).

From these studies, many of the specific intracellular proteins involved in the signaling cascades downstream of these receptors have been identified. Subsequent to ligand binding, these intracellular proteins initiate kinase activation and Ca^{2+} mobilization, leading in turn to cytoskeletal reorganization, receptor trafficking and cell-specific responses, including cytokine production and altered gene expression (Boniface, Rabinowitz et al. 1998; Thyagarajan, Arunkumar et al. 2003; Kraft and Kinet 2007). In addition to the similarities among the signaling cascades of the BCR, TCR, and FcεRI, these receptors share a common mechanism of activation, in which oligomerization of multiple receptors via binding of multivalent ligand is required (Boniface, Rabinowitz et al. 1998; Thyagarajan, Arunkumar et al. 2003; Kraft and Kinet 2007). However, despite this extensive understanding of the requirements for and consequences of receptor activation, the precise mechanism by which multivalent engagement of receptors initiates signaling has remained elusive.

1.2 Overview of an allergic inflammatory response

When a person is first exposed to a putative allergen, the allergen will be taken up by antigen presenting cells (APCs) in the periphery, such as dendritic cells, macrophages, and B-cells. These cells will then process the allergen and express it on their surface as peptide fragments bound to major histocompatibility complex class II (MHC II). APCs with peptide-MHC (pMHC) complexes on their surface then travel to the lymph nodes, where they will interact with CD4+ T-cells. This interaction is mediated by antigen-specific TCR engagement with pMHC and also interaction of leukocyte function associated antigen 1 (LFA-1) integrins on T-cells with intercellular adhesion molecule 1 (ICAM-1) on the APC. This interaction produces a characteristic contact between APC and T-cell termed the immunological synapse (Dustin, Olszowy et al. 1998; Grakoui, Bromley et al. 1999). This interaction induces T-cell activation and proliferation, driven primarily by T-cell derived interleukin 2 (IL-2). If this interaction occurs in the presence of APC-derived IL-12, the proliferating T-cells will begin to secrete Th2-type cytokines, specifically IL-4, IL-5, and IL-13. These cytokines have a wide range of effects that serve to polarize the immune response away from the interferon-γ, IgG, macrophage-dominated response required for control of bacterial and viral infection, and toward the IgE, mast cell-dominated response associated with control of parasitic infection and also induction of allergy (Goldsby, Kindt et al. 2000).

In the presence of Th2 cytokines, B-cells, which become activated by multivalent engagement of their BCR by the putative allergen, will begin proliferating and undergo isotype switching to produce IgE (Vercelli 2002). This IgE will be secreted into the circulation by the activated B-cells, now called plasma cells, where it will encounter

FcεRI on the surfaces of basophils and also eventually make its way into tissues where it will bind to FcεRI on mast cells.

These mast cells and basophils are now said to be "primed" with allergen-specific IgE. Although IgE binding has several other important consequences (Kitaura, Song et al. 2003; Kawakami and Kitaura 2005), its main function is to confer mast cells and basophils with the ability to respond to allergen. Upon secondary exposure to allergen, often the next season in the case of seasonal allergies, the allergen binds to IgE-FcεRI complexes on the cell surface, triggering a complex signaling cascade that ultimately results in the release of pre-formed mediators of the allergic inflammatory response, stored in granules within the mast cells and basophils. Although variable depending on tissue distribution and species, these granules predominantly contain histamine, leukotrienes, prostaglandins, and serine proteases (Prussin and Metcalfe 2003). Once released into the surrounding tissue, these mediators induce the familiar symptoms of allergic disease: swelling, redness, irritation, mucus production, and bronchoconstriction (Prussin and Metcalfe 2003).

1.3 High Affinity IgE Receptor Overview

The high affinity IgE receptor is expressed on a wide range of cell types and can exist in two distinct forms. In its most well-studied form, FcεRI exists as a heterotetramer, consisting of a single membrane-pass α-subunit, which contains the IgE-binding domain, the four membrane-pass β-subunit, which contains a single immunoreceptor tyrosine-based activation motif (ITAM), and two γ-subunits, which exist as a disulfide-linked homodimer and also contain one ITAM on each subunit. In

addition to its well-known role as the principal receptor on the surface of mast cells and basophils, FcεRI can also exist in humans as a heterotrimer which lacks the β-subunit and is expressed in relatively lower numbers on several cell types, such as plasmacytoid and myeloid dendritic cells, Langerhans cells, monocytes, macrophages, eosinophils, and platelets (Kraft and Kinet 2007). In this heterotrimeric form, FcεRI is believed to function predominantly in antigen presentation, although other functions are currently under investigation (Kraft and Kinet 2007).

The α-subunit is heavily glycosylated, with seven N-linked glycosylation sites that are essential for proper folding and export from the endoplasmic reticulum (ER) (Letourneur, Sechi et al. 1995). The intracellular tail of the α-subunit has no known signaling function, whereas the two Ig-like domains of the extracellular portion are responsible for IgE-binding. These two domains interact asymmetrically with the two hydrophobic regions on the paired Cε3 domains of the Fc portion of IgE (Figure 1.1) (Garman, Wurzburg et al. 2000; Gould and Sutton 2008). This asymmetry not only explains the 1:1 binding stoichiometry between FcεRI and IgE, but also underlies the resulting high affinity ($K_D=10^{-10}$-10^{-11} M (Garman, Wurzburg et al. 2000)), since the two distinct binding interactions increase the avidity of the binding.

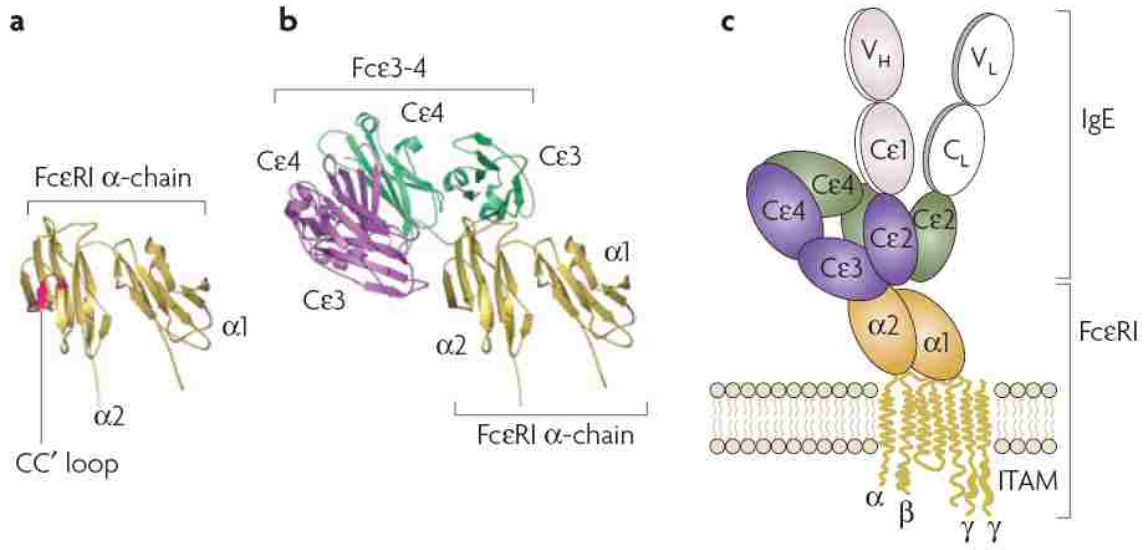

Figure 1.1 Structure of the alpha chain of FcεRI and its interaction with IgE. (a) Structure of the FcεRIα chain taken as it appears when co-crystallized with the Fcε3-4 domains of IgE. The CC' loop has shown some variability among different cystal structures of the FcεRIα extracellular chain and is shown in red. (b) Crystal structure of the extracellular domain of FcεRIα (gold) in complex with the Fcε3-4 domains of IgE (green and purple). (c) Cartoon of the full FcεRI tetramer in complex with IgE. Image taken from (Gould and Sutton 2008).

The β-subunit is a member of the tetraspanin family of proteins and contains a non-canonical ITAM in its C-terminal cytoplasmic tail (Donnadieu, Jouvin et al. 2003). The β-subunit associates with the core-glycosylated α-subunit while still in the ER and, along with the γ-subunit, facilitates transit of the receptor through the secretory pathway to the cell surface (Miller, Blank et al. 1989). Once at the cell membrane, the β-subunit ITAM associates with the SH2-domain containing Src-family kinases Lyn and Fyn; an association which transiently increases upon antigen-mediated activation of FcεRI (Gilfillan and Tkaczyk 2006).

The two γ-subunits have very short extracellular domains, are linked by a disulfide bond within the transmembrane domain, and contain a canonical ITAM in their cytoplasmic domain (Gilfillan and Tkaczyk 2006; Kraft and Kinet 2007). The γ-subunit also associates with the core-glycosylated α-subunit while still in the ER, masking an ER

retention signal on the α-subunit and permitting transit of the trimeric ($\alpha\gamma_2$) or tetramteric ($\alpha\beta\gamma_2$) receptor to the cell surface (Gilfillan and Tkaczyk 2006; Kraft and Kinet 2007). Once at the surface and upon activation, the γ-subunit ITAMs are responsible for the binding and activation of the spleen tyrosine kinase (Syk), which is the main driver of signaling downstream of the receptor (Gilfillan and Tkaczyk 2006; Kraft and Kinet 2007).

The interactions between subunits that stabilize the receptor in the membrane are poorly understood. However, it has been determined that electrostatic and hydrophobic interactions between covalently and non-covalently associated lipids are crucial to maintaining receptor integrity (Kinet, Quarto et al. 1985; Kinet 1999).

1.4 FcεRI Signaling

1.4.1 The FcεRI signaling cascade

In response to antigen-mediated aggregation of IgE-FcεRI on the cell surface, Lyn phosphorylates the ITAMs of the β and γ-subunits (Kraft and Kinet 2007). Given that Lyn is a dually acylated kinase (Xu, Harder et al. 2005), it has been suggested that Lyn's association with aggregated FcεRI is due to their antigen-induced colocalization in lipid rafts (Young, Zheng et al. 2005). However, recent studies have shown that interactions between FcεRI and Lyn require the presence of the SH2-domain of Lyn (Larson, Gosse et al. 2005), suggesting colocalization in lipid rafts is not sufficient to produce productive associations between FcεRI and Lyn.

After phosphorylation of FcεRIβ and γ ITAMs, a complex signaling cascade is initiated involving a series of membrane-associated and cytoplasmic proteins (Figure 1.2).

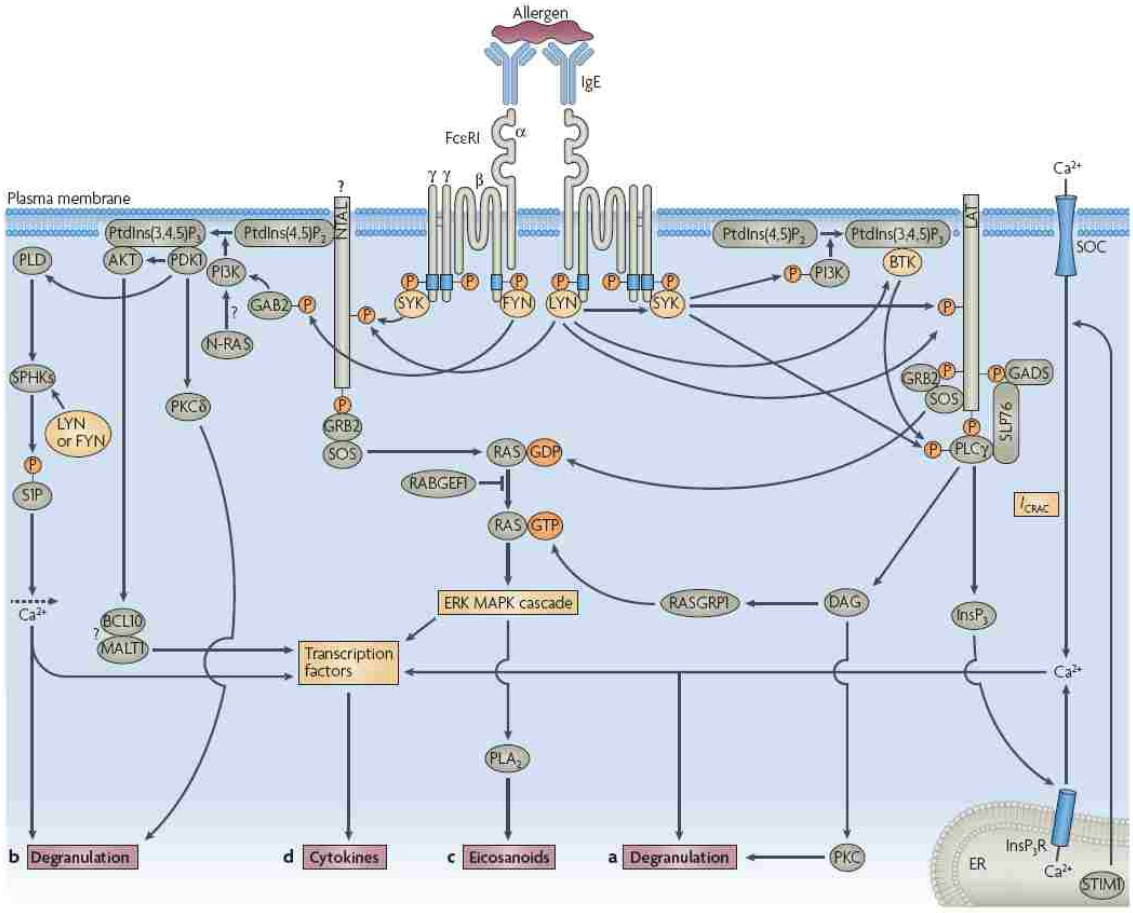

Figure 1.2 Schematic representation of FcεRI signaling. Taken from (Kraft and Kinet 2007).

The primary and most well-studied pathway involves signaling through Lyn. However, experiments in Lyn-deficient cell lines have revealed a secondary pathway through another Src family kinase, Fyn, which appears to primarily mediate degranulation. This complementary pathway is described in detail in (Kraft and Kinet 2007). In the primary (Lyn) pathway, Lyn-mediated ITAM phosporylation facilitates binding of Lyn and Syk to

FcεRIβ and FcεRIγ, respectively, through their SH2 domains. Lyn is then able to phosphorylate and activate Syk, initiating downstream signaling (Kraft and Kinet 2007). Once Syk is activated, it phosphorylates scaffolding proteins, such as SH2-domain containing leukocyte protein of 76 kD (SLP76) and linker for activation of T-cells (LAT). LAT is a transmembrane scaffolding protein which is able to scaffold growth factor receptor bound protein 2 (Grb2) through its SH2 domain. Grb2 can then interact with son of sevenless (Sos), which is a guanine nucleotide exchange factor for Ras, subsequently initiating the Ras-Raf-MAP kinase signaling cascade which results in altered gene transcription (cytokine synthesis) and also simulates the synthesis of eicosanoids via activation of phospholipase A-2. LAT and SLP76 also work in concert with Syk and Bruton's tyrosine kinase (Btk) to activate phospholipase Cγ (PLCγ). Once activated, PLCγ hydrolyzes phosphatidylinositoltrisphosphate lipids in the plasma membrane to produce diacylglycerol (DAG) and inositol-trisphosphate (IP3). IP3 binds to its receptor on the ER membrane, which simulates Ca^{2+} release from ER stores. The rise in cytoplasmic calcium has a wide range of effects, including acting in concert with DAG to activate protein kinase C (PKC); which, like Ca^{2+} itself, facilitates degranulation. This entire sequence of events is reviewed in (Kraft and Kinet 2007).

1.4.2 Role of topography in FcεRI signaling

In addition to the biochemical studies which have provided the framework for understanding the signaling cascade downstream of antigen binding, there is also a significant body of literature examining the spatial aspects of FcεRI signal initiation. An earlier study by the Oliver lab using scanning electron microscopy (SEM) showed characteristic patterns of FcεRI redistribution and clustering during signal transduction.

Specifically, FcεRI were observed to move off of actin-supported membrane ruffles and into large aggregates in response to crosslinking with anti-IgE antibodies (Seagrave, Pfeiffer et al. 1991). This study also demonstrated that small oligomers of FcεRI produced the most robust secretion, whereas larger aggregates appeared to be associated with a diminished secretory response (Seagrave, Pfeiffer et al. 1991).

More recently, high-resolution transmission electron microscopy (TEM) studies using immunogold labeling have enhanced the understanding of the role of receptor topography in FcεRI signaling. These studies have shown that FcεRI, a protein with no known homotypic interactions, exists in small clusters on the surface of unstimulated cells (Figure 1.3A). It was also determined that about 25% of these small clusters are associated with the Src-family kinase, Lyn (Wilson, Pfeiffer et al. 2000). A separate study using chemical cross-linking arrived at a similar estimate (3-20%) of the extent of Lyn association with non-activated FcεRI (Yamashita, Mao et al. 1994). Treatment of cells with a multivalent antigen (DNP-BSA) produced similar effects as seen with anti-IgE-mediated activation of FcεRI: FcεRI redistributed into larger clusters, which were associated with coated pits (Figure 1.3B). These clusters also contained the downstream signaling molecule Syk (Wilson, Pfeiffer et al. 2000).

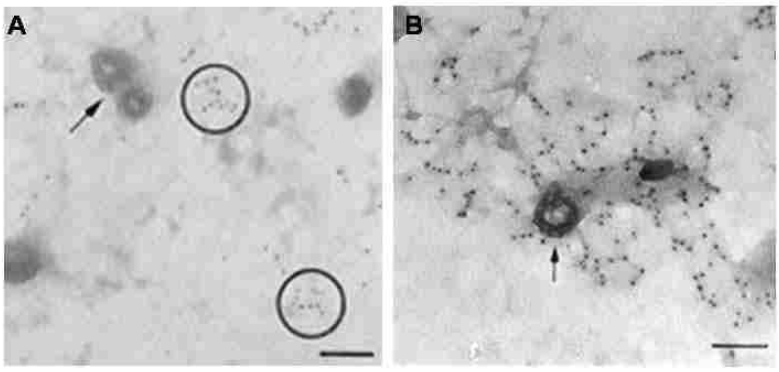

Figure 1.3 FcεRI is distributed nonrandomly on resting and activated mast cells. Membrane sheets were prepared from RBL-2H3 cells before (A) or after (B) cross-linking the FcεRI with DNP-BSA or anti-IgE. The FcεRI ß subunit was labeled from the inside of the membrane using 5-nm gold particles conjugated to anti-FcεRI ß mAb. 5-nm gold particles marking FcεRI ß are distributed in small dispersed clusters and strings (circled) in the membranes of resting cells (A) and as larger clusters in the membranes of IgE-primed cells that were activated for 2 min at 37°C with DNP-BSA (B). Bars = 0.1 µm. Figure adapted from (Wilson, Pfeiffer et al. 2000).

A detailed analysis of the process of clustering and the extent of association with downstream signaling molecules produced a topographical model of FcεRI signal initiation. In this model, antigen binding causes the small, partially Lyn-associated FcεRI clusters to coalesce into larger clusters, of which clusters containing less then 20 FcεRI associate with Lyn, whereas larger clusters (20-100 FcεRI) exclude Lyn and begin to associate with Syk and clathrin-coated pits (Figure 1.4) (Wilson, Pfeiffer et al. 2000).

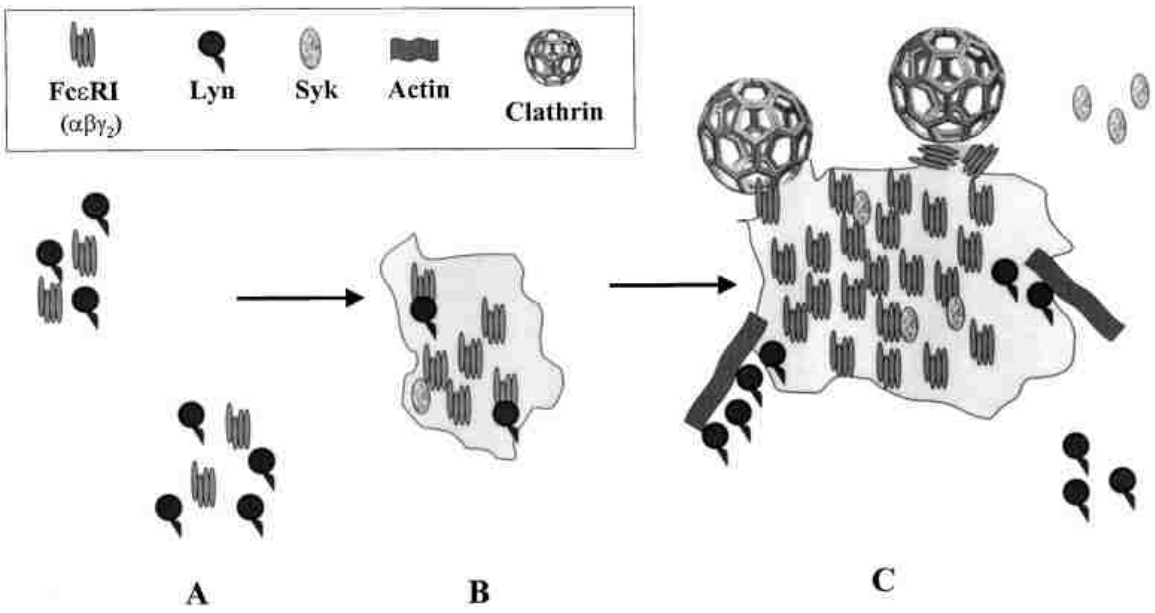

Figure 1.4 Schematic representation of topographical progression of FcεRI signaling. (A) FcεRI is distributed as monomers and small clusters and partially associated with Lyn in the absence of multivalent antigen. (B) Upon stimulation, FcεRI coalesce into larger clusters which begin to recruit Syk. (C) As signaling progresses, the clusters continue to grow in size and largely exclude Lyn while retaining Syk. These large clusters are often associated with coated pits. Taken from (Wilson, Pfeiffer et al. 2000).

The high spatial resolution of EM-based studies has enabled discoveries that highlight the important role played by receptor topography in antigen-induced FcεRI signaling. However the inherently low temporal resolution and extensive fixation required for EM imaging make this technique unsuitable for probing the dynamic behavior of FcεRI as signaling is initiated.

1.4.3 Role of dynamics in FcεRI signaling

Fluoresence microscopy of living cells has contributed significantly to the understanding of the relationship between FcεRI dynamics and signaling. A series of studies using fluorescence recovery after photobleaching (FRAP) (Schlessinger, Webb et al. 1976; McCloskey, Liu et al. 1984; Menon, Holowka et al. 1986; Mao, Varin-Blank et al. 1991; Thomas, Feder et al. 1992; Feder, Chang et al. 1994; Feder, Brust-Mascher et al.

1996; Born and Wolf 1997; Pyenta, Schwille et al. 2003) and time-resolved phosphorescence anisotropy (TPA) (Zidovetzki, Bartholdi et al. 1986; Rahman, Pecht et al. 1992; Feder, Chang et al. 1994) established that non-cross-linked, IgE-bound receptors are relatively free to diffuse across the cell surface and that antigen binding leads to receptor immobilization within two minutes (Menon, Holowka et al. 1986). Through the use of IgE-oligomers of varying sizes, FRAP studies have also shown that larger oligomers result in larger immobile fractions of FcεRI and that larger immobile fractions correlate with a greater extent of degranulation (Menon, Holowka et al. 1986), complementing the insights provided by SEM (Seagrave, Pfeiffer et al. 1991). It has been shown that treatment with even small oligomers of IgE produces large aggregates that are visible at the resolution of the light microscope (Menon, Holowka et al. 1984). The formation of these clusters is therefore not believed to be due solely to crosslinking individual FcεRI into large aggregates, but is instead thought to be facilitated by interactions with other components of the cell membrane (Menon, Holowka et al. 1986).

The model that emerges from these studies is that crosslinking of receptors into small oligomers sends a signal to the cell that facilitates their reorganization into larger signaling domains where kinase recruitment occurs. While the EM-based studies were limited by their low temporal resolution, the fluorescence-based techniques are limited in their spatial resolution and therefore do not provide information about the dynamic behavior of groupings of FcεRI smaller than 200 nm in size, including individual receptors.

1.5 Single Particle Tracking

1.5.1 Single Particle Tracking Overview

Live cell imaging techniques capable of sub-200 nm resolution are required to determine the characteristics of crosslinked FcεRI oligomers that putatively signal the cell to initiate reorganization of FcεRI into signaling domains. Single particle tracking (SPT) provides the necessary spatial and temporal resolution to acquire information on the diffusion characteristics of single molecules and permits correlation of the activation state of FcεRI with their spatial distribution and dynamics.

In this technique, a target of interest is labeled with a polystyrene bead, colloidal gold particle, or fluorophore (organic dye or genetically encoded fluorescent protein). This is typically accomplished through conjugation of the label to an antibody against the target molecule. The target molecule is then labeled at a very low density, such that only a few are labeled on any given cell (Saxton and Jacobson 1997). At this low density, individually labeled target molecules remain well-separated and can therefore be easily distinguished and tracked. Tracking is achieved by imaging live, labeled cells at rapid frame rates (typically >4 frames per second) either by transmitted light (in the case of polystyrene beads or colloidal gold particles) or by fluorescence microscopy. The transmitted light techniques have the advantage of producing high signal-to-noise images, enabling very rapid imaging rates (up to 40,000 frames per second (Murase, Fujiwara et al. 2004)) and can also be used to follow single molecules for long time periods, since photobleaching is not a problem. However, these techniques require relatively large probes (40 nm for colloidal gold up to several microns for polystyrene beads) which can significantly alter the diffusion of the target molecule due not only to their size, but also due to the multivalent nature of their binding (Saxton and Jacobson 1997). By

comparison, organic fluorophores or genetically encoded fluorescent tags are much smaller (1-4 nm), however the signal-to-noise ratio is not as favorable as in the transmitted light techniques, necessitating slower imaging rates, and photobleaching limits the imaging duration (Harms, Cognet et al. 2001; Ueda, Sako et al. 2001).

In addition to facilitating rapid imaging of live cells, SPT also enables individual molecules to be localized with sub-diffraction limited resolution. The lateral resolution of the light microscope is traditionally considered to be ~250 nm (λ/2) (James 1976). Due to this fundamental limitation, isolated objects smaller than 250 nm, so called "point-source emitters", will appear as diffraction limited spots. These diffraction limited spots can be fit by a 2D Gaussian function which returns the center of the spot and a measure of the accuracy of this determination (Equation 1.1) (Jonas, Yao et al. 2006).

$$\sigma_\mu = \sqrt{\left(\frac{\sigma_0^2}{N} + \frac{\frac{a^2}{12}}{N} + \frac{8\pi\sigma_0^4 b^2}{a^2 N^2}\right)}$$

Equation 1.1 Equation describing the localization accuracy of a 2D Gaussian fit to a point source emitter. The standard error of the mean (σ_μ) is related to the number of collected photons (N), the width of the Gaussian distribution (σ_0), the effective pixel size (a), and the standard deviation of the background (b). Taken from (Jonas, Yao et al. 2006).

Using this method under conditions of very high signal-to-noise, particles can be localized to within 1 nm (Jonas, Yao et al. 2006); however the long integration times required to achieve this level of accuracy are not practical for imaging diffusing proteins in live cells. Therefore, a compromise between localization accuracy and frame rate must be reached based upon the goals of any given experiment. SPT algorithms incorporating this method of particle localization have been demonstrated to be superior to other methods in the low signal-to-noise (S:N<4) conditions typically encountered when using

fluorescent probes and the relatively rapid frame rates required to obtain meaningful information about diffusion of the target molecule (Cheezum, Walker et al. 2001).

Once the appropriate labeling and imaging conditions are determined, a time series of images of the labeled, live cells can be obtained. This raw image series then serves as the input for a SPT algorithm, which performs the 2D Gaussian fit to each diffraction limited spot in the image series. This yields a set of XY coordinates for each image in the series, which can then be assembled into trajectories for each labeled molecule (Saxton and Jacobson 1997). An example of a simulated trajectory for a single molecule obtained by imaging at 30 frames per second for 30 seconds is shown in Figure 1.5A. A trajectory can also be represented as a plot of the mean square of the displacement (MSD) versus the time interval (Δt) (Figure 1.5B). This way of representing the data enables it to be fit by different equations which describe the various types of motion that have been observed for molecules diffusing in the cell membrane (Figure 1.5B) and also facilitates calculation of the diffusion coefficient (D). A detailed explanation is provided in Appendix A.

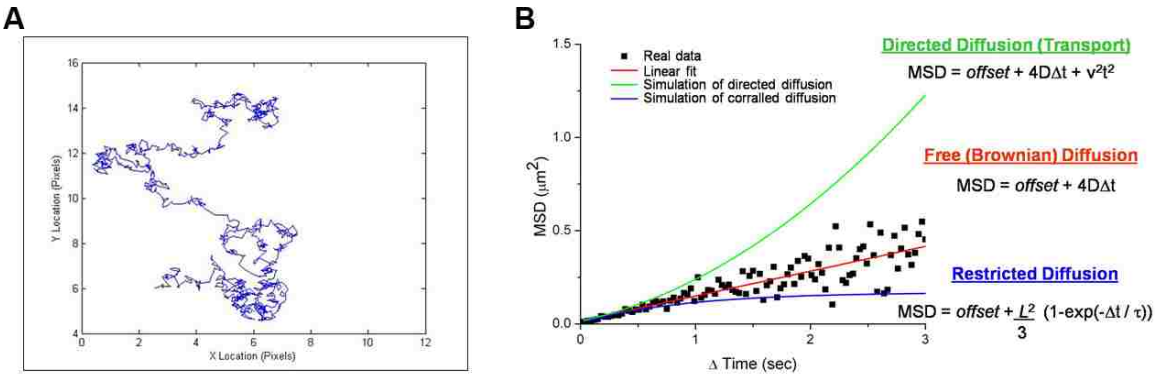

Figure 1.5 Mean square displacement plots. (A) Example of a trajectory for a single molecule undergoing free (Brownian) diffusion. (B) Example of an MSD plot for a single molecule undergoing free diffusion (black squares) and its fit (red line) along with fits to simulations representing directed diffusion (green line) or restricted diffusion (blue line). The equations used to fit the data for the three types of motion are shown at right. The *offset* term is related to the localization accuracy (Martin, Forstner et al. 2002), D is the diffusion coefficient, Δt is the time interval, v is the velocity of the transport process, t is time, L describes the area of the region in which the restricted diffusion occurs, and τ is the correlation time. The equations for directed and free diffusion were adapted from (Kusumi, Sako et al. 1993), and the equation for restricted diffusion from (Destainville and Salome 2006).

1.5.2 Single Particle Tracking of FcεRI

While FcεRI signaling has been examined previously by SPT, these studies were rather narrow in scope and suffered from some important limitations related to the probes used. Previous SPT studies of FcεRI diffusion employed low density lipoprotein (LDL) particles labeled with the fluorescent lipid 1,1'-dioctadecyl-3,3,3',3'-tetramethylindo-carbocyanine (diI) (Feder, Brust-Mascher et al. 1996) or colloidal gold probes (Barisas, Smith et al. 2007). While providing important information on the behavior of individual FcεRI, these measurements suffered from long integration times (1.6 s per image in the case of the diI-LDL studies), large (>40 nm) particle size, and labeling or tracking at nonphysiological temperatures (i.e. 4°C and room temperature). The use of cold (4°C) labeling conditions in studies of FcεRI dynamics is of particular concern since long

duration cold labeling has since been shown to yield significant decreases in measured diffusion of other transmembrane proteins (Suzuki, Ritchie et al. 2005).

1.5.3 Quantum Dots for SPT

Recently, quantum dots (QDs) have been demonstrated to be useful probes for SPT due to their relatively small size (5-20 nm) compared to colloidal gold (30-50 nm), as well as their large extinction coefficients and robust photostability compared to organic fluorophores (Dahan, Levi et al. 2003; Lidke, Lidke et al. 2005). These properties allow single molecules to be imaged over long time periods and at rapid acquisition rates with a minimum of interference from the probe itself (Dahan, Levi et al. 2003). Additionally, the broad absorption and narrow emission spectra of QDs facilitates the simultaneous tracking of multiple proteins of interest through multi-color labeling (Dahan, Levi et al. 2003; Lidke, Nagy et al. 2004; Lidke, Lidke et al. 2005).

In addition to simultaneously tracking multiple targets, multi-color labeling can also be used to increase the labeling density of a single target while still maintaining single particle resolution (Esa, Edelmann et al. 2000). The ability of SPT to localize individual particles with sub-wavelength resolution is dependent upon low density labeling, such that particles remain separated by at least 200 nm (Saxton and Jacobson 1997). Tracking in multiple colors enables the labeling density for any one color to remain low, while the overall concentration of label can be increased in direct proportion to the number of colors used. In this case, the labeling density is limited by the number of emission species that can be reliably distinguished by the imaging system. In the context of FcεRI signal initiation, multi-color SPT provides a method for examining the

dynamic behavior of the small FcεRI clusters previously visible only in the static images of EM.

1.6 Hypothesis: Changes in FcεRI diffusion and topography serve to initiate FcεRI signaling.

A large number of studies over the past 30 years have examined the lateral mobility of the high affinity IgE receptor (Schlessinger, Webb et al. 1976; McCloskey, Liu et al. 1984; Menon, Holowka et al. 1986; Zidovetzki, Bartholdi et al. 1986; Mao, Varin-Blank et al. 1991; Rahman, Pecht et al. 1992; Thomas, Feder et al. 1992; Feder, Chang et al. 1994; Feder, Brust-Mascher et al. 1996; Born and Wolf 1997; Pyenta, Schwille et al. 2003). However, few of these studies went beyond determining the diffusion coefficient and all of them were conducted at non-physiological temperatures. A subset of these studies measured FcεRI mobility before and at least two minutes after exposure to a single, relatively high dose of multivalent antigen and all reported a dramatic decrease in FcεRI mobility (Menon, Holowka et al. 1986; Zidovetzki, Bartholdi et al. 1986; Mao, Varin-Blank et al. 1991; Pecht, Ortega et al. 1991; Rahman, Pecht et al. 1992; Pyenta, Schwille et al. 2003). A further subset found a correlation between an activating agent's ability to immobilize FcεRI and the extent of degranulation it induced (Menon, Holowka et al. 1986; Pecht, Ortega et al. 1991). The only study to employ a low, yet still activating dose of cross-linking agent reported that FcεRI remained mobile after cross-linking (Schlessinger, Webb et al. 1976). Despite this one seemingly aberrant result, the overall picture of FcεRI signal initiation that emerged from these studies was that immobilization of FcεRI strongly correlated with cell activation.

Given this concept, we hypothesized that changes in FcεRI diffusion and topography serve to initiate FcεRI signaling. More specifically, we proposed that immobilization of FcεRI was the inciting event which triggered a cellular response and induced downstream signaling and large-scale reorganization of FcεRI into large aggregates on the cell surface. To address this hypothesis, we developed and implemented novel live-cell imaging techniques and QD based probes to rigorously assess the diffusion and topography of FcεRI in the context of signal initiation. Through the following series of experiments, we describe a new role for the actin cytoskeleton in influencing diffusion of transmembrane proteins on micron length scales, quantify the kinetics and dose dependence of antigen-induced immobilization and clustering of FcεRI, and elucidate the role of receptor dynamics in FcεRI signaling. In the end, we determined that our results contradicted the original hypothesis, prompting us to propose a new paradigm for the role of receptor dynamics in FcεRI signaling.

CHAPTER 2: ACTIN RESTRICTS FCεRI DIFFUSION AND FACILITATES ANTIGEN-INDUCED RECEPTOR IMMOBILIZATION

Actin restricts FcεRI diffusion and facilitates antigen-induced receptor immobilization

Nicholas L. Andrews[1,4], Keith A. Lidke[2,3,4], Janet R. Pfeiffer[1], Alan R. Burns[3], Bridget S. Wilson[1], Janet M. Oliver[1], and Diane S. Lidke[1]

[1]Department of Pathology and Cancer Research and Treatment Center and [2]Department of Physics and Astronomy, University of New Mexico, Albuquerque, New Mexico 87131; [3]Sandia National Laboratories, Albuquerque, New Mexico 87185-0351

[4]These authors contributed equally to this work.

Published in *Nature Cell Biology.* 2008 Aug;10(8):955-63.

Correspondence should be addressed to D.S.L. (e-mail: dlidke@salud.unm.edu)

Abbreviations: BSA, bovine serum albumin; COM, center of mass; DNP, 2,4-dinitrophenol; EM, electron microscopy; FcεRI, high affinity IgE receptor; FRAP, fluorescence recovery after photobleaching; MSD, mean square displacement; QD, quantum dot; SPT, single particle tracking; TIRF, total internal reflection fluorescence; TPA, time-resolved phosphorescence anisotropy

2.1 ABSTRACT

The actin cytoskeleton has been implicated in restricting diffusion of plasma membrane components. Here, simultaneous observations of quantum dot-labelled FcεRI motion and GFP-tagged actin dynamics provide direct evidence that actin filament bundles define micron-sized domains that confine mobile receptors. Dynamic reorganization of actin structures occurs over seconds, making the location and dimensions of actin-defined domains time dependent. Multiple FcεRI often maintain extended close proximity without detectable correlated motion, suggesting that they are co-confined within membrane domains. FcεRI signaling is activated by cross-linking with multivalent antigen. We show that receptors become immobilized within seconds of cross-linking. Disruption of the actin cytoskeleton results in delayed immobilization kinetics and increased diffusion of cross-linked clusters. These results implicate actin in membrane partitioning that not only restricts diffusion of membrane proteins, but also dynamically influences their long-range mobility, sequestration, and response to ligand binding.

2.2 INTRODUCTION

Signal transduction from the external environment to the cell interior is typically mediated by ligand-bound transmembrane receptors embedded in a lipid bilayer. In many systems, receptor activation is associated with changes in receptor dynamics and membrane topography (Dustin and Cooper 2000; Lidke, Lidke et al. 2005; Zhang, Leiderman et al. 2006). Among these are the multichain immune recognition receptor family members that include the B-cell receptor (BCR) of B-cells, the T-cell receptor (TCR) of T-cells, and the high affinity IgE receptor (FcεRI) of mast cells and basophils, which are crucial to the execution of key events in the immune response. Cross-linking of these transmembrane receptors induces receptor oligomerization, protein and lipid kinase activation and Ca^{2+} mobilization, leading in turn to cytoskeletal reorganization, receptor trafficking and cell-specific responses including altered gene expression (Boniface, Rabinowitz et al. 1998; Thyagarajan, Arunkumar et al. 2003; Kraft and Kinet 2007). These signaling events have been well studied by biochemical techniques, but the precise mechanism by which oligomerization initiates these events has remained elusive. Full understanding of these complex signaling cascades will require a more complete description of receptor movements in the membrane, including restrictions that might limit receptor diffusion and accessibility.

A rich literature on single particle tracking (SPT) methods to follow the lateral diffusion of transmembrane and membrane-associated proteins (Saxton and Jacobson 1997; Murase, Fujiwara et al. 2004; Kusumi, Ike et al. 2005; Ritchie, Shan et al. 2005) has revealed nanometer-scale "confinement zones" that restrict lateral diffusion and supports the general notion that plasma membrane organization is more structured than

originally postulated by the fluid mosaic model (Singer and Nicolson 1972). A membrane-skeleton fence (picket fence) model has been proposed to explain confined diffusion (Jacobson, Sheets et al. 1995; Kusumi, Nakada et al. 2005) at the scale of nanometers and microseconds. In this model, a relatively static meshwork of actin-defined domains transiently retain diffusing membrane proteins and lipids, leading to apparent long time-scale diffusion rates that are much slower than those measured in artificial lipid bilayers. A recent comparison of high resolution electron microscopy (EM) images of cytoskeletal "ghosts" with high-speed SPT data demonstrates that nanometer-sized transient confinement zones measured by SPT correlate well to regions delimited by membrane-associated cortical cytoskeleton visualized by EM (Morone, Fujiwara et al. 2006). However, technical limitations preclude simultaneous SPT and direct observation of nanometer-scale actin structures in living cells, leaving the precise mechanism of restricted diffusion at the nanometer scale open to debate. Specifically, other structural features in membranes, such as lipid rafts or protein islands (Draber and Draberova 2002; Douglass and Vale 2005; Frankel, Pfeiffer et al. 2006; Lillemeier, Pfeiffer et al. 2006), have also been suggested to affect lateral diffusion.

Here, we directly characterize transmembrane receptor diffusion with respect to actin by simultaneous fluorescence imaging of *micron-scale* features of the cortical actin cytoskeleton and FcεRI. Quantum dot (QD)-labelled IgE was used to tag FcεRI. IgE binds tightly to the α subunit of FcεRI, essentially becoming another subunit of the receptor (Kulczycki and Metzger 1974; Garman, Wurzburg et al. 2000). Exploiting this tight binding enables labeling of the resting receptor with minimal disruption to normal cell physiology, providing a highly specific and relevant probe of receptor dynamics and

membrane topography. Micron scale features of the actin-based cytoskeleton have been described in detail using EM of detergent-extracted platelets (Hartwig and DeSisto 1991). We sought to visualize large membrane-proximal actin bundles in RBL-2H3 cells using GFP-tagged actin with confocal and total internal reflection fluorescence (TIRF) microscopy. We provide direct evidence that actin cables near the membrane define regions that limit receptor diffusion. These structures do not provide a static meshwork of enclosed domains, but instead form a dynamic labyrinth defined by micron-scale actin barriers that reorganize over time scales of 1-10 seconds. In contrast to the putative transient confinement zones of the picket fence model, here we describe a phenomenon that occurs in time scales of seconds and over distances of microns. In addition to restriction of membrane protein diffusion, we provide evidence that actin-based membrane partitioning dynamically influences long-range mobility, sequestration and response to ligand binding.

2.3 RESULTS

2.3.1 QD-IgE is functionally monovalent

A monovalent QD-IgE probe was developed in order to study properties of the resting IgE receptor, FcεRI. The reaction conditions were carefully controlled to produce functionally monovalent complexes of QD with $IgE_{anti\text{-}DNP}$ (QD-IgE; see Materials and Methods). Several approaches were taken to evaluate valency (see Materials and Methods, Appendix A, Fig. S2.1). For functional evaluation, we determined that QD-IgE did not induce substantial activation of RBL-2H3 cells assessed by confocal microscopy

as a lack of ruffle formation and QD-IgE internalization (Fig. 2.1a; top panels) and by degranulation assay as a lack of β-hexosaminidase release (Fig. 2.1b). In addition, QD-IgE primed cells were capable of responding to stimulation with the multivalent antigen DNP-BSA. This was demonstrated visually as cell ruffling and QD-IgE internalization (Fig. 2.1a, bottom panels and Appendix A, Video 2. 1) and biochemically as significant β-hexosaminidase release (Fig. 2.1c). The somewhat blunted secretory response of QD-IgE primed cells (Fig. 2.1c) is likely due to steric limitations that the QD label imposes on the IgE-FcεRI aggregates (Ortega, Schweitzer-Stenner et al. 1988).

Since QDs can serve as probes in both EM and fluorescence imaging (Giepmans, Deerinck et al. 2005), we analysed the topography of QD-IgE-tagged receptors on native membrane sheets by TEM. A visual inspection of QD distribution on the sheets shows many singlets as well as small clusters of 20-40 nm in size (Fig. 2.1d), verified as statistically nonrandom by the Hopkins test (Fig. 2.1d; inset). These results are consistent with previous studies using immunogold (Wilson, Pfeiffer et al. 2000; Zhang, Leiderman et al. 2006) and confirm that previously observed clustering of resting receptors cannot be trivially explained as an artifact of the multivalent gold probes used to label fixed cell membranes (described in (Kusumi, Ike et al. 2005)). Brief treatment of QD-IgE labelled cells with polyvalent antigen results in the formation of large clusters of receptors (Fig. 2.1e), as well as the appearance of QD-labelled receptors in clathrin coated pits (Fig. 2.1e, upper inset). These studies demonstrate that QD-IgE behaves comparably to unlabelled IgE and therefore serves as a reliable probe of IgE-FcεRI dynamics.

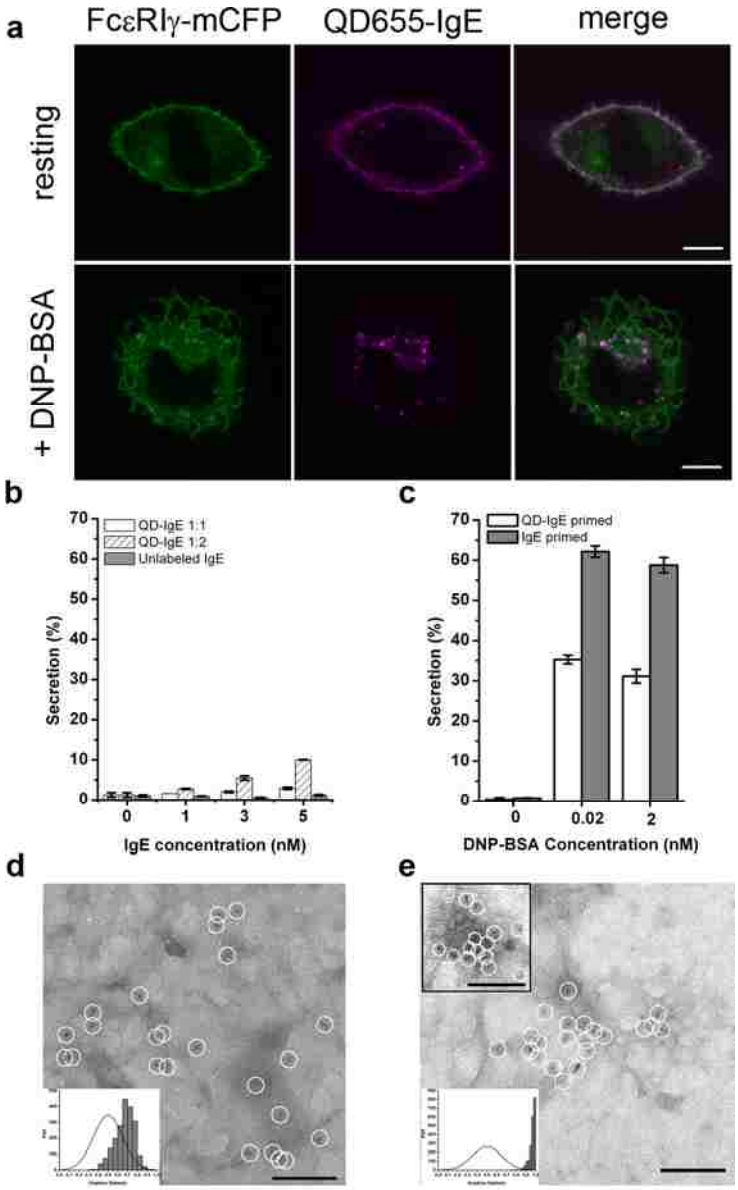

Figure 2.1 QD-IgE serves as a non-perturbing probe of FcεRI diffusion. (**a**) RBL-2H3 cells stably expressing FcεRI-gamma-mCFP were labelled with 1 nM QD655-IgE and then imaged (top panels) or cross-linked with 14 nM DNP-BSA for 10 min prior to imaging (bottom panels). (**b,c**) Degranulation assay plots showing the percentage of total β-hexosaminidase content secreted in response to 30 min incubation at 37°C with various IgE (**b**) or after priming with QD-IgE or IgE in response to various amounts of DNP-BSA (**c**). (**d**,**e**) Individual QD655-IgE-FcεRI are indicated by white circles in electron micrographs from membrane sheets prepared from RBL-2H3 cells labelled with QD655-IgE (**d**) and stimulated for 10 min with 14 nM DNP-BSA (**e**) before fixation. A right shift in the experimental data (grey bars) away from a random distribution (solid line) in the Hopkins plot indicates a slightly clustered distribution of QD655-IgE-FcεRI in the resting state (**d**, inset) and a highly clustered distribution after cross-linking (**e**, inset)(Zhang, Leiderman et al. 2006). The scale bars represent 10 μm in **a** and 100 nm in **d** and **e**.

2.3.2 QD-IgE-FcεRI demonstrates characteristic membrane protein diffusion

Estimations of membrane protein diffusion are variable, depending on differences in acquisition rates, temperature and the method of measurement. For example, imaging at ambient temperatures is simpler, but the diffusion rate is slower than at physiological temperatures. The frequent use of cold (4°C) labeling conditions in studies of FcεRI dynamics (Feder, Brust-Mascher et al. 1996; Barisas, Smith et al. 2007) is of particular concern because long duration cold exposure has been shown to decrease measured diffusion of other transmembrane proteins (Suzuki, Ritchie et al. 2005). We compared the diffusion of QD-IgE-FcεRI at room temperature (22°C) and at 35°C and observed a faster diffusion coefficient (D) and larger restricted region of diffusion (L) at the higher temperature (Appendix A, Fig. S2.2). To avoid these potentially confounding effects, we labelled cells and acquired data at physiological temperatures (34-37°C). The median diffusion coefficient ($D_{1\text{-}3}$), measured at video rate (33 frames/s), was 0.074 $\mu m^2/s$ (Table 2.1). This value is consistent with previous measurements performed at lower temperatures (D = 0.02-0.05 $\mu m^2/s$ (Schlessinger, Webb et al. 1976; Thomas, Feder et al. 1992; Feder, Brust-Mascher et al. 1996; Pyenta, Schwille et al. 2003; Barisas, Smith et al. 2007)).

As documented in previous studies of other membrane proteins (Kusumi, Sako et al. 1993; Daumas, Destainville et al. 2003; Murase, Fujiwara et al. 2004; Suzuki, Ritchie et al. 2005; Jacquier, Prummer et al. 2006; Barisas, Smith et al. 2007), we observed four distinct modes of FcεRI diffusion in unstimulated cells: free, directed, restricted, and immobile (Appendix A, Fig. S2.3). Our observation of restricted and immobile receptors

is consistent with the general notion that the plasma membrane contains structures that limit lateral diffusion, which are not present in artificial bilayers.

Table 2.1. Median diffusion coefficients and actin overlap

Imaging Condition	Cell Treatment	N	D_{1-3} ($\mu m^2/s$)[a]	IQR[c]	Relative Actin Overlap[d]
Apical	resting	236	0.074	0.065	
Apical	Latrunculin B	138	0.10	0.087	
Apical	DNP-BSA	647	0.010	0.038	
Apical	Latrunculin B + DNP-BSA	403	0.020	0.044	
TIRF	resting	303	0.077[b]	0.074	1.43
TIRF	Latrunculin B	265	0.059[b]	0.067	1.30
TIRF	PMA	102	0.075[b]	0.078	1.32

[a] D_{1-3} values were calculated as described in 2. 5 Materials and Methods. Values are reported as median.

[b] Median D_{1-3} values from TIRF experiments were calculated after excluding "immobile" trajectories, defined as $D_{1-3} \leq 0.0009$ mm^2/s.

[c] Interquartile Range (IQR), see Materials and Methods.

[d] Ratio of actin crossings between simulated and real trajectories. A value > 1 indicates that simulated, freely-diffusing particles cross actin more frequently than real trajectories. The differences in behavior between real and simulated data are statistically significant (see text and Appendix A for details).

2.3.3 Receptors are co-confined in micron-scale membrane domains

Despite labeling conditions that resulted in only a few QD-IgE labeled receptors per cell, we often observed prolonged overlap between the emissions of two or three tracked receptors (Appendix A, Video 2. 2). These observations raised the possibility that weak attractive interactions may exist between non-cross-linked receptors. However,

when two QDs with the same emission spectra overlap, they cannot be easily distinguished until they separate. Thus, the analysis of close interactions between receptors is limited in protocols using only one color of fluorophore.

We overcame this limitation by labeling cells with a mixture of QD585-IgE and QD655-IgE and simultaneously tracking both QDs. This allowed us to independently localize each molecule even when their emissions overlapped. In the example shown in Figure 2a-c, two QD-labelled receptors repeatedly approach each other to within our localization limits (see Materials and Methods) while never moving farther than 500 nm apart before coming back together (Fig. 2.2c). Despite their close proximity, the trajectories of the two molecules do not appear to be correlated (Fig. 2.2b). In the second example (Fig. 2.2d-f), a maximum separation of 2 μm occurs before the two molecules come back together (Fig. 2.2f). The observation that QD-IgE-FcεRI complexes can move microns apart before seeming to reverse direction to rejoin each other cannot be explained by attractive forces between the observed receptors.

To determine if protein-protein interactions (i.e., transient dimerization) could explain the prolonged colocalization of QD-IgE-FcεRI complexes, we developed mathematical analyses to quantify coordinated movement between receptors at separation distances less than 500 nm (see Supplementary Methods). In order to capture these potentially highly dynamic events, we used TIRF microscopy with a faster acquisition rate of 100 frames/s. The analysis involves measuring the magnitude of a receptor's displacement vector (jump magnitude) and the extent of correlated motion between nearby receptors (uncorrelated jump distance). If two receptors form a transient dimer, their diffusion is expected to be slowed (Kusumi, Nakada et al. 2005), producing a

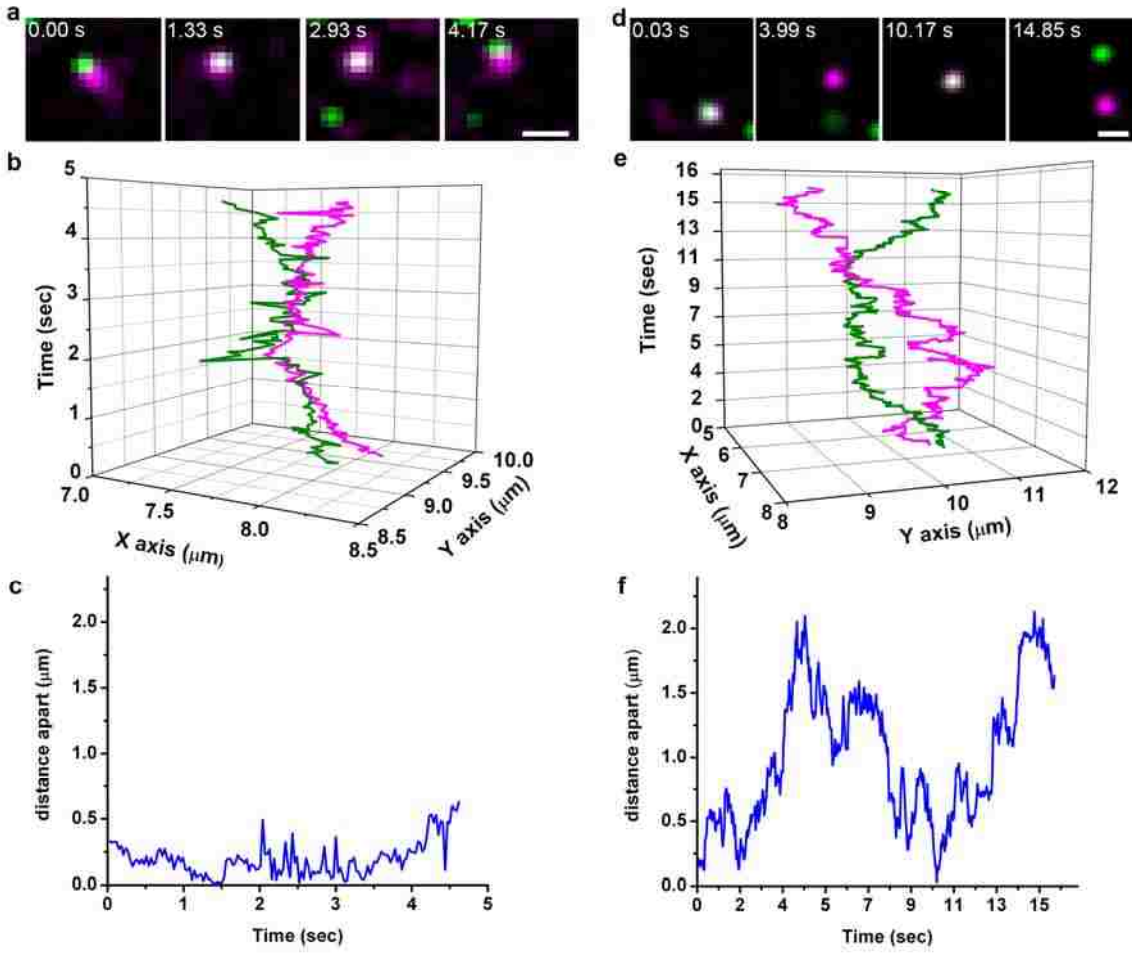

Figure 2.2 FcεRI are co-confined. (**a**) Sample images from a time series showing two QD-IgE-FcεRI complexes co-confined within a ~500 nm domain. (**b**) XY versus time plot of trajectories of QD655-IgE-FcεRI (magenta) and QD585-IgE-FcεRI (green) from time series shown in **a**. (**c**) Plot of interparticle distance versus time for particles shown in **a**. (**d**) Sample images from a time series showing two QD-IgE-FcεRI complexes co-confined within a ~2 μm domain. (**e**) XY versus time plot of trajectories of QD655-IgE-FcεRI (magenta) and QD585-IgE-FcεRI (green) from time series shown in **d**. (**f**) Plot of interparticle distance versus time for particles shown in **d**. Images in **a** and **d** have been Gaussian filtered. Images were acquired on the apical surface at 33 frames/s. The scale bars represent 1 μm in **a** and **d**.

decrease in their jump magnitude. Additionally, if two receptors are forming a transient dimer, they would move together during the lifetime of this dimer; i.e., the motion of the two interacting receptors would be correlated, producing a decrease in the uncorrelated

jump distance. By plotting the jump magnitude and the uncorrelated jump distance as a function of distance between receptor pairs, we can detect the presence of transient dimers, provided their lifetime is longer than the acquisition time for each image (10 ms).

To model the observed behavior of prolonged colocalization, we performed simulations of diffusing particles which formed transient dimers for 200 ms when two particles approached within 25 nm (see Appendix A, Fig. S2.4). This produced a dramatic decrease in the uncorrelated jump distance as receptors came close enough to interact (Appendix A, Fig. S2.4). In contrast to the simulations, analysis of real trajectories produced only gradual decreases in the jump magnitude (Fig. 2.3, open circles) and the uncorrelated jump distance (Fig. 2.3, x-marks). The weak dependence of these values on separation distance is consistent with measuring a slower diffusion constant when particles are confined in a small region (as described in (Ritchie, Shan et al. 2005)). Together, these analyses do not support transient dimer formation as a mechanism for the prolonged colocalization we observed and instead suggest co-confinement by membrane structure as the most likely explanation.

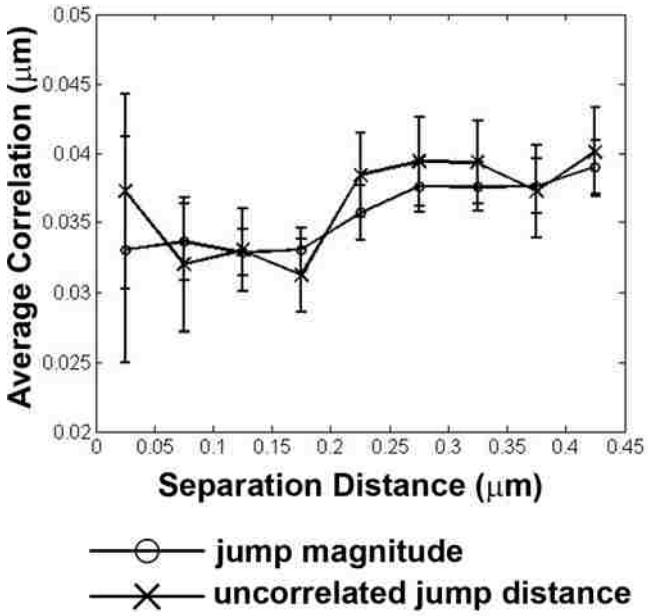

Figure 2.3 Motion of QD-IgE-FcεRI is consistent with co-confinement; not attraction. Mean distance of uncorrelated jump distance (x-marks) and jump magnitude (open circles) plotted as a function of distance between QD-IgE-FcεRI complexes. Data are presented as mean ± s.e.m. of 1,128 instances of QD-IgE-FcεRI complexes approaching within 0.5 μm.

2.3.4 Dynamic actin structures restrict FcεRI diffusion

To determine the role of the actin cytoskeletal network in the lateral diffusion and observed co-confinement of QD-IgE-FcεRI complexes, RBL-2H3 cells were stably transfected with GFP-actin. Two-color time series of QD-IgE-FcεRI motion with respect to the actin cytoskeleton were acquired. Due to its superior signal-to-noise ratio, TIRF microscopy was primarily used to track QD-IgE-FcεRI and GFP-actin movements on the adherent cell surface at 33 frames/s.

In initial experiments, cells were treated with the protein kinase C agonist, phorbol myristate acetate (PMA), to induce actin filament bundles resembling stress fibers (Pfeiffer and Oliver 1994). QD-IgE-FcεRI diffusion was largely limited to actin-poor regions of the membrane, often remaining confined within a single actin-defined

compartment for several seconds of tracking (Fig. 2.4a,b and Appendix A, Video 2.3). The size of these compartments (L) can be estimated based upon the plateau value on the Y axis of the mean square displacement (*MSD*) plot. Figure 2.4a illustrates a typical MSD plot, generated from the receptor trajectory trace shown in Figure 2.4a (inset), and fit by MSD = *offset* + $(L^2/3)(1-\exp(-\Delta t / \tau))$ (Destainville and Salome 2006), where $D=L^2/12\tau$. From the fit we find that L = 1.1 μm, which correlates very well with the *actual, observed* actin-defined region in Figure 2.4a.

Imaging of untreated RBL-GFP-actin cells revealed continuous re-organization of the actin network, resulting in a nearly complete change in the pattern of GFP-actin fluorescence on a 10 s time scale (Appendix A, Video 2.4). Nevertheless, diffusion of QD-IgE-FcεRI still remained largely limited to actin-poor regions (Fig. 2.4c). Mathematical analysis of receptor/actin crossing frequency was performed to verify that receptors are avoiding actin structures. Comparing the real data trajectories with simulated, freely diffusing particles found a significant difference in actin/trajectory overlap, confirming that the real trajectories cannot be modelled by free diffusion unaffected by actin structures (Table 2.1 and Appendix A).

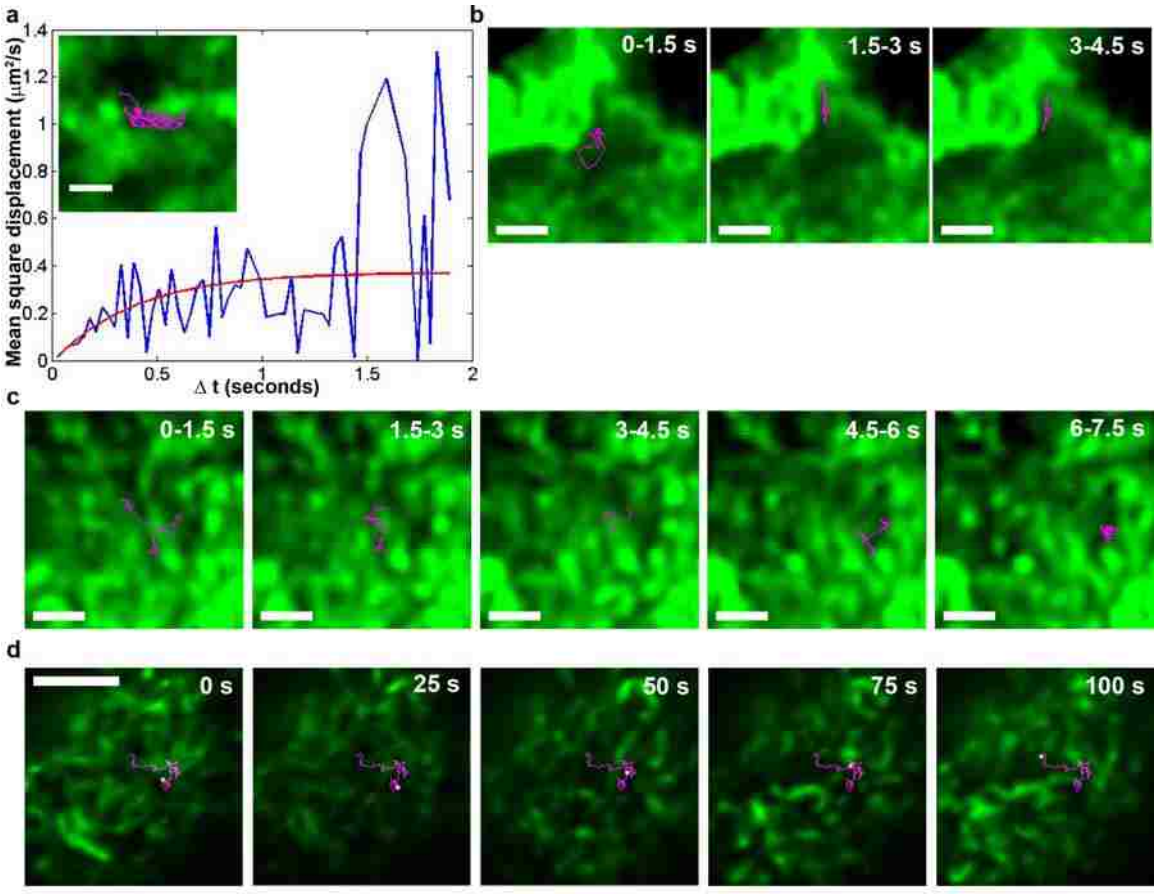

Figure 2.4 Actin defines regions of FcεRI motion in the membrane. (**a**) MSD plot of the trajectory shown in inset, demonstrating diffusion restricted to an area consistent with that delineated by the actin structures. (**a**, **inset**) QD-IgE-FcεRI trajectory (magenta) overlayed with the deconvolved GFP-actin image (green) from the adherent surface of a PMA-treated RBL-2H3 cell. (**b,c**) Image series of deconvolved GFP-actin (green) and 1.5 s long segments of a single QD655-IgE-FcεRI trajectory (magenta) on the adherent surface of a PMA treated (**b**) or untreated (**c**) RBL-2H3 cell. (**d**) Full 100 s QD-IgE-FcεRI trajectory (magenta) with position at 25 s intervals highlighted (white) overlayed with the deconvolved GFP-actin image (green) on the apical membrane of an RBL-2H3 cell. Panels **a-c** were acquired with TIRF microscopy at 33 frames/s. Panel **d** is from a 1 frame/s confocal time series with 1 μm slice thickness. The scale bars represent 1 μm in **a-c** and 5 μm in **d**.

The data in Figure 2.4a-c above were acquired from the relatively flat, adherent cell surface in TIRF mode, which images structures within ~200 nm of the coverslip. We performed multiple control experiments to ensure that interactions between the plasma membrane and the coverslip were not responsible for the observed behavior of QD-IgE-FcεRI complexes (Appendix A, Fig. S2.5). The observation of similar behavior on the

apical cell surface provides perhaps the most compelling support of the TIRF data for evidence of actin-restricted FcεRI diffusion. Confocal microscopy was used to eliminate the cytoplasmic GFP-actin signal and image the actin structure in a 1 μm slice at the apical cell surface. In confocal mode, the frame rate had to be reduced to 1 frame/s in order to image single QDs. Despite the slower frame rate, we were able to follow the trajectories of QD-labelled receptors over a period of 100 s while simultaneously imaging GFP-actin. Figure 2.4d shows that receptors on the apical surface were restricted from crossing actin-rich regions. As seen at the adherent cell surface, dynamic actin reorganization accompanies receptor movement into previously restricted areas (Fig. 2.4d and Appendix A, Video 2. 5).

To determine if FcεRI alters its diffusion properties when encountering actin structures or is simply deflected by the physical barrier, we calculated the mean square single jump length of FcεRI as a function of distance from actin (Fig. 2.5). Although the data analysis in Figure 5 suggests a slight reduction in mean jump distance as the receptor approaches the actin (solid line), simulations (dashed line) show that this can be explained by a combination of geometric effects and finite detector integration time (Ritchie, Shan et al. 2005). Thus, there is no indication of a real change in diffusion as close as 100 nm from underlying actin structures. These results favor the interpretation that membrane-associated actin structures or proteins bound to actin act on FcεRI as a physical barrier that deflects the receptor.

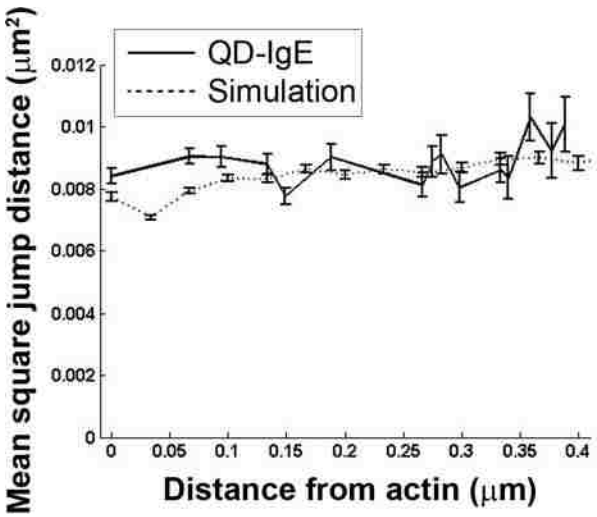

Figure 2.5 Effect of actin proximity on FcεRI trajectories. All QD-IgE trajectories found by TIRF-SPT at 33 frames/s in PMA-treated cells were used to calculate single time step mean square jump distances as a function of distance from an actin structure (solid line). For comparison, simulations of particles diffusing near a reflecting boundary with constant membrane viscosity and finite localization accuracy, modelled after the real data, were used to calculate mean square jump distances as function of distance from the reflecting boundary (dashed line).

To further discern the influence of the actin cytoskeleton on FcεRI diffusion, we treated cells with 500 nM latrunculin B for 10 minutes prior to imaging. This dose of latrunculin disrupts cytoskeletal architecture (see Appendix A, Fig. S2.6) without causing significant damage to cells (Frigeri and Apgar 1999). Latrunculin produced a small but significant ($p=1.9x10^{-5}$ by K-S test) increase in FcεRI diffusion on the apical membrane (Fig. 2.6a, Table 2.1), consistent with previous observations of less confined motion (Kusumi, Ike et al. 2005). Unexpectedly, latrunculin treatment decreased diffusion at the adherent surface (Table 2.1). While the mechanism is unclear, we note that non-actin components of the cortical cytoskeleton (possibly spectrin) are still visible in EM as a fine meshwork on the adherent surface of treated cells (see Appendix A, Fig. S2.7).

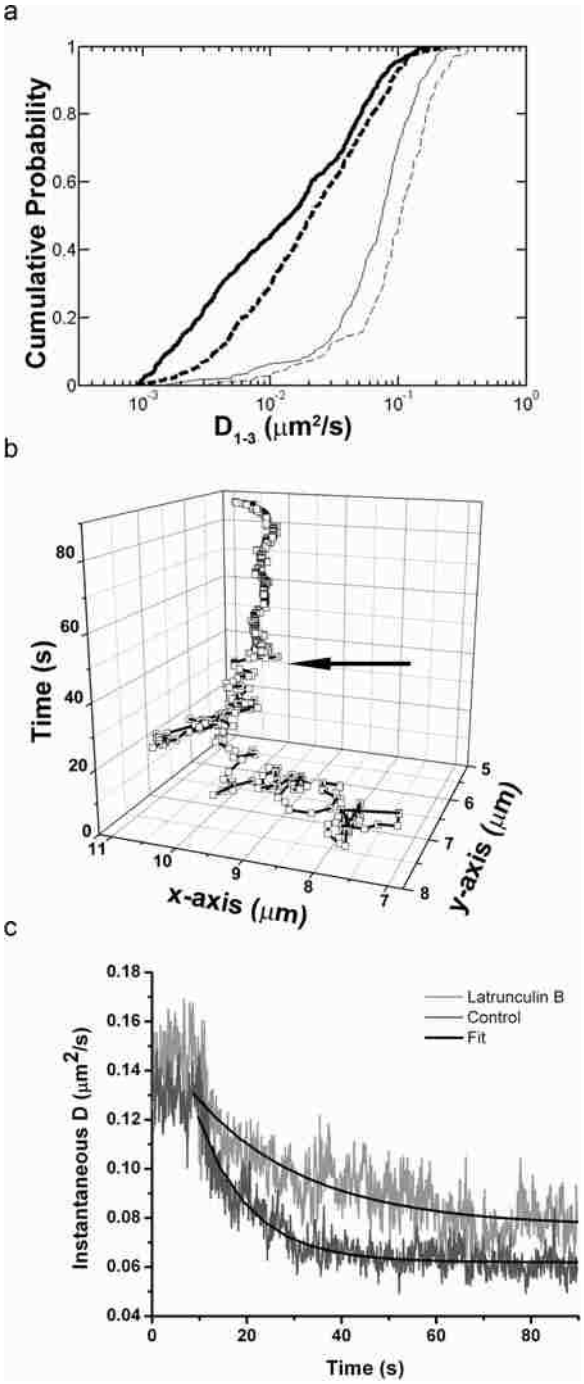

Figure 2.6 Actin facilitates cross-link-induced immobilization of FcεRI. (**a**) Cumulative probability distribution plot of diffusion coefficients for QD-IgE in the absence (solid lines) and presence (dashed lines) of latrunculin B and before (thin lines) and after (thick lines) cross-linking with DNP-BSA. (**b**) XY versus time plot of a single QD-IgE-FcεRI. Arrow indicates time of DNP-BSA addition. (**c**) Kinetics of cross-link-induced immobilization in the presence (light gray, n=12) and absence (dark gray, n=17) of latrunculin B. Black lines are fits to the exponential decay model: $D(t) = D_o e^{(-t/\tau)}$, where D is the instantaneous diffusion coefficient and τ is the decay constant.

2.3.5 Cytoskeletal disruption slows immobilization kinetics

Activation of RBL-2H3 cells is well-known to induce substantial cytoskeletal remodeling and an increase in F-actin content (Frigeri and Apgar 1999). There is also a dramatic decrease in FcεRI mobility within minutes of cross-linking (Menon, Holowka et al. 1986). To determine the kinetics of receptor immobilization, we devised an assay to measure the mobility of QD-IgE-FcεRI complexes during cross-linking with 30 ms time resolution.

Upon addition of 14 nM DNP-BSA, FcεRI diffusion is rapidly decreased. The mobility transition is evident in trajectories of individual receptors, as seen in Figure 6b. Averaging the behavior of many receptors over time yields the mean instantaneous diffusion coefficient plot (Fig. 2.6c). Note that diffusion reaches a baseline within seconds after cross-linking. An exponential decay model was used to fit the data after cross-linker addition, returning a characteristic decay time (τ) of 11.0 ± 0.19 s for untreated cells. In the presence of latrunculin, which disrupts both nanometer and micron-scale actin structures, τ increased to 30.0 ± 1.3 s (error indicates 95% confidence interval), suggesting a role for actin structure in the process of antigen-mediated receptor immobilization. From these data, we were also able to calculate median diffusion constants both prior to and immediately after cross-linking. Latrunculin treatment significantly ($p=1.8\times10^{-13}$ by K-S test) increases the final diffusion rate after cross-linker addition (Fig. 2.6a and Table 2.1), confirming that the actin cytoskeleton plays an important role in cross-link-induced immobilization of FcεRI.

2.4 DISCUSSION

Our results provide evidence for micron-scale restriction of membrane protein diffusion by *dynamic* actin structures and are particularly relevant to studies where membrane molecules are tracked on relatively long time scales (seconds). We frequently observed two or more QD-IgE-FcεRI complexes remaining in close proximity for several seconds (Fig. 2.2 and Appendix A, Video 2. 2). However, close inspection of this behavior revealed an absence of detectable correlated motion between individual receptors (Fig. 2.3). We suggest that this behavior represents co-confinement of multiple receptors within the same membrane domain and support the idea that the *micron-scale* domains of co-confinement are defined by barriers of filamentous actin. These shifting actin barriers sub-divide the membrane, producing transiently co-confined sub-populations of membrane proteins. Actin could restrict diffusion through various mechanisms, including acting as a physical barrier (actin itself or associated proteins), directly binding FcεRI, or interacting with lipids and increasing membrane viscosity. Our analysis of FcεRI diffusion with respect to actin bundles (Fig. 2.5) favors the physical barrier explanation.

In addition to the *micron-scale* actin-mediated restriction we have observed, we recognize that there is a finer level of membrane organization at work that we cannot directly visualize. This level of organization has been described as a meshwork composed not only of actin, but also a wide variety of cell-type specific intermediate filament proteins (eg., spectrin (Dahl, Geib et al. 1994; Tang and Edidin 2003)). This nano-scale organization likely underlies the small "confinement zones" apparent in higher frame rate SPT measurements (Saxton and Jacobson 1997; Murase, Fujiwara et al.

2004; Kusumi, Ike et al. 2005; Ritchie, Shan et al. 2005) and may play a role in forming the smaller clusters (~50 nm) of resting FcεRI observed in electron micrographs (Fig. 2.1d). We speculate that the finer cytoskeletal meshwork may be involved in producing a heterogeneous distribution of membrane components on a nanometer scale. The literature offers several representations of this heterogeneity, which exists within the boundaries of large-scale actin-defined regions described in this work, including the protein islands model (Douglass and Vale 2005; Lillemeier, Pfeiffer et al. 2006), the lipid raft model (Pike 2006; Viola and Gupta 2007) and the membrane skeleton model (Jacobson, Sheets et al. 1995; Kusumi, Nakada et al. 2005) (see Appendix A, Fig. S2.8).

The published models, while differing in their descriptions of the roles played by specific proteins in the cytoskeletal meshwork, are universally dependent upon an intact cortical cytoskeleton (Kusumi, Nakada et al. 2005; Lillemeier, Pfeiffer et al. 2006; Viola and Gupta 2007). Each of these putative membrane features are reported to be highly dynamic. In the membrane skeleton model, tracked membrane components reside in individual domains on millisecond time scales (Kusumi, Nakada et al. 2005). Lipid rafts are also reported to be very dynamic (Pike 2006; Viola and Gupta 2007). In our data, the lack of correlated motion at small separation distances (Fig. 2.3) implies that receptors only briefly remain in the same nanometer-scale domain. These data suggest that the small clusters of resting FcεRI observed by EM (Fig. 2.1d) are highly dynamic, with exchange between neighbouring small domains occurring on time scales much more rapid than the diffusion of the domains themselves.

The immobilization of IgE-FcεRI complexes in response to treatment with cross-linking agent has been previously studied by fluorescence recovery after photobleaching

(FRAP) (Schlessinger, Webb et al. 1976; Menon, Holowka et al. 1986; Mao, Varin-Blank et al. 1991; Pyenta, Schwille et al. 2003) and by SPT (Barisas, Smith et al. 2007). Unique features of our study include labeling and tracking at physiological temperatures and acquisition of real-time kinetics. A previous attempt to measure the time course of cross-linking-induced immobilization by FRAP was limited to events occurring at least 90 s after addition of cross-linking agent, at which time immobilization had already reached a maximum (Menon, Holowka et al. 1986). We employed our real-time assay to evaluate the kinetics of cross-linking from the precise moment of cross-linker addition. Our results demonstrate that diffusion of QD-IgE-FcεRI decreases within seconds of adding cross-linking agent (Fig. 2.6b) and that the rate of immobilization is slowed by actin disruption with latrunculin (Fig. 2.6a, Table 2.1). Combining our kinetic data with the SPT and EM results reveals that small, dynamic clusters of FcεRI transition to large, stable clusters by an actin-dependent mechanism within seconds of cross-linking. Disruption of actin by latrunculin also increased the apical diffusion coefficient of both resting and cross-linked receptors by two fold (Fig. 2.6a, Table 2.1). Interestingly, treatment with latrunculin is reported to prolong FcεRIγ phosphorylation and to increase degranulation (Frigeri and Apgar 1999), suggesting that the more mobile clusters may have an increased signaling lifetime. Our observation that cross-linked receptors are not as immobile in the presence of latrunculin suggests that immobilization is an important regulatory mechanism of FcεRI signaling.

Our direct and simultaneous observations of FcεRI motion and actin dynamics demonstrate that IgE receptors diffuse within micron-sized membrane domains defined by actin bundles and that confinement is dynamic over length scales of microns and time

scales of seconds. Restricted motion has been observed for a wide variety of membrane proteins, including the erbB family (Kusumi, Sako et al. 1993), glycine receptors (Dahan, Levi et al. 2003), and G-protein coupled receptors (Suzuki, Ritchie et al. 2005). The ubiquitous nature of restricted diffusion, coupled with the observations here, suggest that actin-mediated restriction of membrane protein diffusion plays an important regulatory role in a wide variety of signaling pathways.

2.5 MATERIALS AND METHODS

2.5.1 Reagents

Mouse monoclonal anti-DNP IgE was prepared as described(Liu, Bohn et al. 1980). Monovalent biotin-IgE was prepared through modification of the FluoReporter® Mini-Biotin-XX Protein Labeling Kit protocol (Invitrogen, Carlsbad, CA): a biotin-succinimidyl ester to IgE ratio of 4:1 and a 15 min reaction time was used to generate biotin-IgE with an average biotin:IgE ratio of 0.83:1 as determined with the FluoReporter® Biotin Quantitation Assay Kit (Invitrogen, Carlsbad, CA). Biotin-IgE was combined in 1:1 stoichiometry with Qdot® 655 or Qdot® 585 streptavidin conjugate (Invitrogen, Carlsbad, CA) in PBS + 1% BSA to generate 20-60 nM stock solutions of monovalent QD-IgE. Stock solutions were stored at 4°C and used within four weeks. To facilitate comparisons between unlabelled IgE and QD-IgE, all concentrations are reported in nM, with 5 nM IgE or 14 nM DNP-BSA being equivalent to 1 μg/ml. Latrunculin B was from Sigma-Aldrich (St. Louis, MO). PMA was from Invitrogen (Carlsbad, CA). DNP-BSA was from Molecular Probes (Eugene, OR).

2.5.2 Cell culture

Rat basophilic leukemia (RBL-2H3) cells were grown as adherent monolayers in minimum essential medium with 10% fetal calf serum (Invitrogen, Carlsbad, CA) as described (Wilson, Pfeiffer et al. 2000). For microscopy, cell monolayers were cultured in 8-well Lab-Tek chambers (Nunc, Rochester, NY) 24 hours before experiments.

2.5.3 Degranulation assay

Cell monolayers were grown in 24-well tissue culture plates for 24 hours. Typically, FcεRI were primed by adding 5 nM anti-DNP-IgE to cultures overnight. After washing away excess IgE, cells were activated with 0.014-140 nM DNP-BSA. Release of β-hexosaminidase was measured as described (Ortega, Schweitzer-Stenner et al. 1988).

2.5.4 Cell treatment for SPT experiments

Cells in Lab-Tek chambers were labelled with 50 or 100 pM QD-IgE in Hanks' balanced salt solution (HBSS) for 10 min at 37°C, then washed with HBSS prior to imaging. This yielded an average of ten QD-IgE-FcεRI complexes per cell. For TIRF imaging, washing was omitted. All imaging was performed at 34-36°C. PMA-treated samples were pre-incubated for 30 min and imaged in the presence of 50 nM PMA. Latrunculin B-treated samples were pre-incubated for 10 min and imaged in the presence of 500 nM latrunculin B. Where indicated, cells were stimulated with 14 nM DNP-BSA.

2.5.5 Cell treatment for immobilization

Cells were labelled with 500 pM QD-IgE for 10 min at 37°C as above, then incubated at 37°C for 30 min with 140 nM unlabelled IgE. Cells were washed and imaged by wide field microscopy at 35°C in 200 µl HBSS for ~10 seconds, followed by addition of DNP-BSA to a final concentration of 14 nM. Where described, cells were treated with 500 nM latrunculin B during the last 10 min of IgE priming and latrunculin B was maintained in the medium during activation. The presence of 500 nM latrunculin B did not affect the rate or amount of IgE binding (data not shown).

2.5.6 Electron Microscopy

RBL-2H3 cell monolayers on glass coverslips were labelled with 30 nM QD655-IgE for 30 min at 37°C. Cells were fixed for seven min in 0.5% PFA and membrane sheets prepared as described in (Wilson, Pfeiffer et al. 2000). Electron micrographs were acquired using a transmission electron microscope (Hitachi H600). Probe identification and Hopkins statistical analysis were performed as described in (Zhang, Leiderman et al. 2006).

2.5.7 Fluorescence Microscopy

Confocal imaging was performed on a Zeiss LSM 510 META system equipped with a 63× 1.4 N.A. oil objective. Single 1 μm z-sections were acquired at 1 frame/s. GFP and QDs were excited simultaneously using 488 nm excitation and emission collected using a 545 nm dichroic mirror with 505 nm LP filter and the 625-689 nm range of the META detector, respectively.

Wide field imaging for SPT was performed using an Olympus IX71 inverted microscope equipped with a 60× 1.3 N.A. water, 100× 1.4 N.A. oil, or 150× 1.45 N.A. oil TIRF objective. Wide field excitation was provided by a mercury lamp with either a 436 nm BP or 543 nm BP excitation filter. Objective-based total internal reflection fluorescence (TIRF) microscopy was performed using excitation from a 472 nm continuous wave laser (CrystaLaser, Reno NV), which was expanded and entered the microscope through a laser side port of the microscope filter turret. Fluorescence emission was filtered with a 473 nm long pass filter (LP01-473RU, Semrock, Rochester, NY). Emission was collected by an electron multiplying CCD camera (Andor iXon 887 for widefield; Andor Luca for TIRF). In both cases, an image splitter (Cairn Research

OptoSplit II, Kent, U.K.) was used to simultaneously image two spectrally distinct QDs or QD655 and GFP. Images were registered using a calibration image of multi–fluorophore fluorescent beads (0.2 μm Tetraspeck, Invitrogen, Carlsbad, CA) that have an emission spectrum covering the two spectral windows. For further details see Appendix A. QD emission was collected using the appropriate QD (20 nm bandpass) emission filters (Chroma, Rockingham, VT). GFP emission was collected using a 510/40 BP emission filter. The sample temperature (34-36 °C) was maintained by an objective heater (Bioscience Tools, San Diego, CA).

2.5.8 Single Particle Tracking

Images were acquired at either 33 or 100 fames/s for a total of 3,000 frames. Analysis of the acquired image series was performed as described previously (Arndt-Jovin, Lopez-Quintela et al. 2006) and similar to (Dahan, Levi et al. 2003) to obtain trajectories, which were used to generate mean square displacement (MSD) plots (Martin, Forstner et al. 2002) (see Supplementary Methods for more detail). Diffusion coefficients were found by fitting the first three points of the MSD plots to MSD = *offset* + $4D_{1\text{-}3}\Delta t$, (Kusumi, Sako et al. 1993). Localization accuracy for each individual trajectory is described by the offset from the origin of the resulting fit. Localization accuracy of the system was determined by imaging QD-IgE-FcεRI in cells treated with 14 nM DNP-BSA for 5 minutes, then fixed in 2% paraformaldehyde for 20 minutes at room temperature. Imaging under various experimental conditions yielded localization accuracies of 11.86 and 13.81 nm for QD655 and QD585, respectively imaged at 100 frames/s in TIRF mode; 9.32 and 10.37 nm for QD655 and QD585, respectively imaged at 33 frames/s in TIRF mode; and 50.00 nm for QD655 imaged on the apical surface at

33 frames/s in wide-field mode. Note that all interaction analysis was performed on data acquired under TIRF imaging conditions, where the localization is most accurate. Instantaneous diffusion coefficients are average diffusion coefficients calculated over all tracked QDs and using all points within a sliding window of 10 frames (.3 s). The instantaneous diffusion coefficient is given by

$D=(1/N)S_{t,t,n}((\boldsymbol{r}_{t+t}-\boldsymbol{r}_t)^2-offset)/4t$ where $\boldsymbol{r}$ is a trajectory position, *offset* is found by a fit to the longest trajectory, and the sum is over all N valid trajectory coordinate pairs in the time window.

2.5.9 Statistical Analysis

Due to the wide range of values and nonparametric distribution of D_{1-3}, values are reported as medians and interquartile range is provided as a measure of statistical dispersion. Statistical comparisons between data sets were made using the Kolmogorov-Smirnov test unless otherwise noted and significance was defined as $p<0.05$.

2.5.10 Image Processing

All image processing was performed using Matlab (The MathWorks, Inc., Natick, MA) in conjunction with the image processing library DIPImage (Delft University of Technology). For descriptions of specific analysis routines, see Appendix A.

2.6 ACKNOWLEDGEMENTS

This work was supported by NIH grants R01 GM49814, R01 AI051575 and P20 GM 67594, the Oxnard Foundation, ACS IRG 192, and by the Sandia LDRD and SURP

programs. Sandia is a multi-program laboratory operated by Sandia Corporation, a Lockheed Martin Company, for the United States Department of Energy under contract DE-AC04-94AL85000. Nicholas Andrews was supported by NSF IGERT DGE-0549500 and the UNM-SOM MD/PhD Program. We thank Sheli Ryan for cell culture assistance, Jun Zhang for EM image analysis, and Jonas Anderson and Bernd Rieger for image processing assistance. The UNM Cancer Center Fluorescence Microscopy Facility received support from NIH grants S10 RR14668, S10 RR19287, S10 RR016918, P20 RR11830 and P30 CA118100 and from NSF grant MCB9982161. Electron micrographs were generated in the University of New Mexico Electron Microscopy Facility, which received support from NIH grants P20 GM067594, S10 RRI5734 and RR022493.

CHAPTER 3: ANTIGEN-INDUCED FcεRI IMMOBILIZATION IS REQUIRED FOR INTERNALIZATION, NOT SIGNALING

Antigen-induced FcεRI immobilization is required for internalization, not signaling

Nicholas L. Andrews[1], Janet R. Pfeiffer[1], A. Marina Martinez[1], David M. Haaland[2], Ryan W. Davis[2], Bridget S. Wilson[1], Janet M. Oliver[1], and Diane S. Lidke[1]

[1]Department of Pathology and Cancer Research and Treatment Center, University of New Mexico, Albuquerque, New Mexico 87131

[2]Sandia National Laboratories, Albuquerque, New Mexico 87185-0351

Prepared for Submission to *Immunity*

Correspondence should be addressed to D.S.L. (e-mail: dlidke@salud.unm.edu)

Abbreviations: BSA, bovine serum albumin; DNP, 2,4-dinitrophenol; EM, electron microscopy; FcεRI, high affinity IgE receptor; FRAP, fluorescence recovery after photobleaching; MSD, mean square displacement; QD, quantum dot; SPT, single particle tracking

3.1 ABSTRACT

The high affinity IgE receptor (FcεRI) plays a central role in the allergic inflammatory response. Cross-linking of IgE-bound FcεRI by multivalent antigen stimulates the release of pre-formed mediators of allergic inflammation from mast cell granules. At high concentrations, multivalent antigen-binding has been shown to cause a rapid decrease in the lateral mobility of FcεRI and subsequent internalization of the receptor. In this study, we use quantum dot (QD) based probes, single molecule tracking, and hyperspectral microscopy to address the causal relationship between antigen-induced FcεRI immobilization, signal initiation, and internalization. We demonstrate that the kinetics and extent of immobilization are highly dependent on antigen concentration and are directly related to the size of IgE-FcεRI clusters formed. The Src-family kinase inhibitor PP2, which inhibits the earliest steps in FcεRI signaling, does not significantly affect antigen-induced immobilization, aggregation, or internalization of FcεRI. By employing two different specificities of IgE, we show that each specificity forms clusters independently and that cross-linking one subset of receptors does not alter the diffusion or distribution of non-cross-linked receptors. Using hyperspectral microscopy, we demonstrate that small, antigen-induced clusters of at least three IgE-FcεRI remain freely mobile on the cell surface under conditions in which activation is occurring. We also demonstrate that multivalent antigen itself, in the form of DNP-QD, remains mobile on the cell surface at activating doses. Our results demonstrate that antigen-induced immobilization is due solely to formation of large receptor clusters and is required for FcεRI internalization; not signaling.

3.2 INTRODUCTION

The T-cell receptor (TCR), B-cell receptor (BCR), and high affinity IgE receptor (FcεRI) constitute the multichain immune recognition receptor family and are crucial to the execution of key events in the immune response (Sigalov 2004). These receptors share a common mechanism of activation in which multiple receptors must be cross-linked together by a multivalent antigen in order to initiate signal transduction (Boniface, Rabinowitz et al. 1998; Thyagarajan, Arunkumar et al. 2003; Kraft and Kinet 2007). In each of these systems, antigen binding is associated with changes in receptor dynamics and topography (Dustin and Cooper 2000; Wilson, Pfeiffer et al. 2000; Thyagarajan, Arunkumar et al. 2003). In the case of the TCR, it has recently been shown that TCR microclusters signal actively while diffusing through the peripheral supramolecular activation complex (pSMAC), and cease signaling in the central supramolecular activation complex (cSMAC) where they are largely immobile (Varma, Campi et al. 2006). In the FcεRI system, it is well established that IgE-FcεRI mobility decreases dramatically upon addition of high doses of multivalent antigen (>1 μg/ml) (Menon, Holowka et al. 1986; Zidovetzki, Bartholdi et al. 1986; Pecht, Ortega et al. 1991; Larson, Gosse et al. 2005; Andrews, Lidke et al. 2008). These studies demonstrate that changes in receptor diffusion in response to activation is a common feature of multichain immune recognition receptor family members. However, the relationship between these changes and signaling remains to be elucidated.

In contrast to the clear changes in diffusion of FcεRI in response to high doses of multivalent antigen, the effects of lower antigen doses on receptor mobility are less well-studied. One early study used Fluorescence Recovery After Photobleaching (FRAP) to

demonstrate that cross-linking of FITC-IgE-labeled FcεRI by low levels of anti-FITC antibodies induced degranulation without causing significant decreases in FcεRI mobility (Schlessinger, Webb et al. 1976). Subsequent studies using FRAP (Menon, Holowka et al. 1986; Mao, Varin-Blank et al. 1991; Pyenta, Schwille et al. 2003) and rotational correlation spectroscopy (Pecht, Ortega et al. 1991) concluded that the extent of IgE-FcεRI immobilization is correlated with the extent of degranulation, leading to speculation that immobilization of IgE-FcεRI may drive signaling.

To examine the relationship between antigen-induced changes in FcεRI mobility and signaling, we generated monovalent quantum dot (QD)-IgE that binds FcεRI without cross-linking (Andrews, Lidke et al. 2008) and also multivalent 2,6-dinitrophenyl-QD (DNP-QD), which serves as a multivalent antigen. We have previously described the development of a real-time assay for following the kinetics of cross-link induced FcεRI immobilization (Andrews, Lidke et al. 2008). Using this assay, we showed that immobilization occurs within seconds of antigen addition (at 1 μg/ml of DNP-BSA) and that the kinetics of this response are delayed nearly three-fold by cytoskeletal disruption with latrunculin B (Andrews, Lidke et al. 2008). In the present study, we use the real-time fluorescence assay to demonstrate that antigen-induced immobilization of FcεRI is dose-dependent and electron microscopy to show that the extent of immobilization correlates with the size of FcεRI clusters formed. We also show that inhibition of downstream signaling by the Src-family kinase inhibitor PP2 does not appreciably affect antigen-induced immobilization or FcεRI internalization and that direct cross-linking of IgE-FcεRI complexes by multivalent antigen is required for the immobilization to occur. Using hyperspectral imaging microscopy, we provide evidence that antigen cross-linked

clusters of FcεRI remain mobile, even at doses sufficient to trigger degranulation. Finally, we demonstrate that receptor-bound multivalent antigen itself also remains mobile at doses that trigger degranulation. We conclude that signaling requires FcεRI crosslinking but not FcεRI immobilization.

3.3 RESULTS

3.3.1 Dose dependence of immobilization and cluster size

The dramatic reduction in IgE-FcεRI mobility that accompanies cross-linking at high doses of multivalent antigen has been well documented (Schlessinger, Webb et al. 1976; Menon, Holowka et al. 1986; Zidovetzki, Bartholdi et al. 1986; Mao, Varin-Blank et al. 1991; Pecht, Ortega et al. 1991; Andrews, Lidke et al. 2008). We investigated the dose-dependence of this immobilization in order to understand its relationship to FcεRI signaling. RBL-2H3 cells were labeled with a mixture of QD625- and QD705-$IgE_{anti\text{-}DNP}$ and then the remaining FcεRI sites were saturated with dark (unlabeled) $IgE_{anti\text{-}DNP}$. Single QD tracking was initiated at 20 frames/s and cells were stimulated by the addition of varying doses of the multivalent antigen, DNP-BSA, ten seconds into each image series. From the resulting time-series images, we calculated the mean instantaneous diffusion coefficient (see 3.7 Materials and Methods), which provides a high temporal resolution measure of the average diffusion rate of IgE-FcεRI. We then plotted this value as a function of time and antigen dose (Figure 3.1A). These data clearly demonstrate that the rate and extent of QD-IgE-FcεRI immobilization is highly dependent on the dose of multivalent antigen. We noted that 0.001 μg/ml DNP-BSA produced only a slight decrease in QD-IgE-FcεRI mobility (Figure 3.1A; magenta line) while still eliciting

robust degranulation (Figure 3.1B), contrary to previous reports suggesting a link between extent of immobilization and amount of degranulation (Menon, Holowka et al. 1986; Mao, Varin-Blank et al. 1991; Pecht, Ortega et al. 1991; Pyenta, Schwille et al. 2003). However, since degranulation is measured as total ß-hexosaminidase release over a 30 minute period of antigen exposure, it was possible that QD-IgE-FcεRI were in fact immobilizing at some later time point. To examine this possibility, we followed the mean instantaneous diffusion coefficient in response to cross-linking with 0.001 µg/ml DNP-BSA out to 15 minutes and noted no decrease in diffusion (Appendix B, Supplementary Figure S3.1). To further assess the relationship between signaling onset and receptor immobilization, we simultaneously measured the kinetics of immobilization and calcium response of individual cells (Appendix B, Supplementary Methods) and showed that intracellular calcium signaling occurs while QD-IgE-FcεRI remains mobile (Appendix B, Supplementary Figure S3.2).

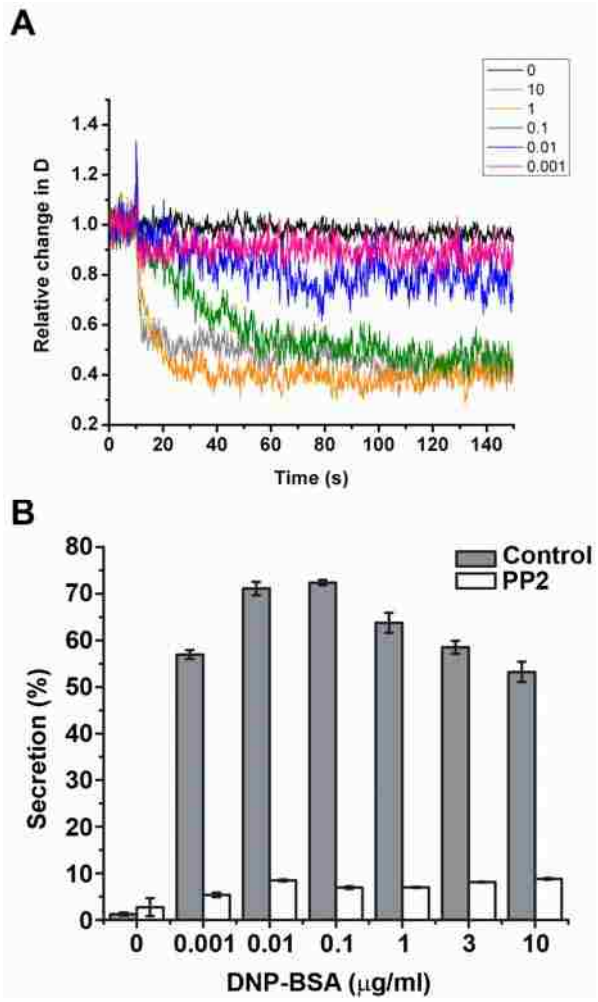

Figure 3.1 Antigen induced immobilization and degranulation are dose-dependent. (A) The relative change in diffusion rate as a function of time. Cells were treated with DNP-BSA at the indicated doses (in μg/ml) 10 s into each image series. (B) Degranulation assay plot showing percentage of total β-hexosaminidase released from cells stimulated with the indicated doses of DNP-BSA in the presence (white bars) and absence (gray bars) of PP2. Error bars represent standard deviation.

A previous study using scanning electron microscopy demonstrated a relationship between IgE-FcεRI aggregate size and extent of ß-hexosaminidase release. This study reported that formation of small oligomers (chains and small clusters) by anti-IgE antibodies was associated with robust degranulation, whereas the formation of large aggregates at higher doses of anti-IgE was associated with a diminished secretory response (Seagrave, Pfeiffer et al. 1991). Here, we used transmission electron

microscopy (TEM) of membrane sheets to obtain information on the dose-dependence of IgE-FcεRI cluster formation for comparison with the kinetics of IgE-FcεRI immobilization. After one minute of stimulation, significant dose-dependent differences in IgE-FcεRI cluster size were clearly visible (Figure 3.2A-C). Quantification of these images confirmed that larger clusters of IgE-FcεRI are formed at higher antigen doses (Figure 3.2D) where the secretory response is diminished (Figure 3.1B). Given that aggregate size is reported to be a major determinant of diffusion rate (Peters and Cherry 1982; Kusumi, Nakada et al. 2005), these data suggest that cross-linking receptors into large complexes could be the sole driving force behind antigen-induced immobilization.

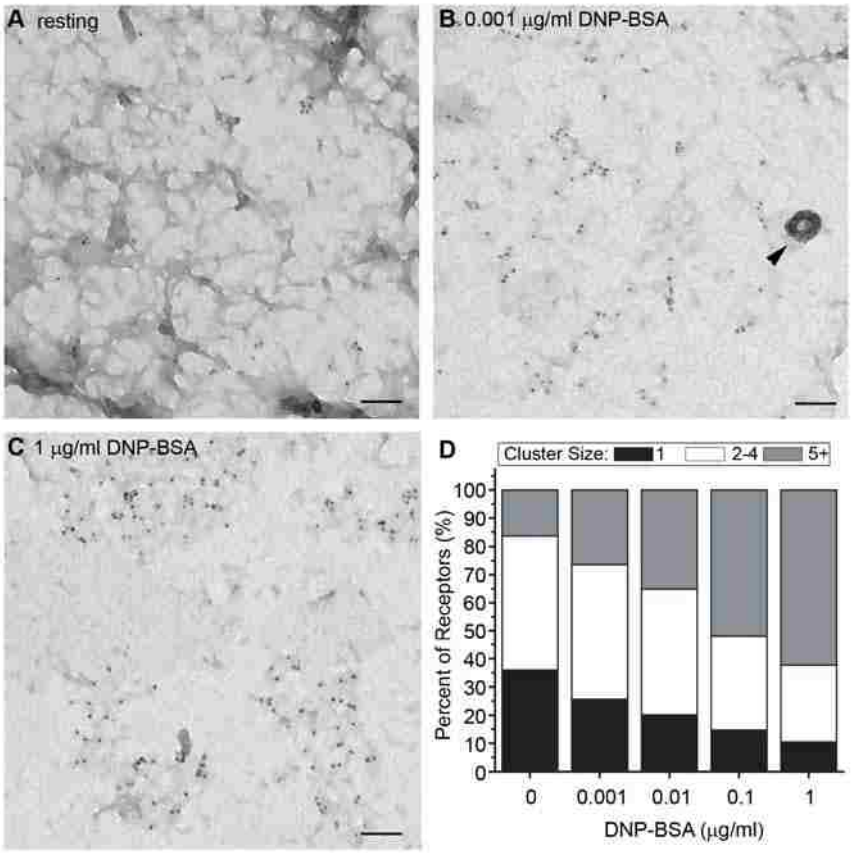

Figure 3.2 Clustering of IgE-FcεRI is dose-dependent. (A-C) Electron micrographs from membrane sheets with 5 nm gold particles marking the position of the β-subunit of FcεRI. Membrane sheet preparations were from resting cells (A), or cells treated with 0.001 (B) or 1 (C) µg/ml DNP-BSA for 1 min. (D) Quantification of receptor clustering after 1 min of stimulation at the indicated doses of DNP-BSA, based upon 10 micrographs per condition. Arrowhead in B indicates a clathrin coated pit. Scale bars in A-C represent 0.1 µm.

3.3.2 Role of downstream signaling

To assess the relationship between signaling and immobilization, we performed anti-phosphotyrosine western blotting over a range of DNP-BSA doses. These experiments demonstrated that the kinetics of tyrosine phosphorylation of the 72 kD band (Syk) in RBL-2H3 lysates were highly dose dependent (Figure 3.3A and B). Tyrosine phosphorylation of Syk occurred with slower kinetics at the lowest antigen dose (0.001 µg/ml), whereas the highest antigen dose (10 µg/ml) showed rapid but attenuated

phosphorylation. We used the Src-family kinase inhibitor PP2 to examine the causal relationship between downstream signaling and the antigen-induced immobilization and internalization of FcεRI. At the dose employed (10 μM), PP2 dramatically reduced antigen-induced tyrosine phosphorylation in response to crosslinking with 1 μg/ml DNP-BSA (Figure 3.3C, D) and largely inhibited degranulation across a range of DNP-BSA concentrations (Figure 1.1B). We employed a flow-cytometry based assay to measure internalization of IgE-FcεRI in response to treatment with various concentrations of DNP-BSA in the presence or absence of PP2 (see 3.7 Materials and Methods). Our results indicate that PP2 treatment did not appreciably affect antigen-induced FcεRI internalization (Figure 3.3E). We also used our kinetics of immobilization assay to examine the effects of PP2 on antigen-induced immobilization of IgE-FcεRI. As can be seen in Figure 3.3F, treatment of cells with 1 μg/ml DNP-BSA resulted in a dramatic immobilization of IgE-FcεRI, irrespective of the presence of PP2. We also observed that antigen-induced clustering of IgE-FcεRI still occurred in the presence of PP2 (Appendix B, Supplementary Figure S3.3). These data indicate that both antigen-induced immobilization and internalization are independent of PP2-sensitive downstream signaling.

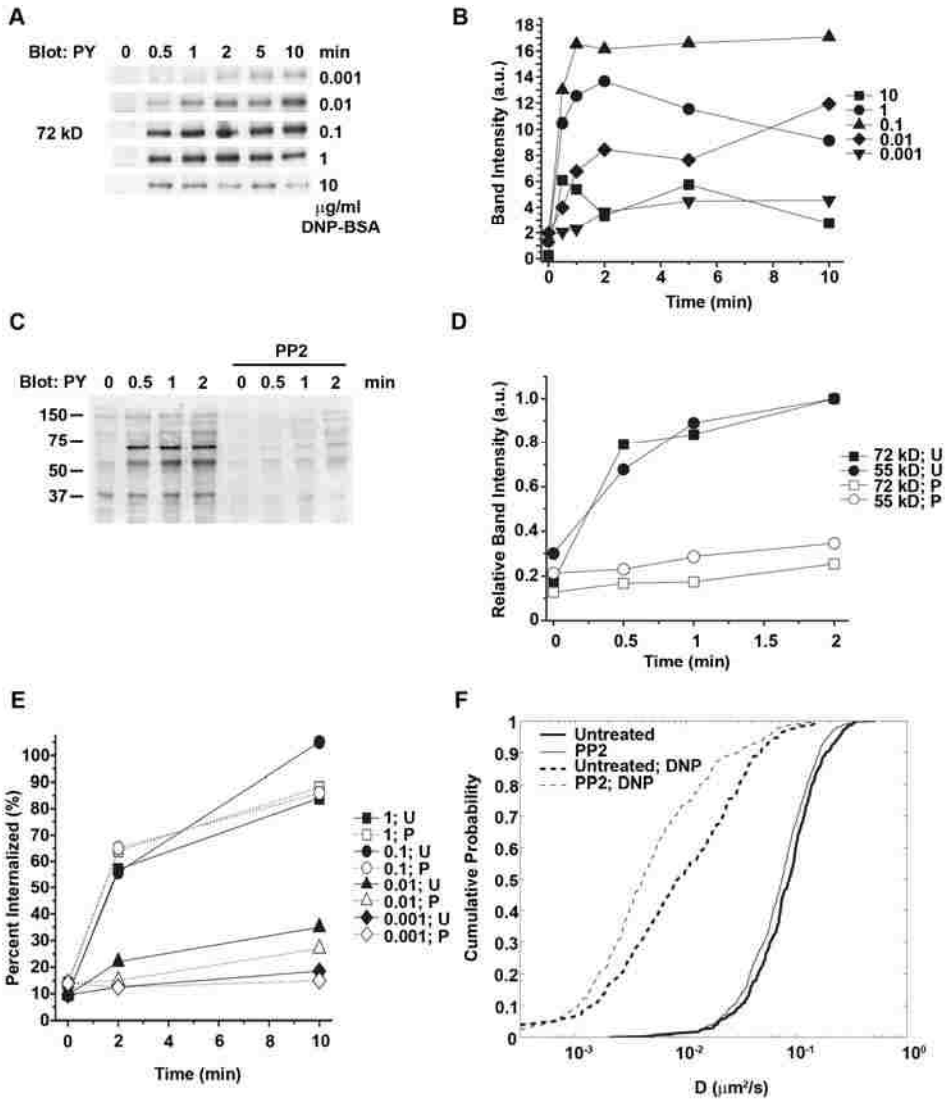

Figure 3.3 PP2-sensitive signaling is not required for immobilization or internalization. (A) Western blot showing the phosphotyrosine signal from the 72 kD band (Syk) in RBL-2H3 cells stimulated with the indicated doses of DNP-BSA. (B) Quantification of blot shown in A. (C) Western blot showing phosphotyrosine signal from RBL-2H3 cells stimulated with 0.1 µg/ml DNP-BSA in the presence or absence of PP2. (D) Quantification of the 72 kD (Syk) and 55 kD (Lyn) bands from the blot shown in C. Intensity is normalized to the peak signal for each band. (E) Percent internalization of IgE-FcεRI as a function of time and antigen dose in the presence (open symbols) or absence (filled symbols) of PP2. (F) CPA plot showing diffusion of QD-IgE-FcεRI before (solid lines) or 1 min after (dashed lines) addition of 1 µg/ml DNP-BSA in the presence (thin lines) or absence (thick lines) of PP2. In D and E, U=untreated; P= PP2. All antigen doses are in µg/ml.

3.3.3 Direct cross-linking of IgE-FcεRI is required for immobilization

To date, the majority of studies have employed cells labeled with only a single specificity of IgE. While this facilitates experimentation, it does not reflect the physiological reality in which less than 10% of receptors on any single cell are likely to be specific for the same allergen (Johansson, Oman et al. 2006). The ability of cells to respond when only a small number of IgE-FcεRI bind antigen has been demonstrated in an earlier study which estimated that only 5% of total surface FcεRI needs to be cross-linked to yield a secretory response (Ortega, Schweitzer-Stenner et al. 1988). These observations raise the possibility that antigen-bound receptors may be able to activate nearby, non-cross-linked receptors, amplifying the signal. A similar model has been proposed for the epidermal growth factor receptor (Verveer, Wouters et al. 2000), and a related phenomenon has been observed in TCR signaling, in which CD4 mediates formation of a "pseudodimer" between two TCRs, enabling T-cells to respond to a single peptide-MHC complex (Irvine, Purbhoo et al. 2002). To determine if such a phenomenon plays a role in antigen-induced clustering and immobilization of FcεRI, we employed IgE of two different specificities: one idiotype recognizes DNP ($IgE_{anti\text{-}DNP}$) and the other recognizes dansyl ($IgE_{anti\text{-}dansyl}$). We first confirmed the specificity of each antibody by priming cells with either $IgE_{anti\text{-}dansyl}$ or $IgE_{anti\text{-}DNP}$ and then stimulating with either dansyl-BSA or DNP-BSA. As expected, cells loaded with $IgE_{anti\text{-}dansyl}$ and stimulated with dansyl-BSA produced a comparable secretory response to cells loaded with $IgE_{anti\text{-}DNP}$ and stimulated with DNP-BSA (Appendix B, Supplementary Figure S3.3). We also observed that $IgE_{anti\text{-}dansyl}$ primed cells did not respond to DNP-BSA and

$IgE_{anti\text{-}DNP}$ primed cells did not respond to dansyl-BSA (Appendix B, Supplementary Figure S3.4) over a range of antigen doses.

We next examined whether the two different IgE specificities co-clustered upon stimulation with one or both antigens. We primed cells with a 1:1 mixture of Alexa488-$IgE_{anti\text{-}DNP}$ and Alexa633-$IgE_{anti\text{-}dansyl}$. These cells were then exposed to 0.1 μg/ml DNP-BSA, dansyl-BSA, or both (0.05 μg/ml each) for 1 min, then fixed and imaged by confocal microscopy. As can be seen in Figure 3.4A, each IgE specificity only forms clusters in the presence of its cognate antigen, as had been previously suggested (Boniface, Rabinowitz et al. 1998), and these clusters form independently when both antigens are applied simultaneously. This suggests that the clustering of IgE-FcεRI is due to the direct effects of cross-linking by multivalent antigen, and is not due to a global cellular response which induces cluster formation.

To determine the requirement for direct binding to antigen in antigen-induced immobilization of IgE-FcεRI, we developed an SPT-based assay. Cells were labeled with SPT levels of QD655-$IgE_{anti\text{-}DNP}$ and then the remaining receptor sites were saturated with either $IgE_{anti\text{-}DNP}$ or $IgE_{anti\text{-}dansyl}$. As shown in Figure 3.4B, cross-linking the $IgE_{anti\text{-}dansyl}$ primed receptors with 1 μg/ml dansyl-BSA did not significantly affect the diffusion of QD655-$IgE_{anti\text{-}DNP}$ primed receptors. Conversely, cross-linking the $IgE_{anti\text{-}DNP}$ primed receptors with 1 μg/ml DNP-BSA produced the expected dramatic decrease in QD-$IgE_{anti\text{-}DNP}$ primed receptors.

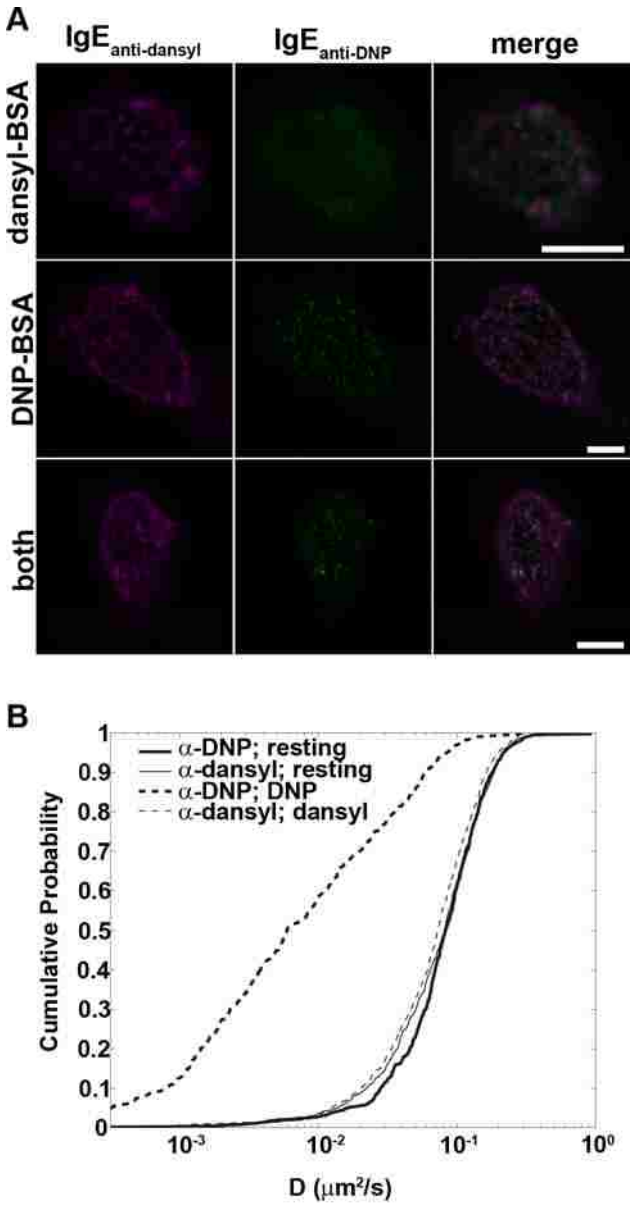

Figure 3.4 Direct cross-linking is required for immobilization. (A) Cells were primed with Alexa647-$IgE_{anti\text{-}dansyl}$ and Alexa488-$IgE_{anti\text{-}DNP}$ and then stimulated for 1 min with DNP-BSA, dansyl-BSA, or both. Scale bars represent 5 μm. (B) The cumulative probability plot of the diffusion rate of QD-$IgE_{anti\text{-}DNP}$ for four conditions is shown. Cells were labeled with QD-$IgE_{anti\text{-}DNP}$ and then primed with either $IgE_{anti\text{-}DNP}$ or $IgE_{anti\text{-}dansyl}$. The diffusion rate of QD-$IgE_{anti\text{-}DNP}$ was then measured in $IgE_{anti\text{-}DNP}$ primed cells before (thick, solid line) and after (thick, dashed line) addition of 1 μg/ml DNP-BSA. The diffusion rate of QD-$IgE_{anti\text{-}DNP}$ was also measured in $IgE_{anti\text{-}dansyl}$ primed cells before (thin, solid line) and after (thin, dashed line) addition of 1 μg/ml dansyl-BSA.

We also modified the above experiment in order to visualize the relationship between antigen-induced clusters and non-cross-linked FcεRI. We labeled cells with SPT levels of QD655-$IgE_{anti\text{-}DNP}$ and then saturated the remaining receptor sites with Alexa488-$IgE_{anti\text{-}dansyl}$. We then stimulated cells with 1 μg/ml dansyl-BSA and simultaneously imaged clustering of Alexa488-$IgE_{anti\text{-}dansyl}$ and diffusion of QD655-$IgE_{anti\text{-}DNP}$. We did not observe prolonged interactions of QD655-$IgE_{anti\text{-}DNP}$ with the clusters of Alexa488-$IgE_{anti\text{-}dansyl}$ (Appendix B, Video 3.1). These experiments together demonstrate the requirement for direct cross-linking in antigen-induced clustering and immobilization of IgE-FcεRI and do not support the existence of lateral signal propagation from antigen-bound to unbound receptors.

3.3.4 Antigen-induced clusters of at least three receptors do not immobilize

It has been previously reported that cross-linking of FcεRI to aggregates larger than dimers induces immobilization (Menon, Holowka et al. 1986). As this did not appear to be consistent with our observations, we designed an experiment to directly observe the motion of small antigen-induced clusters of FcεRI. Cells were labeled with a mixture of five colors of QD-IgE (QD525-, QD565-, QD585-, QD625-, and QD655-IgE) and imaged used a custom-built confocal, hyperspectral microscope (Sinclair, Haaland et al. 2006). This instrument collects emitted light from 490 to 800 nm (512 wavelengths) at each pixel in the image, enabling the entire spectrum of each emitting species in a given sample to be collected. Coupled with powerful multivariate curve resolution (MCR) algorithms, we have previously used this system to identify individual QDs even within a single QD "class" (e.g. Qdot® 565) based on their characteristic emission spectra (Lidke, Andrews et al. 2007). This instrumentation enabled us to acquire

confocal images at a rate of one frame every four seconds while simultaneously visualizing all five colors of QD-tagged IgE-FcεRI complexes. Since we could load cells with a five-fold higher concentration of IgE than could be used in single-color imaging, enough receptors could be primed with QD-IgE to produce a secretory response when cells were challenged with multivalent antigen, without having to prime additional receptors with unlabeled IgE (Appendix B, Supplementary Figure S3.5). Based upon our prior work, we expected to observe some instances of transient co-confinement of multiple IgE-FcεRI (Andrews, Lidke et al. 2008). Consistent with our expectations, we never observed two or more colors of QD diffusing together for more than four seconds (i.e., no two QDs were together over two consecutive frames) in the absence of multivalent antigen. However, upon addition of 0.1 μg/ml DNP-BSA, we frequently observed prolonged (>10 s) co-diffusion of multiple QD-IgE-FcεRI. By obtaining the spectrum from a cluster of QD-IgE-FcεRI, we could easily determine the number of distinct spectral peaks, which correspond to the minimum number of QD-IgE-FcεRI within the cluster. Given that the peak positions within the spectrum obtained from a single cluster were quite stable over time, we were able to demonstrate that at least three QD-IgE-FcεRI diffused as a stable aggregate over many seconds. Two examples of this behavior are shown in Figure 3.5, in which three spectrally distinct QD-IgE-FcεRI diffuse together for over two minutes. We confirmed that activation was in fact occurring under these conditions by degranulation assay (Appendix B, Supplementary Figure S3.5).

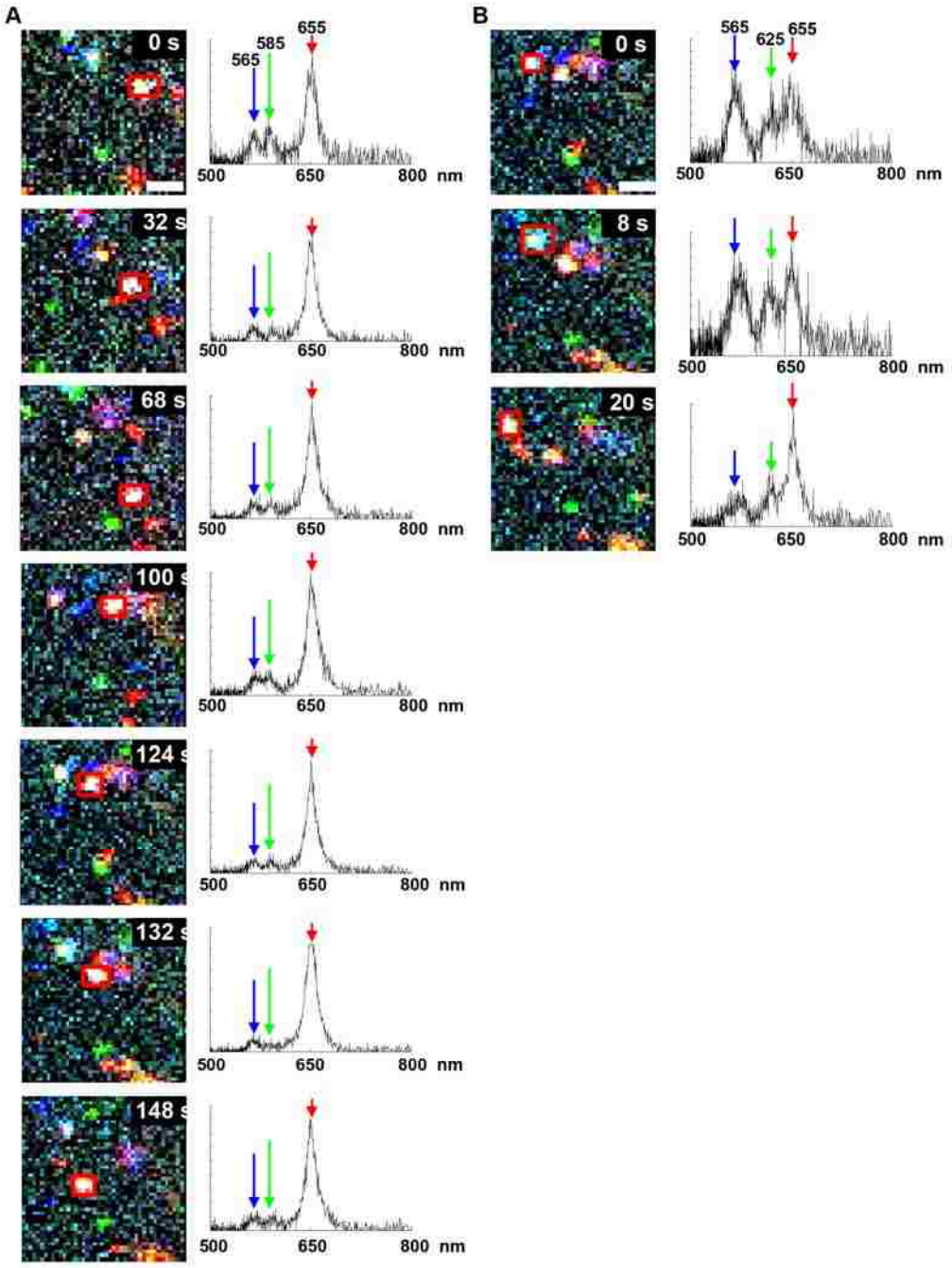

Figure 3.5 Antigen-induced clusters of at least three QD-IgE-FcεRI remain mobile. Cells were labeled with five colors of QD-IgE and then stimulated with 0.1 μg/ml DNP-BSA. Selected images showing diffusing QD-IgE-FcεRI clusters and the spectra of selected clusters (red rectangles) to the right of each image. (A) A cluster composed of QD565-, QD585-, and QD655-IgE-FcεRI diffusing together for over two minutes. (B) A cluster composed of QD565-, QD625-, and QD655-IgE-FcεRI diffusing together for 20 s. Variation in the peak intensities over time is attributed to QD "blinking." Pseudo-colored RGB images generated by displaying 635-655 nm as red, 575-630 nm as green, and 540-570 nm as blue. Scale bars represent 2 μm.

3.3.5 Multivalent antigen remains highly mobile at low, activating doses

Finally, we sought to examine the diffusion of multivalent antigen upon binding to IgE-FcεRI. We generated a QD-based multivalent antigen by reacting biotin-DNP with Qdot® streptavidin conjugates to produce multivalent DNP-QD. We first tested the ability of this antigen to trigger degranulation and found a robust secretory response that was essentially identical for DNP-QD655 and DNP-QD585 (Figure 3.6A). We then primed cells with $IgE_{anti\text{-}DNP}$ and labeled them with a sub-activating dose (1 pM) of DNP-QD655. Using single QD tracking, we determined the diffusion coefficient of DNP-QD655 to be slightly slower than that of unstimulated QD655-IgE (Table 3.1), consistent with formation of small oligomers of IgE-FcεRI upon DNP-QD binding. We next added an activating dose of DNP-QD585 (500 pM) and noted only a slight decrease in the diffusion of DNP-QD655 (Figure 3.6B). These data indicate that, at doses capable of elciting degranulation, multivalent antigen remains mobile upon binding to IgE-FcεRI, consistent with the formation of small, mobile clusters.

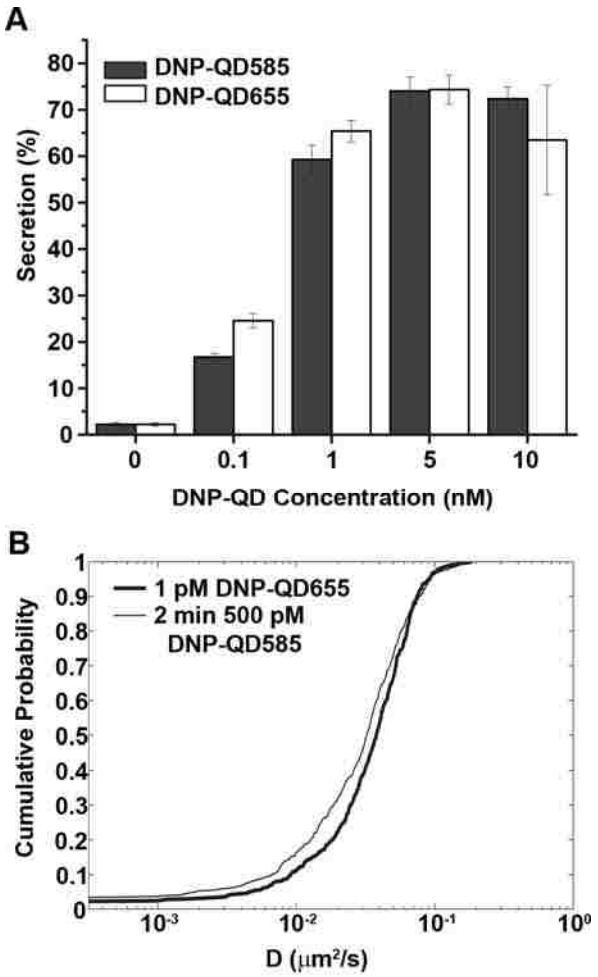

Figure 3.6 DNP-QD remains mobile at activating doses. (A) Degranulation assay plot showing percentage of total β-hexosaminidase released from cells stimulated with the indicated doses of DNP-QD655 (white bars) or DNP-QD585 (gray bars). Error bars represent standard deviation. (B) Cells were primed with $IgE_{anti\text{-}DNP}$ and then labeled with 1 pM DNP-QD655. The cumulative probability of the diffusion rate of DNP-QD655 was then calculated before (thick line) and two min after (thin line) addition of 500 pM DNP-QD585.

Table 3.1. Median diffusion coefficients

Probe	Priming	PP2	Stimulus	Rate[a] (Hz)	D_{1-3}[b] ($\mu m^2/s$)	IQR[c]	N
QD-$IgE_{anti-DNP}$	$IgE_{anti-DNP}$	-	None	20	0.0986	0.0862	6437
QD-$IgE_{anti-DNP}$	$IgE_{anti-DNP}$	-	0.001 μg/ml DNP-BSA	20	0.0662	0.0801	892
QD-$IgE_{anti-DNP}$	$IgE_{anti-DNP}$	-	0.01 μg/ml DNP-BSA	20	0.0519	0.0777	523
QD-$IgE_{anti-DNP}$	$IgE_{anti-DNP}$	-	0.1 μg/ml DNP-BSA	20	0.0119	0.0461	534
QD-$IgE_{anti-DNP}$	$IgE_{anti-DNP}$	-	1 μg/ml DNP-BSA	20	0.003	0.0320	421
QD-$IgE_{anti-DNP}$	$IgE_{anti-DNP}$	-	10 μg/ml DNP-BSA	20	0.0069	0.0362	567
QD-$IgE_{anti-DNP}$	$IgE_{anti-DNP}$	-	None	33	0.0855	0.0747	424
QD-$IgE_{anti-DNP}$	$IgE_{anti-DNP}$	+	None	33	0.0740	0.0701	667
QD-$IgE_{anti-DNP}$	$IgE_{anti-DNP}$	-	1 μg/ml DNP-BSA	33	0.0083	0.0210	310
QD-$IgE_{anti-DNP}$	$IgE_{anti-DNP}$	+	1μg/ml DNP-BSA	33	0.0041	0.0089	309
QD-$IgE_{anti-DNP}$	$IgE_{anti-DNP}$	-	None	33	0.0823	0.0757	763
QD-$IgE_{anti-DNP}$	$IgE_{anti-dansyl}$	-	None	33	0.0807	0.0872	687
QD-$IgE_{anti-DNP}$	$IgE_{anti-DNP}$	-	1μg/ml DNP-BSA	33	0.0059	0.0236	497
QD-$IgE_{anti-DNP}$	$IgE_{anti-dansyl}$	-	1μg/ml dansyl-BSA	33	0.0727	0.0771	842
DNP-QD	$IgE_{anti-DNP}$	-	1 pM DNP-QD655	33	0.0377	0.0360	505
DNP-QD	$IgE_{anti-DNP}$	-	1 pM DNP-QD655 + 500 pM DNP-QD585	33	0.0321	0.0366	576

[a]Rate is the frame rate at which the data was acquired.

[b]D_{1-3} is the diffusion coefficient as calculated by fitting to the first three points of the mean square displacement plot. The value reported is the median. All data were acquired at 35°C.

[c]IQR is the interquartile range, a statistical measure of dispersion.

3.6 DISCUSSION

It has long been known that high doses of multivalent antigen cause rapid immobilization of IgE-FcεRI. A series of studies demonstrated that the extent of this immobilization correlated strongly with degranulation, leading to speculation that receptor immobilization may drive downstream signaling (Menon, Holowka et al. 1986; Mao, Varin-Blank et al. 1991; Pecht, Ortega et al. 1991; Pyenta, Schwille et al. 2003). However, technical limitations prevented a detailed examination of this hypothesis, since techniques did not exist which enabled dynamic studies of small receptor clusters in living cells. Multi-color single particle tracking is able to overcome these limitations and directly address the relationship between antigen-induced immobilization of IgE-FcεRI and the initiation of downstream signaling.

In this study, we systematically evaluated the rate and extent of antigen-induced immobilization as a function of antigen dose (Figure 3.1A) and compared these data with the extent of degranulation (Figure 3.1B) and clustering (Figure 3.2). When examined together, these data indicate that binding of multivalent antigen cross-links IgE-FcεRI into clusters whose size is dependent on antigen dose and that the size of the clusters dictates their mobility in the plasma membrane. Although it had been previously reported that the extent of receptor immobilization correlated with degranulation, our high spatiotemporal resolution data show that this is not in fact the case and that the small clusters formed at low antigen doses (0.001 μg/ml DNP-BSA) produce robust degranulation (Figure 3.1B) while remaining highly mobile.

Previous studies demonstrating that IgE dimers were able to induce large scale clustering suggested that these small oligomers induced a cellular response which in turn reorganized the small oligomers into larger aggregates (Menon, Holowka et al. 1984). We addressed this possibility by pre-treating cells with the Src-family kinase inhibitor PP2, which dramatically attenuated antigen-induced tyrosine phosphorylation (Figure 3.3C and D). While it is possible that as yet unknown signaling pathways downstream of FcεRI, which do not significantly rely on tyrosine phosphorylation, might still be active, our data strongly suggest that downstream signaling is not required for immobilization. Therefore, based upon our model that the extent of immobilization is due to extent of clustering by antigen, FcεRI signaling is also unlikely to be involved in cluster formation. In support of this, we observed large-scale aggregation of IgE-FcεRI even in the presence of PP2 (Appendix B, Supplementary Figure S3.3).

Given that cross-linking of only 5% of surface IgE-FcεRI is required to produce degranulation (Ortega, Schweitzer-Stenner et al. 1988), and the proposed existence of signal amplification to non-liganded receptors in the EGFR and TCR systems (Verveer, Wouters et al. 2000; Irvine, Purbhoo et al. 2002), we examined the possibility of signal amplification in the FcεRI system. By using two different specificities of IgE, we were able to independently cross-link discrete fractions of FcεRI on the cell membrane and probe for changes in organization and diffusion of the non-cross-linked FcεRI. We detected no appreciable changes in either the distribution or diffusion of non-antigen-bound IgE-FcεRI, despite cross-linking of the majority of IgE-FcεRI by multivalent antigen (Figure 3.4). This was consistent with a previous study in which a fraction of IgE-bound, cross-linked FcεRI and non-IgE-bound FcεRI were fractionated and probed

for tyrosine phosphorylation in response to cross-linking with anti-IgE (Paolini, Jouvin et al. 1991). This early study showed no detectable phosphorylation of non-IgE-bound FcεRI, despite extensive phosphorylation of cross-linked IgE-bound FcεRI. However, since the time of this study, it has been well documented that IgE-binding alone triggers substantial changes in FcεRI (Kitaura, Song et al. 2003; Kawakami and Kitaura 2005), therefore the presence of IgE on the non-cross-linked FcεRI in our study is an important distinction between these two experimental approaches. Additionally, our study supplements the phosphorylation data by demonstrating that the diffusive properties of non-cross-linked IgE-FcεRI are not appreciably altered by cross-linking a majority of IgE-FcεRI. This gives further credence to the idea that antigen-induced clustering of IgE-FcεRI is the sole driving force behind the observed changes in receptor diffusion.

Also of note, PP2-sensitive downstream signaling appeared to be dispensible for antigen-induced internalization of IgE-FcεRI (Figure 3.4E). This result is consistent with earlier studies in which the bulk of the cytoplasmic domains (i.e., ITAMs) of FcεRI did not appear to play a significant role in antigen-induced internalization of the receptor (Mao, Varin-Blank et al. 1991). Given that the extent of antigen-induced internalization correlates very well with the extent of antigen-induced immobilization and cluster formation (compare Figure 3.5E with Figures 3.1A and 3.2) and that immobilization and internalization are both unaffected by PP2 treatment, it seems reasonable to speculate that extensive clustering and the concomitant immobilization of FcεRI are sufficient to induce internalization. A study using confocal microscopy and antigen immobilized on substrates did not detect a recruitment of clathrin-coated pits or AP-2 to sites of antigen binding (Santini and Keen 1996), suggesting that immobilization of FcεRI alone is not

sufficient to induce internalization. However, a recent study showed that siRNA-mediated knockdown of clathrin heavy chain did not affect FcεRI internalization (Fattakhova, Masilamani et al. 2006). Given the apparent dispensability of clathrin for antigen-mediated internalization of FcεRI, it could be that immobilization alone could induce internalization through some clathrin- and AP-2-independent pathway.

In addition to providing an ideal platform for following the diffusion of single molecules, the unique spectral characteristics of QDs also facilitate multicolor imaging. We took advantage of these properties to probe the behavior of small clusters of receptors, an important topographical regime that cannot be readily addressed by traditional single molecule or ensemble imaging techniques. To accomplish this, we employed hyperspectral microscopy, which facilitates discrimination of multiple fluorescent species with narrowly separated emission maxima (Sinclair, Haaland et al. 2006). Together, our QD-based probes and hyperspectral imaging instrumentation allowed us to demonstrate that small antigen-induced oligomers of at least three IgE-FcεRI remain mobile on the cell surface and diffuse together as stable complexes for minutes (Figure 3.5). This result further supports the uncoupling of signaling from receptor immobilization, given that the dose of antigen used to generate these mobile oligomers was sufficient to trigger degranulation (Appendix B, Supplementary Figure S3.5).

We next examined the diffusion of multivalent antigen itself, using another QD-based probe, DNP-QD. These experiments corroborated the hyperspectral and single-color QD-IgE based measurements in showing that DNP-QD also remained mobile on the surface at doses sufficient to trigger degranulation (Figure 3.6). The fact that the

diffusion coefficient of DNP-QD was somewhat slower than that measured for QD-IgE (Table 3.1) is consistent with DNP-QD binding to multiple IgE-FcεRI and forming a small, stable complex as was directly observed in the hyperspectral imaging studies. Given that only a slight difference in DNP-QD diffusion was observed at doses both above and below the threshold for degranulation, it is likely that the aggregates formed under these two conditions are of comparable size and signaling activity and that degranulation occurs due to the increased number of signaling aggregates.

The picture that emerges from this work is that binding of multivalent antigen serves to cross-link multiple IgE-FcεRI together into small, stable aggregates that actively signal. At higher antigen doses, these clusters are more extensively cross-linked into larger aggregates, which become immobile and signal poorly. The mere existence of these large, immobile aggregates appears to be sufficient to trigger their internalization through a mechanism that may or may not involve clathrin coated pits. This series of events appears to be consistent with the current understanding of TCR signaling in the immune synapse. In the immune synapse, antigen-induced microclusters of TCR signal actively in the peripheral supramolecular activation complex (pSMAC) as they diffuse freely (Varma, Campi et al. 2006). These microclusters make their way to the central supramolecular activation complex (cSMAC) due to frictional coupling to the centripetal flow of actin (Kaizuka, Douglass et al. 2007; DeMond, Mossman et al. 2008). Once the microclusters reach the cSMAC, they coalesce, become immobile, and cease signaling prior to being internalized (Varma, Campi et al. 2006). Due to the micron-scale structure of the immune synapse, the diffusing microclusters are well-segregated from the larger, non-signaling clusters of TCR which are internalized in the cSMAC, facilitating study.

The soluble antigens used in the FcεRI system do not induce this cellular-scale reorganization, although recent studies have shown that mast cells are capable of forming an immune synapse when presented with surface-associated antigens (Juan Rivera, oral presentation, FASEB Summer Research Conference on Immunoreceptors, New Haven, CT, August 2008). However, due to the significant similarities in FcεRI response to soluble antigen and the TCR response to surface-associated antigen, a model emerges in which cluster size is the primary regulator of signaling.

In both FcεRI and TCR signaling, low levels of multivalent antigen induce the formation of small receptor clusters which signal actively while remaining relatively free to diffuse. The formation of larger clusters, whether due to high doses of soluble antigen or centripetal actin flow-mediated aggregation of existing small clusters of receptors, causes receptor immobilization, signal termination, and internalization (Figure 3.7).

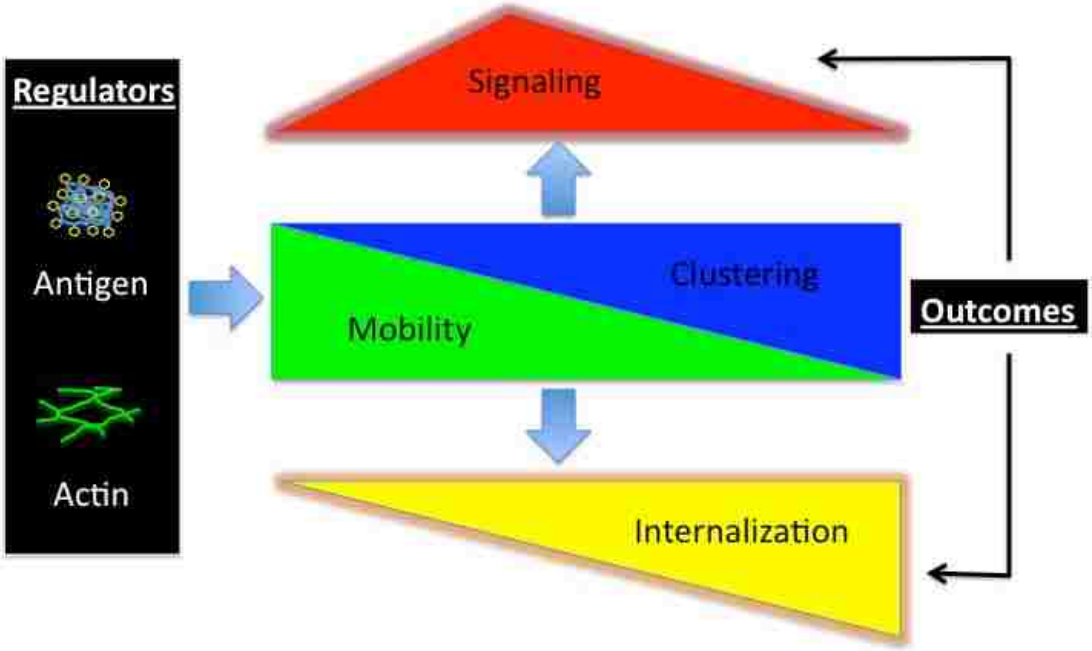

Figure 3.7 Cluster-centric model of MIRR signaling. Antigen dose and valency, as well as actin, modulate receptor clustering, which is inversely related to receptor mobility. The extent of clustering is the primary regulator of internalization, which occurs most extensively in the context of large, immobile clusters; and also of signaling, which occurs most efficiently in the context of small, mobile clusters.

This model provides a common framework for understanding multichain immune recognition receptor signaling in the context of both soluble and surface-associated antigens and identifies the extent of receptor oligomerization as the controlling force underlying receptor mobility, activity, and internalization.

3.7 MATERIALS AND METHODS

3.7.1 Reagents

Mouse monoclonal $IgE_{anti\text{-}DNP}$ was prepared as described in (Liu, Bohn et al. 1980). Mouse monoclonal $IgE_{anti\text{-}dansyl}$ was from BD Biosciences (San Jose, CA). Latrunculin B was from Sigma-Aldrich (St. Louis, MO). DNP-BSA was from Invitrogen (Carlsbad, CA). PP2 was from Calbiochem (La Jolla, CA). Antiphosphotyrosine antibodies (PY20/PY99) were from Santa Cruz Biotechnology (Santa Cruz, CA). HRP-conjugated secondary antibodies and SuperSignal® West Pico Chemiluminescent Substrate kit were from Pierce Protein Research Products (Rockford, IL). QD-IgE was prepared as described in (Andrews, Lidke et al. 2008). Stock solutions of QD-IgE were stored at 4°C and used within four weeks. Alexa-labeled derivatives of IgE were prepared according to the instructions provided with the Alexa Fluor® 488 or Alexa Fluor® 633 Microscale Protein Labeling Kits (Invitrogen, Carlsbad, CA). To facilitate comparisons between unlabeled and QD-labeled reagents, 5 nM IgE or 14 nM DNP-BSA is equivalent to 1 µg/ml.

3.7.1.1 Synthesis of DNP-QD

A 1 mM biotin-DNP stock solution was prepared by dissolving 1 mg DNP-X-biocytin-X succinimidyl ester (Molecular probes) in 100 µl dimethylsulfoxide (Sigma) followed by reaction with ammonium bicarbonate (Sigma) in a 1:10 stoichiometric ratio in water for 30 minutes to quench the succinimidyl ester group. The stock solution was stored at 4°C. DNP-QD was prepared by reacting biotin-DNP with the indicated Qdot® Streptavidin conjugate (Invitrogen) in a 50:1 ratio in PBS + 1% BSA for four hours at 4°C. DNP-QD

was then purified by dialysis against PBS and the final concentration determined by absorption at 532 nm. Stock solutions were stored at 4°C and used within four weeks.

3.7.1.2 Synthesis of dansyl-BSA

Dansyl-BSA was prepared by slight modification of the protocol provided with Dansyl-X, SE (Invitrogen, Carlsbad, CA) to yield a dansyl:BSA ratio of 69.3 as measured by absorbance at 335 and 280 nm. Dansyl-BSA was stored in 30 µl aliquots at -20°C and thawed immediately before use.

3.7.2 Cell culture

Rat basophilic leukemia (RBL-2H3) cells were grown as adherent monolayers in minimum essential medium with 10% fetal calf serum (MEM/FBS) (Invitrogen, Carlsbad, CA) as described in (Wilson, Pfeiffer et al. 2000). For microscopy, cell monolayers were cultured in 8-well Lab-Tek chambers (Nunc, Rochester, NY) 24 hours before experiments.

3.7.3 Degranulation assay

Cell monolayers were grown in 24-well tissue culture plates for 24 hours. FcεRI were primed by adding 5 nM $IgE_{anti\text{-}DNP}$ or $IgE_{anti\text{-}dansyl}$ to cultures overnight. After washing away excess IgE, cells were either pre-incubated or not with 10 µM PP2 for 10 min and then activated with DNP-BSA ± 10 µM PP2, dansyl-BSA, or DNP-QD at the indicated doses. Release of β-hexosaminidase was measured as described in (Ortega, Schweitzer-Stenner et al. 1988).

3.7.4 IP and Western Blotting

Cells were grown to confluency in TC-60 dishes in MEM/FBS, washed with HBSS, and then stimulated in HBSS at 37°C for the indicated times and with the indicated doses of DNP-BSA. After a PBS rinse, cells were solubilized in cold NP-40 lysis buffer (150 mM NaCl, 50 mM Tris/HCl pH 7.2, 1% NP-40, 5 µg/ml leupeptin, 5 µg/ml antipain, 1 mM NaVO4, 1 mM PMSF). Lysates were clarified by centrifugation. Supernatants were mixed with 5x sample buffer for SDS-PAGE and subsequent transfer to nitrocellulose membranes. Blocked membranes were probed with primary and HRP-conjugated secondary antibodies, followed by detection of bands by ECL (Pierce, Rockford, IL).

3.7.5 Wide-field imaging

All single particle tracking was performed using an Olympus IX71 inverted microscope equipped with a 60× 1.3 N.A. water objective. Wide field excitation was provided by a mercury lamp with the indicated excitation filters. Emission was collected by an electron multiplying CCD camera (Andor iXon 887). A two-color (Cairn Research OptoSplit II, Kent, U.K.) or four-color (MAG Biosystems Quad-View) image splitter was used to simultaneously image multiple spectral channels. Each channel was projected onto the CCD as a 128x128 pixel image. When required, registration of the images was achieved using an image of fluorescent beads (0.2 µm Tetraspeck, Invitrogen) which have an emission spectrum covering the two spectral windows. For details, see (Andrews, Lidke et al. 2008). The sample temperature was maintained at 34-36 °C by an objective heater (Bioscience Tools, San Diego, CA).

3.7.5.1 SPT of QD-IgE

RBL-2H3 cells in 8-well Lab-Tek chambers were labeled with 500 pM QD655-$IgE_{anti\text{-}DNP}$ in HBSS for 10 min at 37°C prior to imaging. Where indicated, cells were then incubated with 50 nM $IgE_{anti\text{-}DNP}$ or $IgE_{anti\text{-}dansyl}$ for 30 min at 37°C in MEM/FBS, washed, and then stimulated during imaging with the indicated doses of DNP-BSA ± 10 μM PP2 or dansyl-BSA while imaging at 5 to 33 frames/s at 35°C. Images were acquired using a 436/10 nm BP excitation filter and emission collected by a 600 nm dichroic mirror and a 655/40 nm BP emission filter. The resulting image series were analyzed and diffusion coefficients obtained using previously described single particle tracking algorithms (Andrews, Lidke et al. 2008). PP2 had no measureable effect on IgE binding (data not shown).

3.7.5.2 SPT of DNP-QD

RBL-2H3 cells in 8-well chambers were primed by 30 min incubation with 50 nM $IgE_{anti\text{-}DNP}$ at 37°C in MEM/FBS, washed with HBSS and then imaged in HBSS at 35°C. One pM DNP-QD655 was added at the microscope and images acquired at 33 frames/s. Cells then received 500 pM DNP-QD585 for 2 min and images again acquired at 33 frames/s. Images were acquired using a 436/10 nm BP excitation filter and emission was collected through a 500 nm LP filter, which sent light to the two-color image splitter equipped with a 600 nm dichroic mirror and 655/40 nm and 585/20 BP emission filters. The resulting image series were analyzed and diffusion coefficients calculated using previously described single particle tracking algorithms (Andrews, Lidke et al. 2008).

3.7.5.3 Kinetics of immobilization assay

RBL-2H3 cells were labeled with a 1:1 mixture of 500 pM QD625- and QD705-$IgE_{anti-DNP}$ for 10 min at 37°C in HBSS, washed, and then incubated at 37°C for 30 min with 140 nM $IgE_{anti-DNP}$. Cells were washed and imaged at 20 frames/s at 35°C in 200 µl HBSS for ~10 seconds, at which point 100 µl of 3X DNP-BSA was added at the indicated concentrations. Images were acquired with a 436/10 nm BP excitation filter, and a 500 nm LP emission filter which sent light to a two-color image splitter equipped with a 655 nm dichroic mirror and 625/26 nm and 710/40 nm BP emission filters. Instantaneous diffusion coefficients were calculated as described in (Andrews, Lidke et al. 2008) and the traces from multiple cells (resting, n=51; 10 µg/ml, n=11; 1 µg/ml, n=9; 0.1 µg/ml, n=10; 0.01 µg/ml, n=10; 0.001 µg/ml, n=16) averaged to generate the final plot.

3.7.6 Confocal imaging of $IgE_{anti-DNP}$ and $IgE_{anti-dansyl}$

RBL-2H3 cells were grown overnight on 15 mm round glass coverslips in MEM +10% FBS containing 0.5 µg/ml each Alexa488-$IgE_{anti-DNP}$ and Alexa647-$IgE_{anti-dansyl}$. Cells were then washed with HBSS and stimulated with either 0.1 µg/ml DNP-BSA, dansyl-BSA or both (0.05 µg/ml each) in HBSS for 1 min. After stimulation, cells were washed in HBSS and fixed by 20 min incubation in 2% paraformaldehyde. After fixation, cells were mounted in ProLong AntiFade Gold® and imaged on an LSM510 META imaging system equipped with a 63× 1.4 N.A. oil objective. Excitation was provided by a 488 nm Argon laser alternated with a 633 nm HeNe laser for independent excitation of Alexa 488 and Alexa 633, respectively. Emission was collected through a 545 nm dichroic mirror and 505-530 nm BP or 650 nm LP emission filters for Alexa 488 and Alexa 633, respectively. The confocal slice thickness was 1 µm.

3.7.7 Hyperspectral imaging microscopy

Cells were grown by overnight culture on 15 mm diameter round coverslips. Cells were labeled by 15 min incubation at 22°C with a mixture of QD655-, QD625-, QD585-, QD565-, and QD525-IgE at 400 pM each in HBSS. Cells were then washed with HBSS before mounting in HBSS +/- 0.1 µg/ml DNP-BSA on 25x75 mm glass slides using a 2 mm rubber spacer. Samples were then imaged by hyperspectral microscopy as described in (Sinclair, Haaland et al. 2006). Within two minutes of mounting the sample, confocal image series consisting of 60 frames at a rate of 0.25 Hz were acquired. The resulting images series were then subtracted for dark current and despiked (Sinclair, Haaland et al. 2006) and displayed using a custom image analysis program (Sinclair, Haaland et al. 2006). Regions of interest could then be manually selected and the spectra from these regions obtained.

3.7.8 Electron microscopy

RBL-2H3 cell monolayers on glass coverslips were primed by overnight incubation with 5 nM $IgE_{anti\text{-}DNP}$. Cells were then washed with PBS and stimulated with the indicated doses of DNP-BSA for the indicated times. Cells were fixed for seven min in 0.5% paraformaldehyde and membrane sheets prepared as described in (Wilson, Pfeiffer et al. 2000). Electron micrographs were acquired using a transmission electron microscope (Hitachi H600). Probe identification and statistical analyses were performed as described in (Zhang, Leiderman et al. 2006). For plotting cluster size as a function of time and antigen dose, we employed a cut-off distance of 50 pixels (43 nm), such that any

receptors within the cutoff distance of each other were considered part of the same cluster.

3.7.9 Flow cytometry

RBL-2H3 cells were primed in suspension by 2 hour incubation at 37°C with 2 µg/ml Alexa488-IgE in MEM + 10% FBS. Cells were then pelleted and washed once with HBSS. After washing, cells were incubated in the presence or absence of 10 µM PP2 for 10 min in HBSS, followed by stimulation for 2 or 10 min with the indicated doses of DNP-BSA, in the presence or absence of 10 µM PP2 in HBSS. Samples were then split into two and one sample for each condition was subjected to a light acid strip by 10 min incubation at 4°C in 0.5 M NaCl and 0.2 M acetic acid (pH 2.7) to remove any surface-accessible Alexa488-IgE. All samples were then fixed by 20 min incubation in 2% Paraformaldehyde at 25°C in PBS, and Alexa488 fluorescence read by flow cytometry. The ratio of the acid-stripped and non-stripped samples for each condition was then used to calculate the percentage of internalized IgE-FcεRI.

3.7.10 Statistical analysis

Due to the wide range of values and nonparametric distribution of $D_{1\text{-}3}$, values are reported as medians and interquartile range is provided as a measure of statistical dispersion. Statistical comparisons between data sets were made using the Kolmogorov-Smirnov test unless otherwise noted and significance was defined as $p<0.05$.

3.7.11 Image Processing

All image processing was performed using Matlab (The MathWorks, Inc., Natick, MA) in conjunction with the image processing library DIPImage (Delft University of Technology). Descriptions of specific analysis routines has been reported previously (Andrews, Lidke et al. 2008).

3.8 ACKNOWLEDGEMENTS

This work was supported by NIH grants R01 GM49814, R01 AI051575 and P20 GM 67594, the Oxnard Foundation, ACS IRG 192, and by the Sandia SURP program. Sandia is a multi-program laboratory operated by Sandia Corporation, a Lockheed Martin Company, for the United States Department of Energy under contract DE-AC04-94AL85000. Nicholas Andrews was supported by NSF IGERT DGE-0549500 and the UNM-SOM MD/PhD Program. We thank Sheli Ryan for cell culture assistance. The UNM Cancer Center Fluorescence Microscopy Facility received support from NIH grants S10 RR14668, S10 RR19287, S10 RR016918, P20 RR11830 and P30 CA118100 and from NSF grant MCB9982161. Electron micrographs were generated in the University of New Mexico Electron Microscopy Facility, which received support from NIH grants P20 GM067594, S10 RRI5734 and RR022493.

CHAPTER 4: SUMMARY, IMPLICATIONS, AND FUTURE STUDIES

4.1 SUMMARY

The preceding studies were designed to address the hypothesis that immobilization of FcεRI was the inciting event that triggered a cellular response and induced downstream signaling and large-scale reorganization of FcεRI into large aggregates on the cell surface. To address this hypothesis, we developed QD based probes for use in single molecule tracking experiments that enabled us to rigorously assess the diffusion and topography of FcεRI in the context of signal initiation. From these experiments, we not only characterized the diffusion of FcεRI, but also uncovered a new role for the actin cytoskeleton in influencing diffusion of transmembrane proteins on micron length scales. Our experiments demonstrate that receptor immobilization is not required for antigen-induced FcεRI signaling, yet appears to be required for receptor internalization. The processes of receptor aggregation, immobilization, and internalization did not appear to require downstream signaling. In light of the experiments described here, aggregation and immobilization can be best explained by extensive cross-linking of receptors that occurs at high doses of multivalent antigen. However, the mechanism by which IgE-FcεRI internalization occurs merits further study.

4.1.1 Chapter 2 summary

While there had been multiple studies examining the diffusion of FcεRI, only a handful had done so at the level of individual receptors (Feder, Brust-Mascher et al. 1996; Barisas, Smith et al. 2007). However, these prior studies were hindered by either large probes (Feder, Brust-Mascher et al. 1996), known to significantly alter membrane protein diffusion (Saxton and Jacobson 1997) or labeling at non-physiological

temperatures (Barisas, Smith et al. 2007), which has since been shown to markedly reduce membrane protein diffusion (Suzuki, Ritchie et al. 2005). We therefore developed a QD-based probe, QD-IgE, which would not significantly affect FcεRI diffusion due to its small size (Dahan, Levi et al. 2003), yet would enable rapid acquisition of images over long time periods due to its brightness and photostability (Dahan, Levi et al. 2003; Lidke, Lidke et al. 2005). We performed our labeling and measurements at physiological temperatures (37°C). In characterizing our QD-IgE probe, we determined that it was functionally monovalent (Figure 2.1, S2.1) and still able to bind antigen and activate cells (Figure 2.1 and Video 2.1). We were able to calculate diffusion coefficients under a variety of conditions (Table 2.1) and detected the expected four modes of diffusion: free, restricted, directed, and immobile (Figure S2.3).

During our measurements of FcεRI diffusion, we noted what appeared to be evidence of attraction between FcεRI (Video 2.2). Taking advantage of multi-color imaging, we examined this behavior more closely and determined that it was consistent with co-confinement of multiple FcεRI in the same sub-region of the plasma membrane; not attractive forces between receptors (Figures 2.2, 2.3 and S2.4). Since the actin cytoskeleton had previously been implicated in restricting diffusion of plasma membrane components (Jacobson, Sheets et al. 1995; Kusumi, Nakada et al. 2005), we transfected RBL-2H3 cells with GFP-actin in order to simultaneously visualize FcεRI diffusion and actin dynamics. We observed that actin filament bundles defined dynamic, micron-sized domains that reorganized on the time scale of seconds, transiently confining mobile receptors (Figure 2.4 and Videos 2.3, 2.4, and 2.5). Our analyses indicated this

confinement was due to actin acting as a physical barrier to diffusing receptors (Figure 2.5).

To determine if this transient receptor co-confinement played a role in antigen-induced immobilization of FcεRI, we developed an assay that enabled us to follow the kinetics of this process in real time. Using this assay, we showed that receptors become immobilized within seconds of cross-linking and that disruption of the actin cytoskeleton results in delayed immobilization kinetics and an increased diffusion rate of cross-linked clusters (Figure 2.6). These results implicated actin in membrane partitioning that not only restricts diffusion of membrane proteins, but also dynamically influences their long-range mobility, sequestration, and response to ligand binding.

4.1.2 Chapter 3 summary

It had long been observed that treatment with multivalent antigen lead to a rapid immobilization of IgE-FcεRI (Menon, Holowka et al. 1986; Mao, Varin-Blank et al. 1991; Pecht, Ortega et al. 1991; Pyenta, Schwille et al. 2003). Given that several studies had demonstrated a link between a cross-linking agent's ability to induce receptor immobilization and its ability to trigger degranulation, it was believed that the two were causally related (Menon, Holowka et al. 1986; Mao, Varin-Blank et al. 1991; Pecht, Ortega et al. 1991; Pyenta, Schwille et al. 2003). To directly address the causal relationship between antigen-induced FcεRI immobilization, signal initiation, and internalization, we again turned to QD based probes and single molecule tracking.

Using the kinetics of immobilization assay we had developed previously (Andrews, Lidke et al. 2008), we demonstrated that the kinetics and extent of

immobilization are highly dependent on antigen concentration and that the extent of immobilization does not appear to correlate with degranulation (Figure 3.1). Using TEM, we were able to quantify receptor clustering as a function of antigen dose and demonstrated a very close correlation between the extent of clustering (Figure 3.2) and the kinetics and extent of immobilization (Figure 3.1).

Early reports had suggested that IgE dimers were capable of eliciting large-scale reorganization of FcεRI into very large aggregates, leading to speculation that initial signaling by small oligomers of receptors signaled a larger reorganization of receptors into aggregates (Menon, Holowka et al. 1984). To examine this possibility, we used the Src-family kinase inhibitor PP2, which inhibits the earliest steps in FcεRI signaling (Figure 3.3C and D). We found that PP2 treatment did not significantly affect antigen-induced immobilization, aggregation, or internalization of FcεRI (Figures 3.3E, F and S3.3), indicating that none of these processes are dependent upon downstream signaling.

While the vast majority of experiments are performed by priming cells with a single specificity of IgE, in the physiological state, it is estimated that <10% of FcεRI on a cell are specific for the same antigen (Johansson, Oman et al. 2006). Consistent with this, it has been shown in the laboratory that only ~5% of surface FcεRI need to be engaged to produce a secretory response (Ortega, Schweitzer-Stenner et al. 1988). Together, these observations raise the possibility of signal amplification between engaged and non-engaged FcεRI as has been described in other receptor systems (Verveer, Wouters et al. 2000; Irvine, Purbhoo et al. 2002). By employing two different specificities of IgE, we showed that each specificity forms clusters independently and

that cross-linking one subset of receptors does not significantly affect the diffusion or distribution of non-cross-linked receptors (Figure 3.4).

Our observations that IgE-FcεRI did not appear to markedly slow its diffusion upon exposure to low, activating doses of multivalent antigen led us to attempt to directly visualize these small clusters using hyperspectral microscopy. The hyperspectral microscope designed and built by our collaborators at Sandia National Laboratories, enabled us to simultaneously excite and spectrally discriminate individual QDs, even when they were from the same "class" of QDs (e.g. Qdot® 565) (Lidke, Andrews et al. 2007). We labeled RBL-2H3 cells with a mixture of QD525-, QD565-, QD605-, QD625-, and QD655-IgE, and imaged the cells in the presence and absence of a low, activating dose of multivalent antigen. We observed that small, antigen-induced clusters of at least three IgE-FcεRI remain freely mobile on the cell surface under conditions in which activation is occurring (Figures 3.5 and S3.5).

To corroborate these findings, we developed a second QD-based probe to enable us to monitor the diffusion of multivalent antigen upon binding to IgE-FcεRI on the cell surface. Using this DNP-QD we observed that it too remains mobile on the cell surface at activating doses (Figure 3.6). In further support of the signaling competence of small, mobile IgE-FcεRI clusters, we also performed simultaneous tracking of QD-IgE and Ca^{2+} ratio imaging at various doses of multivalent antigen. These experiments showed Ca^{2+} oscillations in response to low doses of DNP-BSA while QD-IgE-FcεRI remained highly mobile (Figure S3.2). Altogether, our results demonstrate that antigen-induced immobilization is due solely to formation of large receptor clusters and is required for FcεRI internalization; not signal initiation.

4.2 IMPLICATIONS

4.2.1 Implications for FcεRI diffusion and plasma membrane structure

The results presented in Chapter 2 have significant implications for both the diffusion of FcεRI, and for our understanding of plasma membrane structure. In the case of FcεRI, our results provide rigorous quantification of receptor diffusion under physiological labeling and imaging conditions. In addition, the experiments detailing the kinetics of antigen-induced immobilization provide a unique dataset for following receptor activation in real time. All of these data can be used to facilitate mathematical simulations that will enable us to further probe the complex process of FcεRI activation on spatiotemporal scales that remain inaccessible to modern biological techniques.

Perhaps most striking are the insights into membrane organization provided by the data presented in Chapter 2. It is true that actin has long been implicated in modulating receptor diffusion over time scales of milliseconds and distances of nanometers (Kusumi, Sako et al. 1993; Jacobson, Sheets et al. 1995; Kusumi, Nakada et al. 2005). These previous studies have provided an explanation for the phenomenon that diffusion of transmembrane proteins is typically about 50-fold slower when measured in actual cell membranes compared to measurements made in artificial bilayers (Kusumi, Nakada et al. 2005). This is believed to be due to rapid diffusion within nanometer scale actin-defined domains coupled with an occasional "hop diffusion" event in which the membrane protein (or lipid) crosses into an adjacent actin-defined domain (Kusumi, Nakada et al. 2005). Since the diffusion within actin-defined domains consists of many rapid, short displacements, measurements acquired at slower frame rates only detect the

hops between compartments and therefore return an apparently slower diffusion rate. These actin-defined domains are generally considered to exist as a static meshwork and have only been directly visualized in fixed samples by EM (Morone, Fujiwara et al. 2006). Since nanometer scale features are currently unable to be resolved in live samples, the dynamic behavior of these structures remains unclear. However, given that the micron-scale confinement we observed appeared to be due to actin acting as a physical barrier, and that this physical barrier explanation is also believed to underly nanometer scale confinement (Kusumi, Nakada et al. 2005), it is intriguing to consider that the highly dynamic behavior of micron scale actin structures may also extend to nanometer scale structures.

Regardless of nanometer scale membrane dynamics, that seemingly similar processes are at work over micron distances adds an additional layer of complexity to our evolving understanding of membrane architecture. While this level of organization has only so far been described in our work, it is our expectation that micron-scale confinement by dynamic actin structures will prove to be at work in a wide variety of cell types and receptor systems. As for its functional role, we speculate that this co-confinement may facilitate productive encounters between receptors in the context of multivalent antigen binding. Our results indicating that the kinetics and extent of antigen-inuced immobilization are dependent on an intact actin cytoskeleton (Figure 2.6) suggest that this may in fact be the case. However, it is true that a wide variety of cellular processes rely on actin, and it could very-well be that actin facilitates antigen-induced receptor clustering by some as yet unclear mechanism. At a minimum, the results described in Chapter 2 describe a heretofore unappreciated role for the actin

cytoskeleton in dynamically modulating diffusion of transmembrane proteins over micron-length scales.

4.2.2 Implications for multichain immune recognition receptor activation

The results presented in Chapter 3 serve to directly address the main aim of our overall hypothesis; namely that antigen-induced immobilization of FcεRI serves as the inciting event that initializes signaling, reorganization into large receptor clusters, and internalization. Given the results presented in Chapter 3, the initial hypothesis clearly requires some refinements. This hypothesis seemed quite plausible given the bulk of studies which showed a clear link between extent of immobilization and extent of degranulation (Menon, Holowka et al. 1986; Mao, Varin-Blank et al. 1991; Pecht, Ortega et al. 1991; Pyenta, Schwille et al. 2003). However, nearly all of the studies of FcεRI diffusion to date have employed relatively high doses of cross-linking agent, with one notable exception. The early work by Schlessinger, *et al*. indicated that when FITC-IgE-FcεRI was crosslinked with low, activating levels of anti-FITC antibodies, the receptors remained mobile on the cell surface (Schlessinger, Webb et al. 1976). This result is in accordance with our rigorous examination of the relationship between diffusion and signal initiation, which calls for a new paradigm for FcεRI signaling.

Our results definitively eliminate a role for downstream signaling in clustering, immobilization, and internalization of FcεRI and place control of these processes solely on antigen concentration and valency. At low concentrations and/or valency, antigen binding induces the formation of small oligomers of IgE-FcεRI, which remain stably associated as they continue diffusing in the membrane. These small, mobile clusters

actively signal. As cross-linking continues with higher concentrations of antigen, these small oligomers coalesce into large aggregates which, due solely to their large size, become effectively immobilized on the cell surface. The signaling state of these large aggregates remains to be definitively determined, however our data suggests that they do not signal effectively. The mere presence of these large, immobile aggregates is sufficient to trigger their internalization through an as yet undefined mechanism.

This "cluster-size centric" model of FcεRI signaling also appears to be consistent with observations of TCR signaling in the context of the immune synapse. When encountering surface-associated antigen, T-cells form a highly organized, radially symmetric contact with the surface or antigen presenting cell (Grakoui, Bromley et al. 1999). This organization greatly facilitates study of TCR signaling by providing micron-scale segregation of receptors in various states of activation. Studies of the T-cell immune synapse have revealed that microclusters of TCR form in the periphery of the cell-surface contact and signal actively as they migrate toward the center of the contact where the mircoclusters coalesce, immobilize, cease signaling and are internalized (Kaizuka, Douglass et al. 2007). The striking organization of the immune synapse would lead one to speculate that it is this cellular-level organization that dictates the signaling activity, mobility, and internalization of ligand-bound TCR. However, given the aforementioned similarities between TCR and FcεRI signaling, and our results demonstrating that cluster size appears to be the primary driver of these processes in the FcεRI system, it seems reasonable to speculate that cluster size is also dictating activation state and mobility of the TCR.

4.3 FUTURE STUDIES

4.3.1 Future Study 1: Probing the dynamics of non-IgE-bound FcεRI

While the studies detailed here have provided a wealth of insight into the dynamics of IgE-FcεRI, there has been very little work on the behavior of FcεRI when it is not bound to IgE. Labeling IgE with fluorescent molecules ex-vivo and then adding these fluorescent derivates to cells expressing FcεRI has provided a highly convenient method of probing FcεRI behavior. However, due to this convenience, very few investigators have developed methods to label FcεRI without the use of IgE. Indeed, until recently it was assumed that IgE had no effect on FcεRI other than to confer the receptor with the ability to bind antigen. Recent studies have shown that IgE binding alone mediates a wide range of effects, including stabilization of FcεRI at the cell surface, enhanced proliferation, cytokine secretion, and, in some cases, degranulation (Kitaura, Song et al. 2003; Kawakami and Kitaura 2005). Perhaps the most intriguing of these is the stabilization of FcεRI at the cell surface. In the presence of IgE, the number of FcεRI on the cell surface increases dramatically (Yamaguchi, Lantz et al. 1997). This increase is not dependent upon protein synthesis and is therefore believed to be due to a decrease in the rate of receptor internalization (Yamaguchi, Lantz et al. 1997). Exactly how IgE mediates this effect is not known, due in large part to the dearth of knowledge about the behavior of the non-IgE-bound FcεRI.

To address the behavior of non-IgE-bound FcεRI, we propose using a genetically encoded tag fused to the amino terminus of the α-subunit. An 11 amino acid tag (DSLEFIASKLA) can serve as a target sequence for phosphopantetheinyl transferase (PPT) (Yin, Straight et al. 2005). The endogenous function of this enzyme is to transfer acyl chains from acyl-CoA to the serine residue in the target sequence within certain

proteins. This system can be adapted by engineering organic molecules with a fluorescent tag or biotin linked to CoA. When these CoA derivatives are added to cells containing a protein with the DSLEFIASKLA sequence in the presence of PPT, the fluorescent tag is transferred from CoA to the target sequence, covalently linking the organic dye to the protein of interest (Yin, Straight et al. 2005).

This so-called acyl carrier protein (ACP) labeling system could be used to covalently label the non-IgE-bound FcεRI and its dynamics and recycling could be monitored by fluorescence microcopy. By double-transfecting cells with DSLEFIASKLA-FcεRIα and GFP-clathrin, cells could be partially loaded with fluorescent IgE and the extent of association of IgE-FcεRI and FcεRI alone with clathrin coated pits could be quantified, revealing any potential differences in clathrin-mediated endocytosis of the two forms of the receptor.

4.3.2 Future Study 2: Dose dependent temporal regulation of FcεRI signaling

The studies detailed in Chapter 3 showed a clear relationship between antigen dose and the size of clusters formed. In the cluster-centric model we proposed, small oligomers signal actively and larger aggregates do not signal efficiently. It would be useful to examine this aspect of the model through western blot studies. RBL-2H3 cells would be stimulated with various doses of DNP-BSA (0.001 to 10 μg/ml) and the cells lysed at several timepoints (0.5, 1, 2, 5, 10, 20, and 30 min). From these lysates, FcεRI would be immunoprecipitated and analyzed by SDS-PAGE. The resulting blots could then be probed with antiphosphotyrosine antibodies and a time course of FcεRI phosphorylation could therefore be obtained for each dose of antigen. If the model is

correct, one would expect the lowest antigen doses to produce somewhat lower levels of phosphorylation that would persist out to the longer time points. In contrast, the higher levels of antigen, which elicit slightly less secretion, would be expected to show rapid receptor phosphorylation followed by a rapid decline in phosphorylation, indicating signal termination. The differences in signal duration elicited by the various antigen doses may underlie the associated differences in degranulation, with lower doses producing robust degranulation and higher doses resulting in an attenuated secretory response.

4.3.3 Future Study 3: Mechanism of FcεRI internalization

In the EM studies of FcεRI signal initiation, multivalent antigen treatment results in receptors localizing to structures that strongly resemble clathrin coated pits (Pfeiffer, Seagrave et al. 1985; Wilson, Pfeiffer et al. 2000). However, studies attempting to specifically address the role of clathrin coated pits in FcεRI internalization have yielded results that appear to conflict with the EM data. One study using confocal microscopy and surface-immobilized antigen failed to detect a recruitment of clathrin to sites of FcεRI clustering (Santini and Keen 1996). Additionally, when siRNA was used to knock down clathrin and AP-2, no appreciable differences in antigen-induced internalization of FcεRI were observed (Fattakhova, Masilamani et al. 2006). Further clouding the issue was a study in which various truncation mutants of FcεRI were assessed for their ability to be internalized and it was discovered that internalization was not dependent upon the bulk of the cytoplasmic domains of FcεRI (Mao, Varin-Blank et al. 1991). Add to this our own data from Chapter 3 which showed that internalization was not at all dependent

on downstream signaling (Figure 3.3), and one is left with a clear sense that this is a process that warrants further investigation.

To further investigate the role played by clathrin in FcεRI internalization, we could again turn to cells transfected with GFP-clathrin. By loading these cells with fluorescent IgE and then stimulating them with various doses of multivalent antigen (possibly DNP-QD for three-color experiments) and imaging by confocal microscopy, the extent of colocalization between aggregated IgE-FcεRI and GFP-clathrin could be quantified.

To follow up on the siRNA studies which knocked down clathrin, other components of the internalization machinery, such as caveolin and dynamin could be systematically knocked out and their effects on FcεRI internalization evaluated.

4.4 CONCLUDING REMARKS

In this study, we have rigorously quantified the dynamics and topography of FcεRI in the context of signal initiation. In the process, we identified previously unrecognized co-confinement of FcεRI by dynamic, micron-scale features of the actin cytoskeleton and provided a model by which this new spatiotemporal level of membrane organization dovetails with existing conceptions of membrane architecture on the nanometer scale. Using state-of-the-art live cell imaging techniques, QD-based probes, and hyperspectral microscopy, we have systematically and thoroughly examined the role of receptor clustering, mobility, and internalization in the regulation of FcεRI signaling. These studies have provided definitive answers to long-standing questions in the field of

FcεRI signal initation and have formed the basis for a new cluster-centric paradigm for regulation of multichain immune recognition receptor signaling.

APPENDIX A: SUPPLEMENTARY INFORMATION FOR CHAPTER 2

APPENDIX A. SUPPLEMENTARY INFORMATION FOR CHAPTER 2

A.1 Supplementary Figures for Chapter 2

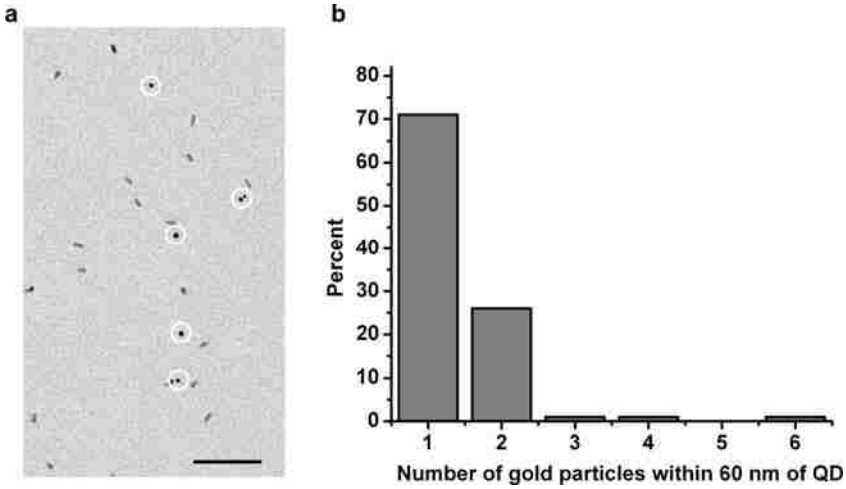

Figure S2.1 QD-IgE is predominantly monovalent. A number of analyses were performed to assess the valency of QD-IgE. In addition to the degranulation and biotinylation assays described in the main text, we carried out EM experiments (see Supplementary Methods for more detail) as shown here. (**a**) Representative electron micrograph of QD-IgE + DNP-BSA-gold. Gold particles (5 nm) are marked with white circles. Scale bar represents 100 nm. (**b**) Graph showing the distribution of the number of DNP-BSA-gold probes within 60 nm of QD-IgE (n = 107). We reason that if QD-IgE were predominantly monovalent, then each complex would have a maximum of two available binding sites for DNP-BSA-gold (IgE valency for DNP = 2). In fact, we find that the majority of the QDs have only one gold particle nearby, further supporting the monovalent nature of QD-IgE.

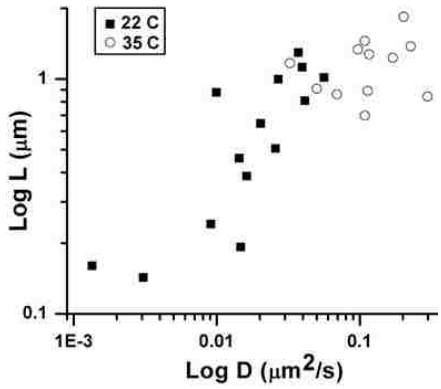

Figure S2.2 Influence of temperature on diffusion. Log-log plot of diffusion coefficient (D) versus restricted region size (L) for trajectories the restricted diffusion model at 22°C (filled squares) and 35°C (open circles). The plotted D and L values were determined by fitting the restricted diffusion equation MSD = *offset* + $(L^2/3)(1-\exp(-\Delta t / \tau))$ (ref (Destainville and Salome 2006)), where $D=L^2/12\tau$ to the first 10% of the data points in each MSD plot. It is apparent that at physiological temperature, D is faster and L is larger than at ambient temperature.

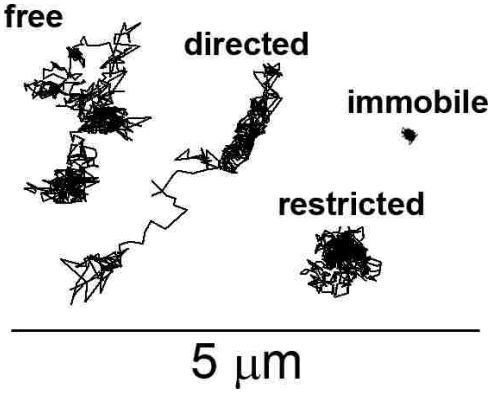

Figure S2.3 QD-IgE-FcεRI exhibits four motional modes. Representative trajectories of QD-IgE-FcεRI are shown. We observed four types of diffusion for FcεRI in resting cells at 35°C: free (65%), restricted (23%), immobile (4%) and directed (8%). Trajectories were classified by a slight modification of the method described in (Kusumi, Sako et al. 1993).

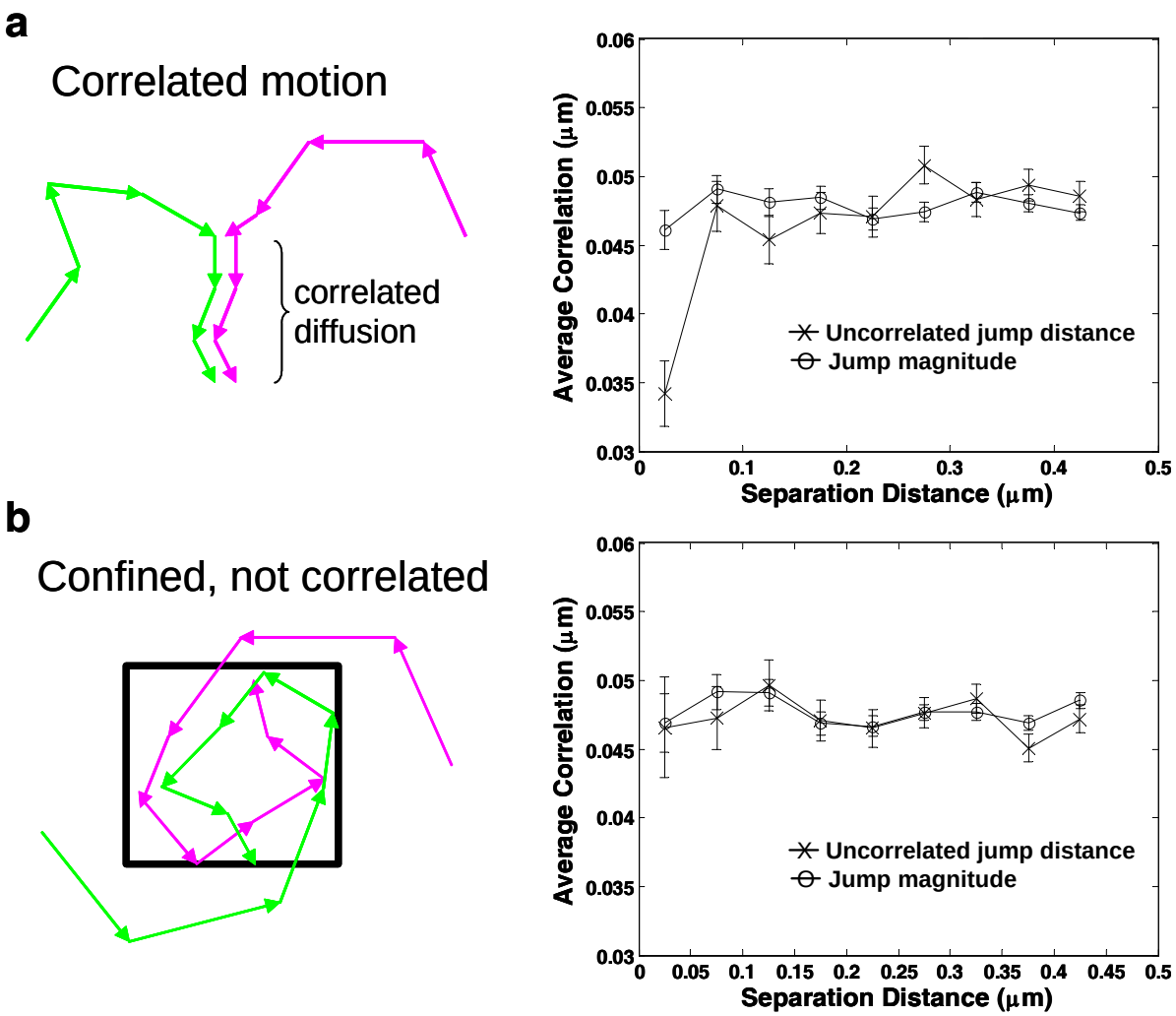

Figure S2.4 Analysis of simulated receptor dimerization or co-confinement. Particles undergoing free Brownian diffusion (D = 0.07 $\mu m^2/s$) were tracked under dimerising (**a**) and non-dimerising (**b**) conditions. Parameters for the simulation included probability of binding (0.5), binding interaction distance (25 nm), localization accuracy (15 nm) and QD blinking. (**a**) Left: Schematic showing the displacement vectors of two receptors that form a transient (up to 200 ms) dimer and undergo correlated motion. Right: Analysis of simulations of transient dimer formation. Note the pronounced decrease in the uncorrelated jump distance as diffusing particles approach each other to within the interaction distance. (**b**) Left: Schematic depicting the displacement vectors of two particles that maintain proximity due to confinement in a region (black square) but do not show correlated motion. Right: Analysis of simulations under the same conditions as **a**, except that the probability of binding was set to zero. Note that the uncorrelated jump distance does not vary significantly as a function of separation distance. Thus, even when these particles are close enough to show emission overlap, the analysis shows that their motion is not correlated. Given that the mechanism of decreased diffusion rate upon oligomerization is poorly characterized in live cells, we did not attempt to include this phenomenon in our simulations and therefore the jump magnitude does not vary in these analyses.

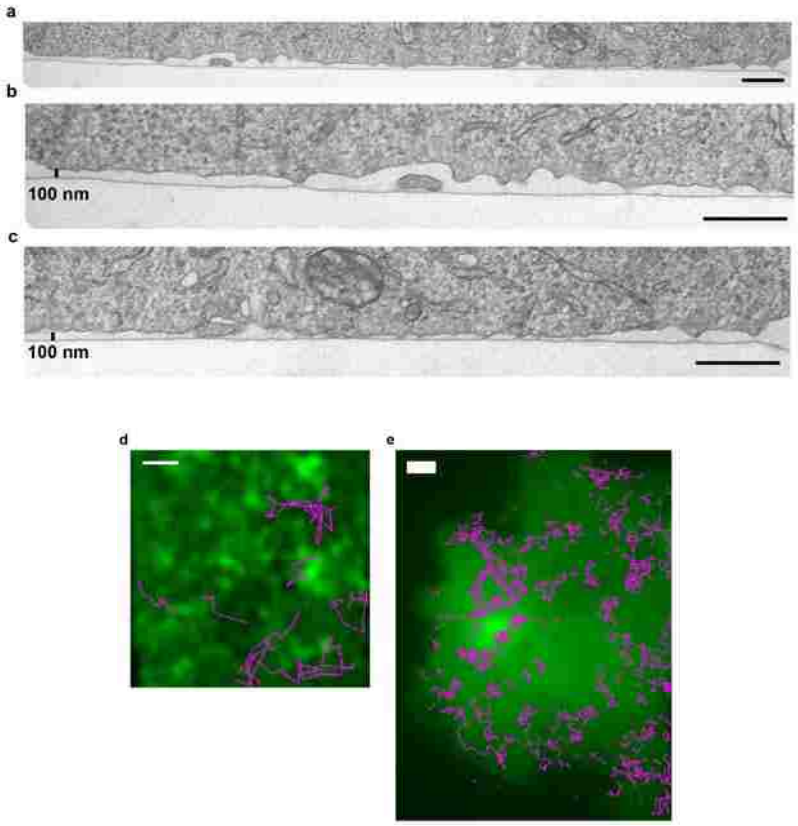

Figure S2.5 Membrane-coverslip distance does not dictate QD-IgE-FcεRI diffusion. (**a-c**) TEM image of an adherent RBL-2H3 cell taken perpendicular to the plane of adhesion (see Supplementary Methods). Images in **b** and **c** are the left and right half, respectively, of the region depicted in **a**. (**d**) TIRF image of GFP-actin (green) overlayed with trajectories of *free* QDs diffusing under the cell (magenta). (**e**) TIRF image of cytoplasmic GFP (green) overlayed with QD655-IgE-FcεRI trajectories (magenta) (see Supplementary Methods). Even regions closest to the coverslip (brightest GFP signal) do not exclude QD-IgE-FcεRI. Also note the highly disimilar patterns of GFP fluorescence in **d** and **e**; indicating that GFP-actin intensity does not correlate with membrane-coverslip distance as measured by cytoplasmic GFP intensity. (**f-q**) TIRF images of adherent, RBL-2H3 cells expressing GFP-actin (**f**, **g**, **j**, **k**, **n**, and **o**) or cytoplasmic GFP (**h**, **i**, **l**, **m**, **p**, and **q)** in the presence of a soluble, extracellular dye. First and third columns show images of GFP-actin (**f**, **j**, and **n**) and cytoplasmic GFP (**h**, **l**, and **p**) signal, respectively. Second and fourth columns (**g**, **i**, **k**, **m**, **o**, and **q**) show signal from a soluble fluorophore which diffuses underneath the cells and is brighter in regions where there is more space between the coverslip and cell membrane and dimmer in regions of close contact. Images are a mean of 50 time frames. A cell mask was generated from the GFP image and applied to **f-i** to remove the high background dye fluorescence surrounding the cell. Note that the large (~300kD) fluorophore has access to nearly all of the area underneath the cell. Selected GFP-actin structures (**f**, **j**, and **n**) or regions of cytoplasmic GFP intensity (**l-q**) are outlined in white and superimposed on both the GFP image and the image of the soluble fluorophore to facilitate comparisons between the two images. All images have been background subtracted. (**r-w**) Confocal images of fixed RBL-2H3 cells expressing GFP-actin enabling comparison of GFP-actin fluorescence (**r**, **u**, and green in **t** and **w**) with β3 or VLA4 (α4) integrin staining (**s**, **v**, and magenta in **t** and **w**) at the adherent surface. Confocal slice thickness is 1 μm. Images have been Gaussian filtered. Scale bars represent 1 μm in **a-d** and **r-w**, 2 μm in **e**, and **j-q** and 5 μm in **f-i**.

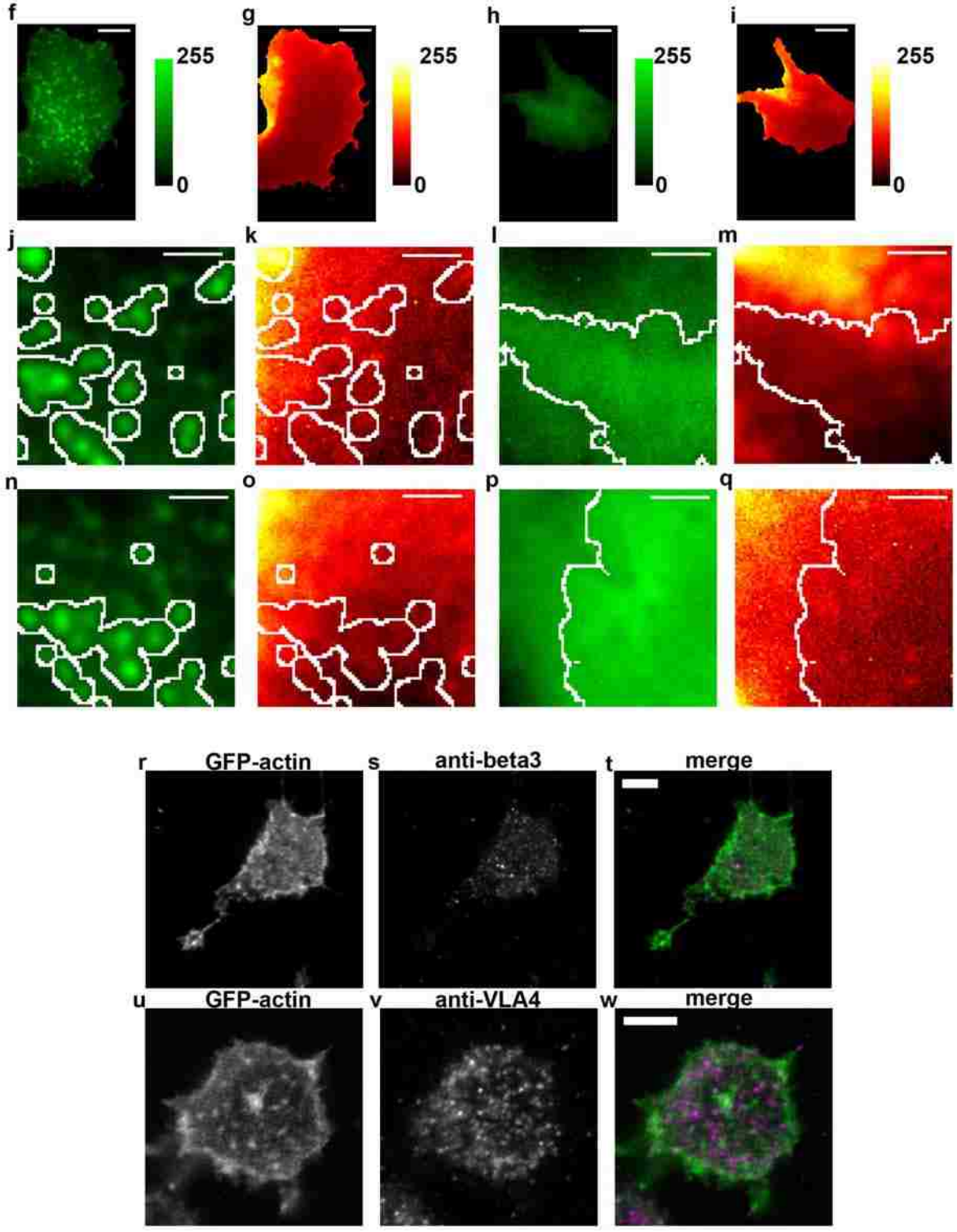

Figure S2.5 continued

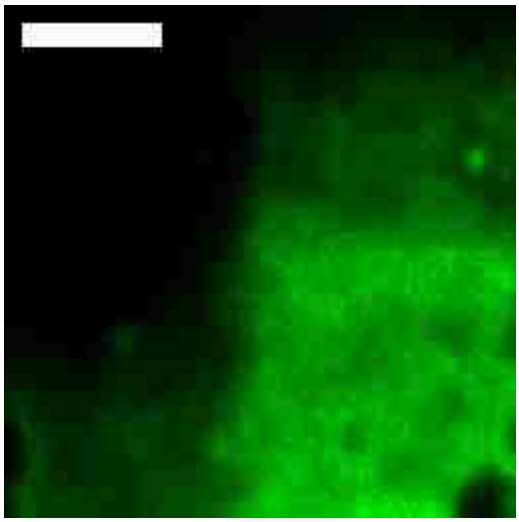

Figure S2.6 GFP-actin structure is visibly disrupted by latrunculin treatment. Deconvolved TIRF image of an RBL GFP-actin cell after 10 minute incubation with 500 nM latrunculin B. Note that less structure is apparent than in untreated cells (Figure S2.5a; Figure 4c in main text, and Supplementary Video 2. 4). Scale bar represents 2 μm.

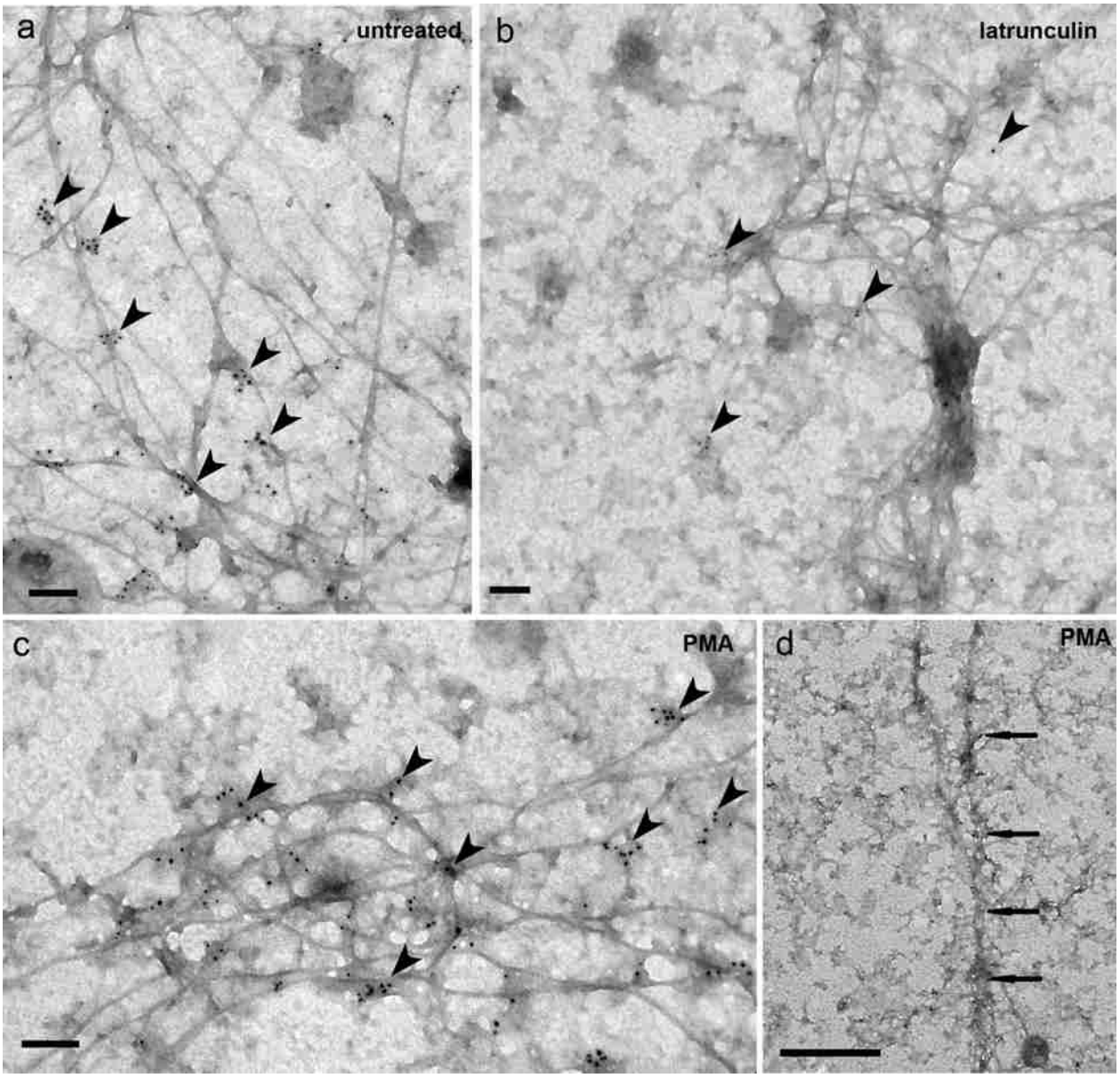

Figure S2.7 Electron microscopy of membrane sheets. Membrane sheets from the adherent surface of RBL cells (prepared as in reference (Pfeiffer and Oliver 1994) with the exception that cells were grown on EM grids) expressing GFP-actin. Gold particles label GFP-actin (arrowheads in **a-c**), which is located primarily at cytoskeletal junctions in the untreated (**a**) and PMA treated (50 nM for 30 min) (**c, d**) cells. This pattern is consistent with earlier observations(Wilson, Pfeiffer et al. 2001). Large actin bundles (arrows in **d**) likely correspond to GFP-actin structures visible by fluorescence micrsoscopy. After treatment with latrunculin B (10 µg/ml for 60 min), GFP labeling is dramatically decreased (indicating a disruption of the actin filaments), but cable-like structures are still present (presumably composed of an intermediate filament protein) (**b**). Scale bars represent 100 nm in **a-c** and 500 nm in **d**.

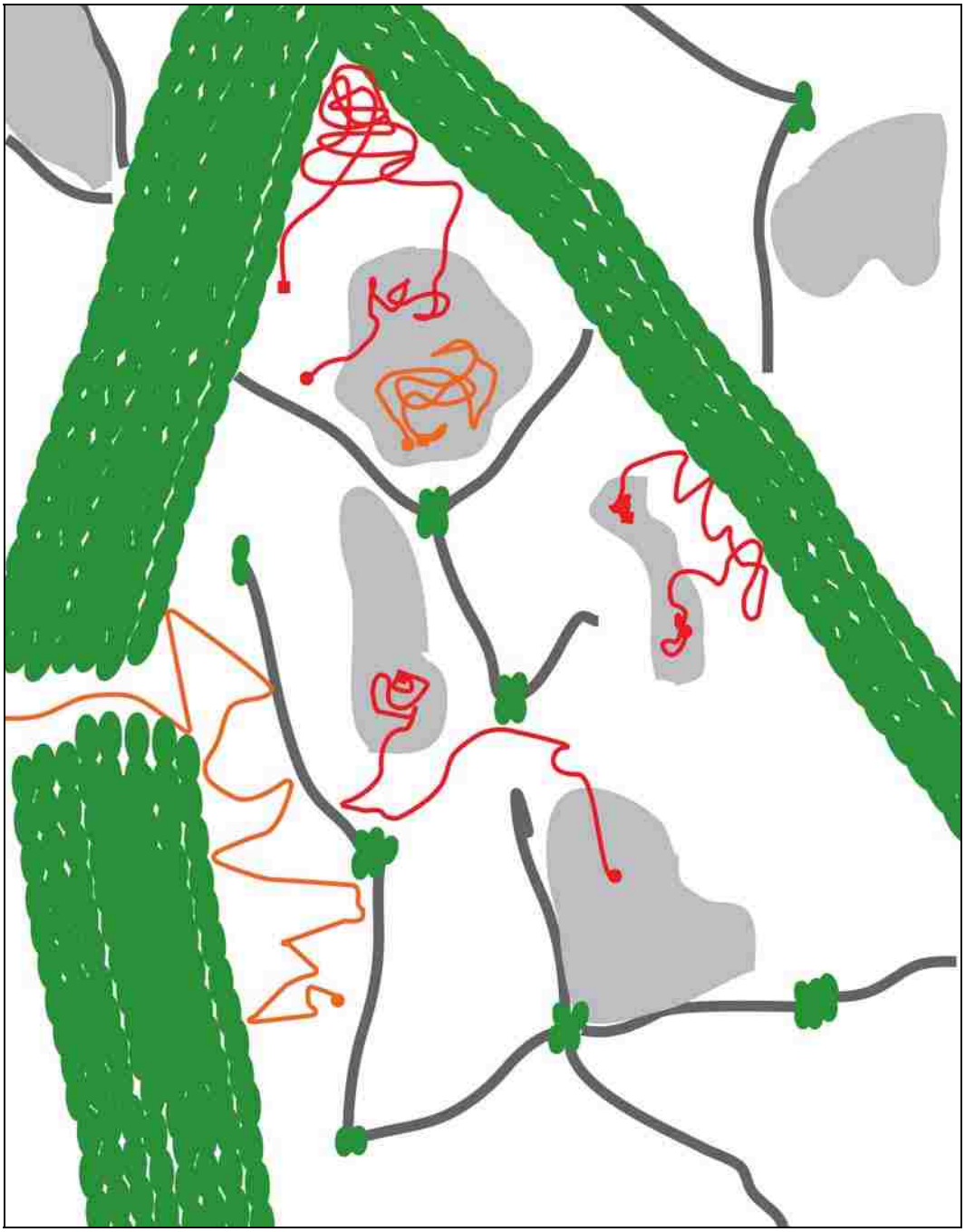

Figure S2.8 Cartoon model of receptor movement through the membrane architecture. Large actin bundles (green filaments), as observed in fluorescence microscopy, partition the membrane into large, micron-sized regions. Within this larger structure is a fine meshwork of cytoskeleton composed of intermediate filaments (dark grey) with actin at the junctions (as seen in EM) that form nano-scale domains. Additionally, membrane rafts (lipid rafts/protein islands, light grey) form specialized domains. Sample receptor trajectories (red, orange) are overlayed on this landscape, to demonstrate ways that these various components can restrict diffusion. Though a single snapshot of the membrane landscape is depicted here, in reality it is dynamically changing.

A.2 Supplementary Video Legends

Video 2.1 RBL-2H3 cell activation through QD-IgE. RBL-2H3 cell stably expressing FcεRIγ-mCFP (left panel), primed with 1 nM QD-IgE (middle panel) and stimulated with 14 nM DNP-BSA. Receptor aggregation and internalization are readily apparent in the fluorescence channels, and cell ruffling and spreading can be seen in the DIC image (right panel). Images acquired at 37°C at 2 frames/min; playback is 5 frames/s. Fluorescence channels have been Gaussian filtered. Scale bar represents 10 μm.

Video 2.2 Co-confinement of multiple QD-IgE-FcεRI. RBL-2H3 cell labelled with 100pM QD655-IgE for 10 min at 37°C. Images acquired at 35°C at 33 frames/s, playback is 33 frames/s. Scale bar represents 5 μm.

Video 2.3 RBL-2H3 cells were transfected with GFP-actin, labelled with QD655-IgE and treated with PMA. Images of the two spectral channels were collected simultaneously on the same CCD camera at 33 frames/s and the two channels were made coincident by shifting the GFP-actin channel (green) using a Fourier based shift algorithm. SPT was performed on the QD-IgE images as described in the text. A small ~ 4x4 micron area centered on the region containing a QD-IgE trajectory was selected for further processing. The "green" channel containing the GFP-actin signal was de-noised and deconvolved as described. For improved visual clarity, the found positions of the tracked QD-IgE were used to generate a 2D Gaussian representation of the particle (magenta) and

were combined as a color overlay with the actin time series to generate a two-color movie. Playback is 10 frames/s. Scale bar represents 1 micron.

Video 2.4 Restricted receptor diffusion on untreated RBL-GFP-actin cells. Same image processing details as in Video 2.3. Playback is 10 frames/s. Scale bar represents 1 micron.

Video 2.5 As described in the text, a 100 frame time series image was collected by imaging the top of the cell with a Zeiss 510 confocal microscope. RBL-2H3 cells were transected with GFP-actin (green) and labelled with QD-IgE (magenta) and were otherwise untreated. Emission was collected with a 545 nm dichroic mirror splitting emission to a 505 LP emission filter for GFP and the META detector was used as a bandpass filter (625-689 nm) to collect QD655 emission. Images were taken with 2× averaging, giving a final rate of 1 frame/s. Each frame of the GFP-actin image was de-noised using a wavelet based filter as described for the initial de-noise step in(Rooms, Philips et al. 2005). SPT was performed on the QD-IgE images as described in the text. For improved visual clarity, the found positions of the tracked QD-IgE were used to generate a 2D Gaussian representation of the particle (magenta) and were combined as a color overlay with the actin time series to generate a two-color movie. Playback is 10 frames/s. Scale bar represents 5 μm.

A.3 Supplementary Methods

A.3.1 EM analysis of QD-IgE valency

Solutions of 1nM QD-IgE or QD were prepared in PBS, 1% BSA and incubated on EM grids (formvar and carbon coated, then glow-discharged) for 15 min at room temperature. Grids were rinsed with PBS, then incubated with DNP-BSA-5nM gold (in PBS, 1% BSA) for 30 min at room temperature, followed by a PBS wash and fixation with 2% glutaraldehyde. Electron micrographs were acquired using a transmission electron microscope (Hitachi H600). From these images, we calculated averages of 1.3 and 6.5 DNP-BSA-gold particles per μm^2 for QD only (43.5 μm^2 total area) and QD-IgE (12.8 μm^2 total area) samples, respectively; indicating 20% non-specific binding of the DNP-BSA-gold probe. The average distances between each gold particle and the nearest QD were 92.7 and 51.4 nm for QD (n=57 gold particles) and QD-IgE (n=83 gold particles) samples, respectively.

A.3.2 TIRF controls

To ensure that interactions with the coverslip were not dictating QD-IgE-FcεRI motion, we performed several control experiments. We monitored diffusion of unbound streptavidin QD underneath GFP-actin cells (Fig. S2.6a), acquired cross-sectional EM images of adherent RBL-2H3 cells (Fig. S2.5), tracked QD-IgE-FcεRI complexes on the top (non-adherent) surface of RBL GFP-actin cells using confocal microscopy (Fig. 2.4 in main text) and on the bottom of RBL-GFP cells using TIRF microscopy (Fig. S2.6b), imaged RBL-GFPactin and RBL-GFP cells in the presence of soluble fluorophore (Fig. S2.7 and S2.8, respectively) using TIRF microscopy, and acquired confocal images of the

adherent surface of fixed GFP-actin cells stained for the α4 and β3 integrins (Fig. S2.9). All of these experiments indicate that there is enough room for diffusion of the QD-IgE-FcεRI complex on the adherent cell surface and that the observed restriction of diffusion by actin structures is not merely a result of streic limitations due to membrane-coverslip proximity.

A.3.2.1 Free QD diffusion. SPT conditions were the same as for QD-IgE-FcεRI, except that unlabelled QDs that diffused between the cell and coverslip were tracked.

A.3.2.2 EM sections. Cells were grown as monolayers on plastic tissue culture dishes, and fixed with 2% glutaraldehyde in 0.1 M sodium cacodylate buffer. Cells were embedded in EPON and allowed to harden. The EPON-embedded cells were separated from the plastic surface and then mounted perpendicular to the plane of adhesion for sectioning. Sections were then processed and imaged as described previously(Pfeiffer, Seagrave et al. 1985).

A.3.2.3 RBL-GFP cells. RBL-GFP cells provided a means to visualize the topography of the adherent cell surface. Regions of the cell closer to the coverslip would have a larger volume within the TIRF field and therefore appear brighter, whereas regions further from the coverslip would have less volume within the TIRF field and appear dimmer. These cells were then labelled with 1 nM QD655-IgE and the QDs were tracked at 10 frames per second while simultaneously acquiring the cytoplasmic GFP signal.

A.3.2.4 Free dye. RBL-GFPactin or RBL-GFP cells were imaged at 5 frames/s in the presence of 20 nM Alexa Fluor® 647-R-phycoerythrin streptavidin (Invitrogen,

Carlsbad, CA) in the imaging buffer. Regions of close contact between the cell and the coverslip exclude more of the soluble fluorophore and therefore have less fluorescence compared to regions which were further from the coverslip. By simultaneously acquiring the GFP-actin signal and the soluble fluorophore signal, we could compare the distribution of GFP-actin with the distance between the membrane and the coverslip.

A.3.2.5 Integrin staining. RBL-2H3 cells expressing GFP-actin were grown on 15 mm round glass coverslips and fixed with 2% paraformaldehyde for 20 minutes at room temperature. Cells were then permeabilized by 10 minute incubation in 1% Triton and stained with anti-VLA4 (anti-α4; Endogen, Boston, MA) or anti-β3 (H-96; Santa Cruz Biotchnology, Inc., Santa Cruz, CA) primary antibodies, followed by incubation with Alexa555-conjugated secondary antibodies (Alexa Fluor® 555 $F(ab')_2$ fragment of goat anti-mouse IgG (Invitrogen, Carlsbad, CA) for anti-VLA4 and Alexa Fluor® 555 donkey anti-rabbit IgG (Invitrogen, Carlsbad, CA) for anti-β3). Coverslips were then mounted in ProLong Gold® anti-fade reagent (Invitrogen, Carlsbad, CA) and imaged on a Zeiss LSM510 META confocal imaging system.

A.3.3 Gene constructs and transfection

The γ subunit of human FcεRI (Accession number NM 004106; GI 4758343) was initially cloned into the EcoRI/SalI site of pCMV6-XL5 (OriGene, Rockville, MD), followed by restriction digest-mediated transfer, in frame with mCFP, into pEF-DEST51 expression vector (Invitrogen, Carlsbad, CA). The pmaxGFP vector was supplied as part of the Cell Line Nucleofector Kit L (Amaxa, Gaithersburg, MD). Transfection was accomplished by introduction of the vector into early passage RBL-2H3 cells using the

Amaxa Nucleofector II with Solution L and Program T-20 (Amaxa, Gaithersburg, MD). RBL-2H3 cells transiently transfected with pmaxGFP were imaged within 24 hours. Cells stably transfected with pEF-FcεRIγ-mCFP were selected with 2.5 μg/ml Blasticidin (Invitrogen, Carlsbad, CA), followed by fluorescence associated cell sorting (FACS) for CFP emission.

A.3.4 Image Registration

For two color imaging, fluorescence was separated into two spectrally distinct images by a dual color image splitter (OptoSplit II, Cairn Research, UK), which were captured simultaneously and side-by-side on a single CCD camera (iXon 897 or Luca, Andor UK). The spectral windows of the captured images were defined by a dichroic filter and two emission filters in the image splitter (565DXCR, D510/40m, D655/40m, respectively, Chroma, Rockingham, VT). The relative translation of one image with respect to the other on the CCD camera was calibrated by imaging multi–fluorophore fluorescent beads (0.2 μm Tetraspeck, Invitrogen, Carlsbad, CA) that have an emission spectrum covering the two spectral windows. The translation vector was found using an iterative cross-correlation routine providing sub-pixel accuracy(Pham, Bezuijen et al. 2005). The quality of the alignment (merging) of the two images was limited only by small aberrations present in one or both of the channels that lead to a typical 10 nm error towards the center of the image (where the alignment routine was biased) to a 30 nm error towards the edges of the images.

A.3.5 Image Processing

All data analysis and image processing was performed within the MATLAB (The Mathworks Inc.) environment, including the DIPImage(Luengo Hendriks, Rieger et al. 1999) image processing library. Single particle tracking algorithms were coded in the c language and called from within MATLAB through a mex interface. For essential speed optimization (~20 X speedup over a MATLAB implementation), the Richardson-Lucy deconvolution code was written using the CUDA toolkit(NVIDIA 2007) (NVIDIA, Santa Clara, CA) to allow calculation using a graphics processing unit (NVIDIA 8800 GTS), and was called from within the MATLAB environment through a mex interface. Confocal images were de-noised using a two dimensional wavelet based filter(Sendur and Selesnick 2002; Rooms, Philips et al. 2005).

A.3.6 Single Particle Tracking

Single particle trajectories were determined from the raw data sets using a three step process: (1) identification of areas of interest; (2) Gaussian fitting; (3) building trajectories from coordinates. This approach is similar to those described previously(Dahan, Levi et al. 2003; Bonneau, Dahan et al. 2005; Arndt-Jovin, Lopez-Quintela et al. 2006; Hagen, Lidke et al. In Press).

A.3.6.1. Identification of areas of interest. Each 2D image from a 3D data set was processed independently to find QD coordinates. Areas of interest were contiguous regions of pixels that met two criteria: (a) pixels had intensities greater than three times the standard deviation of pixel intensities from areas defined as background (backgroundoffset algorithm, (Luengo Hendriks, Rieger et al. 1999)) and (b) pixels were above a threshold, (threshold, (Luengo Hendriks, Rieger et al. 1999)). Afterwards, a high

pass filtering of the image was performed by subtracting from the image a 2D Gaussian filter with σ= 5. The result is a binary image of pixels that passed both criteria.

A.3.6.2. Gaussian fitting. The center of mass of each contiguous region in the binary image was used as a starting point in a Gaussian fitting routine. The raw 2D images were used being offset to zero. The highest intensity pixel in a small region around the starting point (typically 5 pixels square) was used as an updated starting point to the iterative "Gaussian mask"(Thompson, Larson et al. 2002) fitting routine. Fits were performed in a square region, of size ~ 2 x σ_{psf}, around the updated starting point, where σ_{psf} defines the size of 2D Gaussian approximation to the point spread function. After convergence of the fitting routine, defined as a change in location of less than 10^{-5} pixels, a normalized cross-correlation was calculated using the data and a 2D Gaussian with center given by the result of the fit. The found coordinates were only considered as positions of QDs and used in further analysis if they exceeded a cross-correlation value of 0.7.

A.3.6.3. Building trajectories from coordinates. The probability of finding a diffusing particle in two dimensions at a distance greater than r from its starting point after a time Δt is given by(Saxton 1993)

$$P(r,\Delta t)=\exp[\, -r^2/(4D\Delta t)\,] \qquad \text{eq. 1}$$

Trajectories were built from the set of 3D coordinates in two steps. First, coordinates identified at time t were compared with coordinates at time $t+\Delta t$ using eq. 1 where Δt is the inverse frame rate of data acquisition. If $P(r,\Delta t)$ was found to be greater than .05, the coordinate at $t+\Delta t$ is associated with the coordinate at t in a trajectory. This process

builds short,un-interrupted trajectories. Due to the blinking of QDs, temporally separated trajectories may correspond to the movement of the same QD. The end coordinate of all trajectories are compared with all later starting coordinates of other trajectories using eq. 1, where Δt is now the time interval between the end of the first trajectory and the beginning of the second. The later trajectory with the smallest Δt that has a $P(r,\Delta t)>.01$ is connected with the first trajectory. This process is continued until there are no remaining pairs of trajectories that satisfy the criteria. If a trajectory contains more than four coordinates, a diffusion coefficient is estimated from the trajectory as

$$D_{est}=MSD(\Delta t) / 4\Delta t \qquad \text{eq. 2.}$$

where *MSD* is the mean square displacement and Δt is the inverse frame rate. The diffusion coefficient, D, used in eq. 1 is then the mean diffusion coefficient from the two trajectories. If the diffusion coefficient of the two trajectories varies by more than a factor of ten, trajectories are not combined.

A.3.7 Short range interaction analyses

RBL-2H3 cells were labeled with 200 pM each QD655-IgE and QD585-IgE for 10 min at 37°C. TIRF imaging was performed on these cells at 100 frames/s at 35°C and the resulting QD-IgE-FcεRI time series were then tracked as described (see Supplementary Methods, Single Particle Tracking section) to generate sets of trajectories for each color QD. All trajectories from one color of QD were compared with all trajectories of the other color. If QDs of different color were within a cutoff distance (500 nm) in the same time frame, a set of parameters was calculated based on the found positions of the QDs in the next time frame. All calculated parameters were recorded as a function of initial

separation. Uncorrelated jump distance and jump magnitude were calculated to determine if coordinated movement or transient dimerization existed between the tracked QD-IgE-FcεRI complexes. These parameters were averaged over all frames and QD pairs into 50 nm separation bins and then plotted, with the error given as the standard error of the mean in each bin. The degree of correlation between the motions of two particles was obtained by determing the amount of uncorrelated motion between two nearby particles: $D_i = |\mathbf{J}_i - \mathbf{J}_i(\mathbf{J}_i \cdot \mathbf{J}_j)/(|\mathbf{J}_j||\mathbf{J}_i|)|$, where $\boldsymbol{J1}_i = \boldsymbol{r1}_{i+1} - \boldsymbol{r1}_i$, $\boldsymbol{J2}_i = \boldsymbol{r2}_{i+1} - \boldsymbol{r2}_i$, and $\boldsymbol{r}_i$ is the position of a particle in frame *i*. The magnitude of single time step displacements, $|\boldsymbol{J}_i|$, was calculated in a similar manner. Parameters without a particle index (1,2) are calculated for both QDs.

A.3.8 Deconvolution

Deconvolution of time series images involved several steps. First, the pixel regions in each three dimensional data stack that corresponded to actin regions were cropped to form smaller three dimensional data sets and filtered in the time dimension with a Gaussian filter with $\sigma = 10$ frames (0.3 seconds). For manageable processing of several hundred data sets, each data set containing 2,000 images, only 1 of 10 time filtered images were deconvolved, starting with frame 5 and ending with frame 1,995. These 200 images first had a pixel-wise camera offset subtracted from them and then were independently de-noised using a two dimensional wavelet based filter(Sendur and Selesnick 2002; Rooms, Philips et al. 2005). To prevent edge related artifacts during deconvolution, each image was mirrored along each edge by 16 pixels that were then multiplied by a cosine function that went to zero at the outermost pixel. A two dimensional Gaussian was used to represent the microscope point spread function (PSF).

The width of the PSF was determined by a fit to a high signal to noise image of a 100 nm bead (Tetraspeck, Invitrogen, Carlsbad, CA). Two hundred iterations of a Richardson-Lucy deconvolution(Richards.Wh 1972; Lucy 1974) were performed on each image with an entropy regularization(de Monvel, Le Calvez et al. 2001) after each iteration with regularization parameter of 0.05. After deconvolution, images were cropped to their original size.

A.3.9 Binary Segmentation of Actin Structures

The deconvolved time series images were used for actin segmentation. Each image was filtered, and segmented using a four step process. First, a top hat filter (DIPImage function 'tophat') selects regions that are above a local minimum. Second, the top hat filtered image is eroded using grey scale erosion (DIPImage 'erosion') to better define the brightest regions. Third, the image is locally contrast stretched by dividing each pixel by the maximum value found in a 10 pixel (0.67 micron) radius around each pixel. Finally, the resulting image is thresholded (DIPImage function 'threshold') to create a binary image representing the location of actin structures.

A.3.10 Actin Trajectory Overlap

Coordinates found from single particle tracking were used to build binary trajectory images that were compared with actin structures. If a coordinate was valid (QD has not 'blinked' off) in both a time frame t and the next time frame at t+1, a binary image was created of this single time frame jump by drawing a pixelized line from the starting point to the end point. The linear pixel size used is the back-projected pixel size of the collected CCD images, which was 67 nm. For all valid single frame jumps in each

trajectory found by single particle tracking, the total length of the linearized trajectory, as well as the number of pixels in the trajectory that overlapped with the binary actin image at time *t* were recorded. For each trajectory, the same calculation was made using 10 simulated particles that had the same starting coordinate, diffusion coefficient, trajectory length, and blinking behavior as that of the single particle trajectory, but were otherwise unrestricted.

To test if the found trajectories had behavior with respect to actin that was significantly different from the unrestricted, simulated particles with the same diffusion coefficient, we treated the system using a binomial model as follows. Within groupings for each cell treatment, all trajectories were combined to give a total trajectory length *n*, and a total actin overlap *k*. The simulated particle trajectories were used to define a probability for overlap *p* for the unrestricted case. We make the simplification that all pixels in a trajectory can be treated independently with respect to actin overlap in order to use the well defined binomial model. The cumulative distribution function of the binomial distribution is $F(k;n,p)=I_{1-p}(n-k,k+1)$ where *I* is the regularized incomplete beta function. *F* gives the probability that a randomly generated data set created from the binomial model with parameters *n* and *p* would have a value less than or equal to *k*. We reject the hypothesis that our trajectories can be modeled with unrestricted diffusion with respect to actin when *F* is less than .01. In all three cases, $F<<<0.01$, with $F = 2.35\text{x}10^{-286}$, $2.35\text{x}10^{-264}$ and $2.42\text{x}10^{-154}$ in the resting, latrunculin-treated, and PMA-treated cells, respectively.

A.3.11 Diffusion in proximity to actin

A pixelated distance map to the nearest actin structure was found by a distance transform (DIPImage function 'dt') of the inverse of the binary images created by the binary segmentation of the actin images. The mean square jump distance of single time step jumps was recorded as function of distance from actin for all SPT trajectories in cells treated with PMA.

An offset term was calculated by fitting individual particle trajectories to Eq.(1) using the first 3 data points of the MSD. This value is equivalent to the first point of a calculated MSD plot and can be related to the diffusion coefficient.

The mean observed jump size over some time interval of a freely diffusing particle (and thereby calculated diffusion coefficient) will appear to be reduced near a reflecting boundary due to the particle's inability to make large jumps in the direction of the boundary (Ritchie, Shan et al. 2005). In order to estimate the magnitude of this effect, simulations of a diffusing particle near a reflecting half space boundary were performed using the pixel size and frame rate of the experiment with parameters that correspond to the median experimentally observed $D_{1\text{-}3}$ diffusion coefficient found as described above. To represent detector time averaging, 10 sub-frames at 10 times the frame rate were added together to form one simulated observed frame. If a particle's position after a jump in one of the sub-frames was beyond the reflecting boundary (x = 0), its x-coordinate was multiplied by -1 and the next frame was calculated as a jump from the corrected position. The resulting time series were analysed with the same routines used for experimental data.

APPENDIX B: SUPPLEMENTARY INFORMATION FOR CHAPTER 3

APPENDIX B. SUPPLEMENTARY INFORMATION FOR CHAPTER 3

B.1 Supplementary Figures for Chapter 3

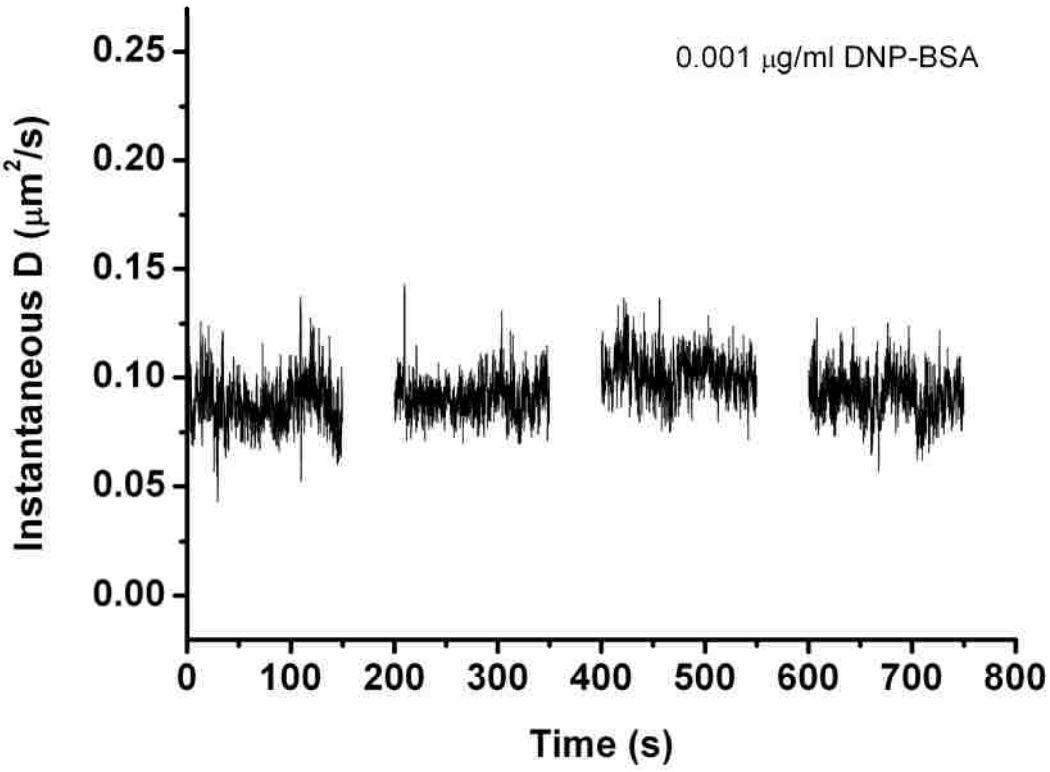

Figure S3.1 Instantaneous diffusion coefficient as a function of time for a single cell after treatment with 0.001 μg/ml DNP-BSA. Experiment conducted as described in main text (Methods, Kinetics of Immobilization Assay section), but in this case multiple time series were acquired sequentially from a single cell after stimulation with 0.001 μg/ml DNP-BSA. Gaps in data are due to finite memory limitations on the length of a single image series and represent the time required to save the previous image series and initiate the next. No changes in diffusion are apparent even after nearly 800 s of stimulation.

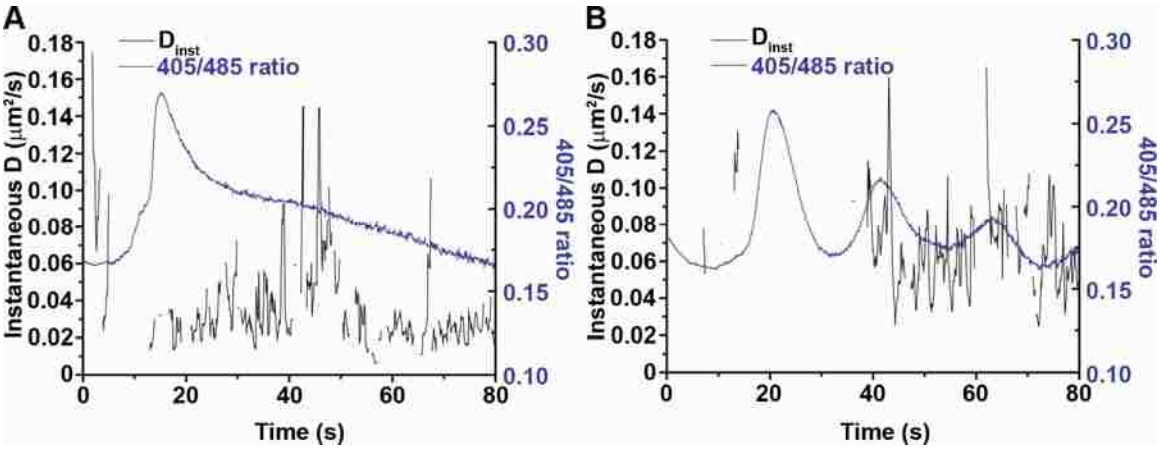

Figure S3.2 Simultaneous measurements of QD-IgE diffusion and Ca2+ responses. Cells were prepared and imaged as described in Appendix B, Supplementary Methods (below). Ten seconds into imaging, cells were stimulated with 10 μg/ml (A) or 0.001 μg/ml (B) DNP-BSA. Instantaneous diffusion coefficients (left axis, black lines) and the 405/485 emission ratio of the Ca^{2+} sensitive dye Indo-1 (right axis, blue lines) were calculated as a function of time. Note that 10 μg/ml DNP-BSA produces a rapid peak and then slow decline in the Ca^{2+} signal (A, blue line) and the instantaneous diffusion coefficient rapidly decreases to a minimum around 0.02 $\mu m^2/s$ (A, black line). In contrast, 0.001 μg/ml DNP-BSA induces Ca^{2+} oscillations (B, blue line) while the instantaneous diffusion coefficient remains largely unchanged at ~0.075 $\mu m^2/s$ (B, black line).

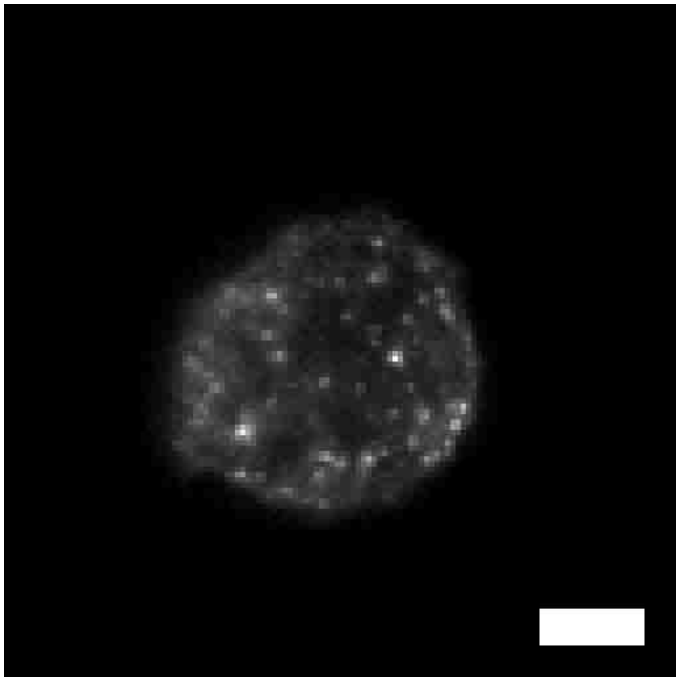

Figure S3.3 Antigen-induced clustering occurs in the absence of downstream signaling. RBL-2H3 cell primed with Alexa488-$IgE_{anti\text{-}dansyl}$, pre-incubated for 30 min with 10 μM PP2, and then stimulated with 1 μg/ml DNP-BSA for 5 min. Image is a sum-projection of a Z-series of wide-field images. Note the presence of clusters of Alexa488-IgEanti-dansyl. Scale bar represents 5 μm.

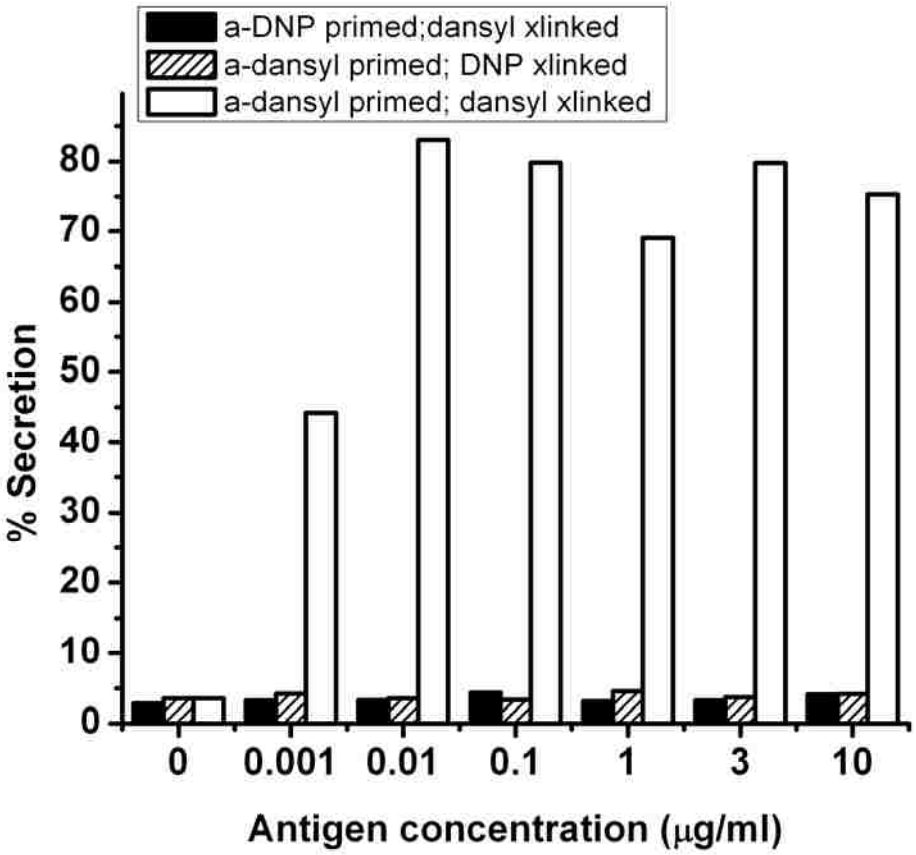

Figure S3.4 $IgE_{anti\text{-}dansyl}$ and $IgE_{anti\text{-}DNP}$ are specific for their designated antigens. RBL-2H3 cells were primed with either $IgE_{anti\text{-}DNP}$ or $IgE_{anti\text{-}dansyl}$ and then stimulated with the indicated doses of either DNP-BSA or dansyl-BSA. β-hexosaminidase was measured as described in main text (Methods, Degranulation assay section) and reported as % of total. No cross-reactivity was seen between $IgE_{anti\text{-}dansyl}$ and DNP-BSA or $IgE_{anti\text{-}DNP}$ and dansyl-BSA. Dansyl-BSA was able to elicit a secretory response from $IgE_{anti\text{-}dansyl}$ primed cells that was comparable to the response of $IgE_{anti\text{-}DNP}$ primed cells to DNP-BSA (main text, Figure 3.1B).

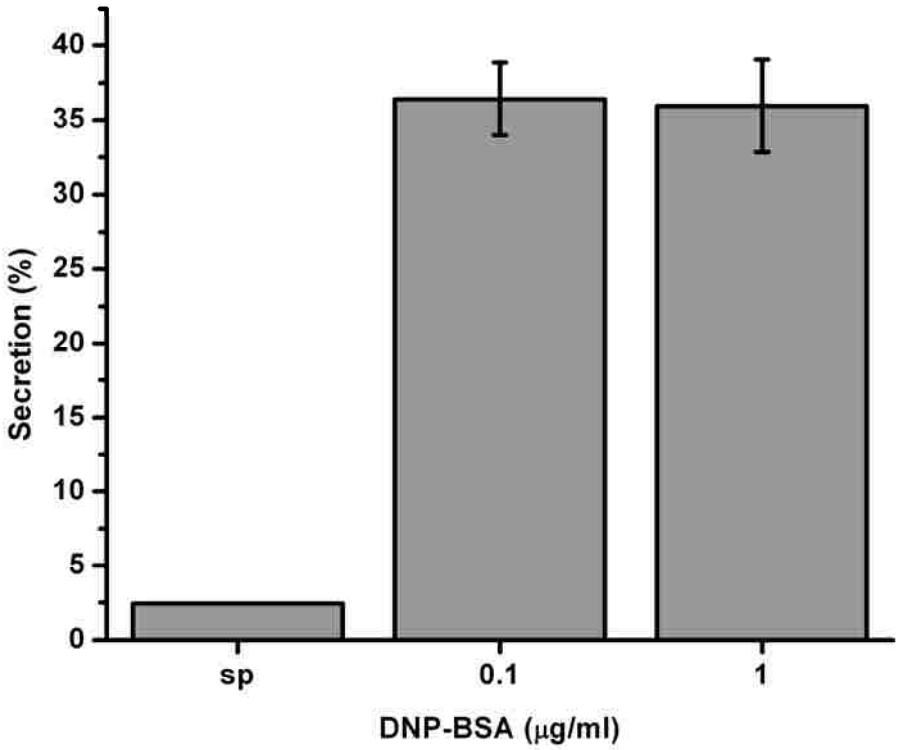

Figure S3.5 Degranulation occurs under the same conditions as the hyperspectral microscopy experiment. Cells primed by 15 min incubation with 2 nM QD-IgE at room temperature, washed, and then stimulated with the indicated doses of DNP-BSA. β-hexosaminidase release assay performed as described in main text (see Methods, Degranulation assay section). This shows that the highly mobile clusters of three QD-IgE-FcεRI complexes shown in the main text, Figure 3.5 are occurring under conditions which cause degranulation.

B.2 Supplementary Video Legend

Video 3.1 Non-crosslinked receptors do not significantly associate with cross-linked receptor aggregates. RBL-2H3 cells were labeled with SPT levels of QD655-IgEanti-DNP and then primed with Alexa488-IgEanti-dansyl. Cells were then exposed to 1 µg/ml dansyl-BSA and imaged at 20 frames/s by wide-field microscopy. Magenta is QD655-IgEanti-DNP, green is Alexa488-IgEanti-dansyl. Images have been gauss-filtered. Playback is 40 frames/s. Scale bar represents 5 µm.

B.3 Supplementary Methods for Chapter 2

B.3.1 Simultaneous Ca^{2+} Ratio Imaging and SPT

RBL-2H3 cells were labeled in an 8-well chamber with QD655-$IgE_{anti\text{-}DNP}$ as described in the main text, washed, and then incubated with 1 µM Indo-1 (Invitrogen, Carlsbad, CA) in MEM/FBS in the presence of 50 nM $IgE_{anti\text{-}DNP}$ for 20 min at RT under a 5% CO_2 atmosphere. Cells were then washed and 200 µl HBSS added to each well for imaging. Cells were then imaged at a rate of five frames/s using a mercury lamp with a 365/10 nm BP excitation filter. Emission was collected using a 380 nm dichroic mirror which sent light through a Quad-View image splitter (MAG Biosystems, Pleasanton, CA) equipped with 440 nm and 515 nm dichroic mirrors mounted in series, which reflected the emitted light through a 405/30 nm BP filter for the calcium bound state of Indo-1, a 485/25 nm BP filter for the calcium free state of Indo-1, and a 655/40 nm BP filter for QD655 emission. The three spectral channels were projected onto a 256x256 pixel region on the center of the CCD, enabling simultaneous collection. The channels collecting emission from the Ca^{2+}-free and Ca^{2+}-bound states of Indo-1 were background subtracted,

averaged, and ratioed, and single particle tracking analysis was performed on the QD655 emission channel as described previously (Andrews, 2008. *Nat Cell Biol*).

REFERENCES

REFERENCES

Andrews, N. L., K. A. Lidke, et al. (2008). "Actin restricts FcepsilonRI diffusion and facilitates antigen-induced receptor immobilization." Nat Cell Biol 10(8): 955-63.

Arndt-Jovin, D. J., M. A. Lopez-Quintela, et al. (2006). "In vivo cell imaging with semiconductor quantum dots and noble-metal nanodots." Proc. SPIE 6096: 60960P1-10.

Barisas, B. G., S. M. Smith, et al. (2007). "Compartmentalization of the Type I Fc epsilon receptor and MAFA on mast cell membranes." Biophys Chem 126(1-3): 209-17.

Boniface, J. J., J. D. Rabinowitz, et al. (1998). "Initiation of signal transduction through the T cell receptor requires the multivalent engagement of peptide/MHC ligands [corrected]." Immunity 9(4): 459-66.

Bonneau, S., M. Dahan, et al. (2005). "Single quantum dot tracking based on perceptual grouping using minimal paths in a spatiotemporal volume." Ieee Transactions on Image Processing 14(9): 1384-1395.

Born, M. and E. Wolf (1997). Principles of optics : electromagnetic theory of propagation, interference and diffraction of light. Cambridge, UK ; New York ;, Cambridge University Press.

Cheezum, M. K., W. F. Walker, et al. (2001). "Quantitative comparison of algorithms for tracking single fluorescent particles." Biophys J 81(4): 2378-88.

Dahan, M., S. Levi, et al. (2003). "Diffusion dynamics of glycine receptors revealed by single-quantum dot tracking." Science 302(5644): 442-445.

Dahl, S. C., R. W. Geib, et al. (1994). "Rapid capping in alpha-spectrin-deficient MEL cells from mice afflicted with hereditary hemolytic anemia." J Cell Biol 125(5): 1057-65.

Daumas, F., N. Destainville, et al. (2003). "Confined diffusion without fences of a g-protein-coupled receptor as revealed by single particle tracking." Biophys J 84(1): 356-66.

de Monvel, J. B., S. Le Calvez, et al. (2001). "Image restoration for confocal microscopy: Improving the limits of deconvolution, with application to the visualization of the mammalian hearing organ." Biophysical Journal 80(5): 2455-2470.

DeMond, A. L., K. D. Mossman, et al. (2008). "T cell receptor microcluster transport through molecular mazes reveals mechanism of translocation." Biophys J 94(8): 3286-92.

Destainville, N. and L. Salome (2006). "Quantification and correction of systematic errors due to detector time-averaging in single-molecule tracking experiments." Biophysical Journal 90(2): L17-L19.

Donnadieu, E., M. H. Jouvin, et al. (2003). "Competing functions encoded in the allergy-associated F(c)epsilonRIbeta gene." Immunity 18(5): 665-74.

Douglass, A. D. and R. D. Vale (2005). "Single-molecule microscopy reveals plasma membrane microdomains created by protein-protein networks that exclude or trap signaling molecules in T cells." Cell 121(6): 937-50.

Draber, P. and L. Draberova (2002). "Lipid rafts in mast cell signaling." Mol Immunol 38(16-18): 1247-52.

Dustin, M. L. and J. A. Cooper (2000). "The immunological synapse and the actin cytoskeleton: molecular hardware for T cell signaling." Nat Immunol 1(1): 23-9.

Dustin, M. L., M. W. Olszowy, et al. (1998). "A novel adaptor protein orchestrates receptor patterning and cytoskeletal polarity in T-cell contacts." Cell 94(5): 667-77.

Esa, A., P. Edelmann, et al. (2000). "Three-dimensional spectral precision distance microscopy of chromatin nanostructures after triple-colour DNA labelling: a study of the BCR region on chromosome 22 and the Philadelphia chromosome." J Microsc 199(Pt 2): 96-105.

Fattakhova, G., M. Masilamani, et al. (2006). "The high-affinity immunoglobulin-E receptor (FcepsilonRI) is endocytosed by an AP-2/clathrin-independent, dynamin-dependent mechanism." Traffic 7(6): 673-85.

Feder, T. J., I. Brust-Mascher, et al. (1996). "Constrained diffusion or immobile fraction on cell surfaces: a new interpretation." Biophys J 70(6): 2767-73.

Feder, T. J., E. Y. Chang, et al. (1994). "Disparate modulation of plasma membrane protein lateral mobility by various cell permeabilizing agents." J Cell Physiol 158(1): 7-16.

Frankel, D. J., J. R. Pfeiffer, et al. (2006). "Revealing the topography of cellular membrane domains by combined atomic force microscopy/fluorescence imaging." Biophys J 90(7): 2404-13.

Frigeri, L. and J. R. Apgar (1999). "The role of actin microfilaments in the down-regulation of the degranulation response in RBL-2H3 mast cells." J Immunol 162(4): 2243-50.

Garman, S. C., B. A. Wurzburg, et al. (2000). "Structure of the Fc fragment of human IgE bound to its high-affinity receptor Fc epsilonRI alpha." Nature 406(6793): 259-66.

Giepmans, B. N., T. J. Deerinck, et al. (2005). "Correlated light and electron microscopic imaging of multiple endogenous proteins using Quantum dots." Nat Methods 2(10): 743-9.

Gilfillan, A. M. and C. Tkaczyk (2006). "Integrated signalling pathways for mast-cell activation." Nat Rev Immunol 6(3): 218-30.

Goldsby, R. A., T. J. Kindt, et al. (2000). Kuby Immunology, Fourth Edition. New York, W. H. Freeman and Company.

Gould, H. J. and B. J. Sutton (2008). "IgE in allergy and asthma today." Nat Rev Immunol 8(3): 205-17.

Grakoui, A., S. K. Bromley, et al. (1999). "The immunological synapse: a molecular machine controlling T cell activation." Science 285(5425): 221-7.

Hagen, G. M., K. A. Lidke, et al. (In Press). Dynamics of membrane receptors: single molecule tracking of quantum dot liganded epidermal growth factor. Single Molecule Dynamics, Wiley Press.

Harms, G. S., L. Cognet, et al. (2001). "Autofluorescent proteins in single-molecule research: applications to live cell imaging microscopy." Biophys J 80(5): 2396-408.

Hartwig, J. H. and M. DeSisto (1991). "The cytoskeleton of the resting human blood platelet: structure of the membrane skeleton and its attachment to actin filaments." J Cell Biol 112(3): 407-25.

Irvine, D. J., M. A. Purbhoo, et al. (2002). "Direct observation of ligand recognition by T cells." Nature 419(6909): 845-9.

Jacobson, K., E. D. Sheets, et al. (1995). "Revisiting the fluid mosaic model of membranes." Science 268(5216): 1441-2.
Jacquier, V., M. Prummer, et al. (2006). "Visualizing odorant receptor trafficking in living cells down to the single-molecule level." Proc Natl Acad Sci U S A.
James, J. (1976). Light microscopic techniques in biology and medicine. The Hague, M. Nijhoff Medical Division.
Johansson, S. G., H. Oman, et al. (2006). "The importance of IgE antibody levels in anti-IgE treatment." Allergy 61(10): 1216-9.
Jonas, M., Y. Yao, et al. (2006). "Detecting single quantum dot motion with nanometer resolution for applications in cell biology." IEEE Trans Nanobioscience 5(4): 246-50.
Kaizuka, Y., A. D. Douglass, et al. (2007). "Mechanisms for segregating T cell receptor and adhesion molecules during immunological synapse formation in Jurkat T cells." Proc Natl Acad Sci U S A 104(51): 20296-301.
Kawakami, T. and J. Kitaura (2005). "Mast cell survival and activation by IgE in the absence of antigen: a consideration of the biologic mechanisms and relevance." J Immunol 175(7): 4167-73.
Kinet, J. P. (1999). "The high-affinity IgE receptor (Fc epsilon RI): from physiology to pathology." Annu Rev Immunol 17: 931-72.
Kinet, J. P., R. Quarto, et al. (1985). "Noncovalently and covalently bound lipid on the receptor for immunoglobulin E." Biochemistry 24(25): 7342-8.
Kitaura, J., J. Song, et al. (2003). "Evidence that IgE molecules mediate a spectrum of effects on mast cell survival and activation via aggregation of the FcepsilonRI." Proc Natl Acad Sci U S A 100(22): 12911-6.
Kraft, S. and J. P. Kinet (2007). "New developments in FcepsilonRI regulation, function and inhibition." Nat Rev Immunol 7(5): 365-78.
Kulczycki, A., Jr. and H. Metzger (1974). "The interaction of IgE with rat basophilic leukemia cells. II. Quantitative aspects of the binding reaction." J Exp Med 140(6): 1676-95.
Kusumi, A., H. Ike, et al. (2005). "Single-molecule tracking of membrane molecules: plasma membrane compartmentalization and dynamic assembly of raft-philic signaling molecules." Semin Immunol 17(1): 3-21.
Kusumi, A., C. Nakada, et al. (2005). "Paradigm shift of the plasma membrane concept from the two-dimensional continuum fluid to the partitioned fluid: high-speed single-molecule tracking of membrane molecules." Annu Rev Biophys Biomol Struct 34: 351-78.
Kusumi, A., Y. Sako, et al. (1993). "Confined Lateral Diffusion of Membrane-Receptors as Studied by Single-Particle Tracking (Nanovid Microscopy) - Effects of Calcium-Induced Differentiation in Cultured Epithelial-Cells." Biophysical Journal 65(5): 2021-2040.
Larson, D. R., J. A. Gosse, et al. (2005). "Temporally resolved interactions between antigen-stimulated IgE receptors and Lyn kinase on living cells." J Cell Biol 171(3): 527-36.
Letourneur, O., S. Sechi, et al. (1995). "Glycosylation of human truncated Fc epsilon RI alpha chain is necessary for efficient folding in the endoplasmic reticulum." J Biol Chem 270(14): 8249-56.

Lidke, D. S., N. L. Andrews, et al. (2007). "Exploring membrane protein dynamics by multicolor single quantum dot imaging using wide field, TIRF, and hyperspectral microscopy." Proceedings of SPIE 6448: 6448Y1-8.
Lidke, D. S., K. A. Lidke, et al. (2005). "Reaching out for signals: filopodia sense EGF and respond by directed retrograde transport of activated receptors." J Cell Biol 170(4): 619-26.
Lidke, D. S., P. Nagy, et al. (2004). "Quantum dot ligands provide new insights into erbB/HER receptor-mediated signal transduction." Nat Biotechnol 22(2): 198-203. Epub 2004 Jan 4.
Lillemeier, B. F., J. R. Pfeiffer, et al. (2006). "Plasma membrane-associated proteins are clustered into islands attached to the cytoskeleton." Proc Natl Acad Sci U S A 103(50): 18992-7.
Liu, F. T., J. W. Bohn, et al. (1980). "Monoclonal dinitrophenyl-specific murine IgE antibody: preparation, isolation, and characterization." J Immunol 124(6): 2728-37.
Lucy, L. B. (1974). "Iterative Technique for Rectification of Observed Distributions." Astronomical Journal 79(6): 745-754.
Luengo Hendriks, C. L., B. Rieger, et al. (1999). ""“DIPimage: A scientific image processing toolbox for MATLAB” Delft Univ. Technol., Delft, The Netherlands." Available: http://www.qi.tnw.tudelft.nl/DIPlib.
Mao, S. Y., N. Varin-Blank, et al. (1991). "Immobilization and internalization of mutated IgE receptors in transfected cells." J Immunol 146(3): 958-66.
Martin, D. S., M. B. Forstner, et al. (2002). "Apparent subdiffusion inherent to single particle tracking." Biophys J 83(4): 2109-17.
McCloskey, M. A., Z. Y. Liu, et al. (1984). "Lateral electromigration and diffusion of Fc epsilon receptors on rat basophilic leukemia cells: effects of IgE binding." J Cell Biol 99(3): 778-87.
Menon, A. K., D. Holowka, et al. (1984). "Small oligomers of immunoglobulin E (IgE) cause large-scale clustering of IgE receptors on the surface of rat basophilic leukemia cells." J Cell Biol 98(2): 577-83.
Menon, A. K., D. Holowka, et al. (1986). "Clustering, mobility, and triggering activity of small oligomers of immunoglobulin E on rat basophilic leukemia cells." J Cell Biol 102(2): 534-40.
Menon, A. K., D. Holowka, et al. (1986). "Cross-linking of receptor-bound IgE to aggregates larger than dimers leads to rapid immobilization." J Cell Biol 102(2): 541-50.
Miller, L., U. Blank, et al. (1989). "Expression of high-affinity binding of human immunoglobulin E by transfected cells." Science 244(4902): 334-7.
Morone, N., T. Fujiwara, et al. (2006). "Three-dimensional reconstruction of the membrane skeleton at the plasma membrane interface by electron tomography." J Cell Biol 174(6): 851-862.
Murase, K., T. Fujiwara, et al. (2004). "Ultrafine membrane compartments for molecular diffusion as revealed by single molecule techniques." Biophys J 86(6): 4075-93.
NVIDIA (2007). "Compute Unified Device Architecture (CUDA)." http://developer.nvidia.com/object/cuda.html.

Ortega, E., R. Schweitzer-Stenner, et al. (1988). "Possible orientational constraints determine secretory signals induced by aggregation of IgE receptors on mast cells." Embo J 7(13): 4101-9.
Paolini, R., M. H. Jouvin, et al. (1991). "Phosphorylation and dephosphorylation of the high-affinity receptor for immunoglobulin E immediately after receptor engagement and disengagement." Nature 353(6347): 855-8.
Pecht, I., E. Ortega, et al. (1991). "Rotational dynamics of the Fc epsilon receptor on mast cells monitored by specific monoclonal antibodies and IgE." Biochemistry 30(14): 3450-8.
Peters, R. and R. J. Cherry (1982). "Lateral and rotational diffusion of bacteriorhodopsin in lipid bilayers: experimental test of the Saffman-Delbruck equations." Proc Natl Acad Sci U S A 79(14): 4317-21.
Pfeiffer, J. R. and J. M. Oliver (1994). "Tyrosine Kinase-Dependent Assembly of Actin Plaques Linking Fc-Epsilon-R1 Cross-Linking to Increased Cell Substrate Adhesion in Rbl-2h3 Tumor Mast-Cells." Journal of Immunology 152(1): 270-279.
Pfeiffer, J. R., J. C. Seagrave, et al. (1985). "Membrane and Cytoskeletal Changes Associated with Ige-Mediated Serotonin Release from Rat Basophilic Leukemia-Cells." Journal of Cell Biology 101(6): 2145-2155.
Pham, T. Q., M. Bezuijen, et al. (2005). "Performance of optimal registration estimators." Proceedings of the SPIE - The International Society for Optical Engineering 5817(1): 133-144.
Pike, L. J. (2006). "Rafts defined: a report on the Keystone Symposium on Lipid Rafts and Cell Function." J Lipid Res 47(7): 1597-8.
Prussin, C. and D. D. Metcalfe (2003). "4. IgE, mast cells, basophils, and eosinophils." J Allergy Clin Immunol 111(2 Suppl): S486-94.
Pyenta, P., P. Schwille, et al. (2003). "Lateral diffusion of membrane lipid-anchored probes before and after aggregation of cell surface IgE-receptors." J Phys Chem A 107: 8310-8318.
Rahman, N. A., I. Pecht, et al. (1992). "Rotational dynamics of type I Fc epsilon receptors on individually-selected rat mast cells studied by polarized fluorescence depletion." Biophys J 61(2): 334-46.
Richards.Wh (1972). "Bayesian-Based Iterative Method of Image Restoration." Journal of the Optical Society of America 62(1): 55-&.
Ritchie, K., X. Y. Shan, et al. (2005). "Detection of non-Brownian diffusion in the cell membrane in single molecule tracking." Biophysical Journal 88(3): 2266-2277.
Rooms, F., W. Philips, et al. (2005). "Simultaneous degradation estimation and restoration of confocal images and performance evaluation by colocalization analysis." Journal of Microscopy-Oxford 218: 22-36.
Santini, F. and J. H. Keen (1996). "Endocytosis of activated receptors and clathrin-coated pit formation: deciphering the chicken or egg relationship." J Cell Biol 132(6): 1025-36.
Saxton, M. J. (1993). "Lateral Diffusion in an Archipelago - Single-Particle Diffusion." Biophysical Journal 64(6): 1766-1780.
Saxton, M. J. and K. Jacobson (1997). "Single-particle tracking: applications to membrane dynamics." Annu Rev Biophys Biomol Struct 26: 373-99.

Schlessinger, J., W. W. Webb, et al. (1976). "Lateral motion and valence of Fc receptors on rat peritoneal mast cells." Nature 264(5586): 550-2.
Seagrave, J., J. R. Pfeiffer, et al. (1991). "Relationship of IgE receptor topography to secretion in RBL-2H3 mast cells." J Cell Physiol 148(1): 139-51.
Sendur, L. and I. W. Selesnick (2002). "Bivariate shrinkage functions for wavelet-based denoising exploiting interscale dependency." Ieee Transactions on Signal Processing 50(11): 2744-2756.
Sigalov, A. B. (2004). "Multichain immune recognition receptor signaling: different players, same game?" Trends Immunol 25(11): 583-9.
Sinclair, M. B., D. M. Haaland, et al. (2006). "Hyperspectral confocal microscope." Appl Opt 45(24): 6283-91.
Singer, S. and G. Nicolson (1972). "The fluid mosaic model of the structure of cell membranes." Science 175(4023): 720-731.
Suzuki, K., K. Ritchie, et al. (2005). "Rapid hop diffusion of a G-protein-coupled receptor in the plasma membrane as revealed by single-molecule techniques." Biophys J 88(5): 3659-80.
Tang, Q. and M. Edidin (2003). "Lowering the barriers to random walks on the cell surface." Biophys J 84(1): 400-7.
Thomas, J. L., T. J. Feder, et al. (1992). "Effects of protein concentration on IgE receptor mobility in rat basophilic leukemia cell plasma membranes." Biophys J 61(5): 1402-12.
Thompson, R. E., D. R. Larson, et al. (2002). "Precise nanometer localization analysis for individual fluorescent probes." Biophysical Journal 82(5): 2775-2783.
Thyagarajan, R., N. Arunkumar, et al. (2003). "Polyvalent antigens stabilize B cell antigen receptor surface signaling microdomains." J Immunol 170(12): 6099-106.
Ueda, M., Y. Sako, et al. (2001). "Single-molecule analysis of chemotactic signaling in Dictyostelium cells." Science 294(5543): 864-7.
Varma, R., G. Campi, et al. (2006). "T cell receptor-proximal signals are sustained in peripheral microclusters and terminated in the central supramolecular activation cluster." Immunity 25(1): 117-27.
Vercelli, D. (2002). "The regulation of IgE synthesis." Clin Allergy Immunol 16: 179-96.
Verveer, P. J., F. S. Wouters, et al. (2000). "Quantitative imaging of lateral ErbB1 receptor signal propagation in the plasma membrane." Science 290(5496): 1567-70.
Viola, A. and N. Gupta (2007). "Tether and trap: regulation of membrane-raft dynamics by actin-binding proteins." Nat Rev Immunol 7(11): 889-96.
Wilson, B. S., J. R. Pfeiffer, et al. (2000). "Observing FcepsilonRI signaling from the inside of the mast cell membrane." J Cell Biol 149(5): 1131-42.
Wilson, B. S., J. R. Pfeiffer, et al. (2001). "High resolution mapping of mast cell membranes reveals primary and secondary domains of Fc epsilon RI and LAT." Journal of Cell Biology 154(3): 645-658.
Xu, Y., K. W. Harder, et al. (2005). "Lyn tyrosine kinase: accentuating the positive and the negative." Immunity 22(1): 9-18.
Yamaguchi, M., C. S. Lantz, et al. (1997). "IgE enhances mouse mast cell Fc(epsilon)RI expression in vitro and in vivo: evidence for a novel amplification mechanism in IgE-dependent reactions." J Exp Med 185(4): 663-72.

Yamashita, T., S. Y. Mao, et al. (1994). "Aggregation of the high-affinity IgE receptor and enhanced activity of p53/56lyn protein-tyrosine kinase." Proc Natl Acad Sci U S A 91(23): 11251-5.

Yin, J., P. D. Straight, et al. (2005). "Genetically encoded short peptide tag for versatile protein labeling by Sfp phosphopantetheinyl transferase." Proc Natl Acad Sci U S A 102(44): 15815-20.

Young, R. M., X. Zheng, et al. (2005). "Reconstitution of regulated phosphorylation of FcepsilonRI by a lipid raft-excluded protein-tyrosine phosphatase." J Biol Chem 280(2): 1230-5.

Zhang, J., K. Leiderman, et al. (2006). "Characterizing the topography of membrane receptors and signaling molecules from spatial patterns obtained using nanometer-scale electron-dense probes and electron microscopy." Micron 37(1): 14-34.

Zidovetzki, R., M. Bartholdi, et al. (1986). "Rotational dynamics of the Fc receptor for immunoglobulin E on histamine-releasing rat basophilic leukemia cells." Biochemistry 25(15): 4397-401.